

<https://doi.org/10.14379/iodp.proc.382.107.2021>



Contents

- 1 Background and objectives
- 2 Operations
- 5 Lithostratigraphy
- 11 Biostratigraphy
- 17 Paleomagnetism
- 26 Geochemistry
- 31 Physical properties
- 38 Stratigraphic correlation
- 41 Downhole measurements
- 43 Core-log-seismic integration
- 47 References

Site U1538¹

M.E. Weber, M.E. Raymo, V.L. Peck, T. Williams, L.H. Armbrecht, I. Bailey, S.A. Brachfeld, F.G. Cardillo, Z. Du, G. Fauth, M. García, A. Glüder, M.E. Guitard, M. Gutjahr, S.R. Hemming, I. Hernández-Almeida, F.S. Hoem, J.-H. Hwang, M. Iizuka, Y. Kato, B. Kenlee, Y.M. Martos, S. O'Connell, L.F. Pérez, B.T. Reilly, T.A. Ronge, O. Seki, L. Tauxe, S. Tripathi, J.P. Warnock, and X. Zheng²

Keywords: International Ocean Discovery Program, IODP, *JOIDES Resolution*, Expedition 382, Iceberg Alley and Subantarctic Ice and Ocean Dynamics, Site U1538, Pirie Basin, Scotia Sea, Weddell Sea, sea ice, Antarctica, Antarctic Ice Sheet, sea level, ice-rafted debris, iceberg-rafted debris, iceberg, provenance, contourites, Weddell Sea Deep Water, Antarctic Circumpolar Current, Southern Hemisphere westerly winds, paleoceanography, paleoclimatology, mid-Pleistocene transition, Pliocene, interglacial climate, marine isotope stage, MIS 5, MIS 11

Background and objectives

International Ocean Drilling Program (IODP) Site U1538 (proposed Site SCO-11) is located 365 km north-northeast of the South Orkney Islands at 57°26.52'S, 43°21.47'W in 3131 m of water. The site lies in Pirie Basin and is situated at Shotpoint 4900 on Seismic Reflection Profile SCAN2013-13, 9 km east of Crossing Line SCAN2013-11. Site U1538 is located in the center of a small basin and provides the most undisturbed stratigraphy among the six potential drill sites in Pirie Basin. The seismic presite survey was conducted with a three-channel SPARKER system, so the depth penetration and resolution of the profile are limited compared to the multichannel seismic (MCS) records at Dove Basin Sites U1536 and U1537. Thus, it was more difficult to follow prominent reflectors and assign seismic units, although extended Pliocene–Pleistocene sections (Seismic Units I and II) were expected. Identification of Reflector d and acoustic basement is questionable.

Previous piston coring in Pirie Basin was conducted 9 km west of Site U1538 at Site MD07-3133 (alternate proposed Site SCO-01) along Seismic Line SCAN2013-13. Site MD07-3133 recovered a 36 m long sediment core that reaches back to Marine Isotope Stage (MIS) 3, which implied that the high sedimentation rates observed at Dove Basin Sites U1536 and U1537 could be doubled in Pirie Basin. However, Site MD07-3133 is located at a marginal position of the small basin in the northern Pirie Basin with potential seismic discontinuities below ~160 meters below seafloor (mbsf). Therefore, Site U1538, in the central part of that basin, was chosen for

drilling to maximize undisturbed recovery and recover the thickest Pleistocene section.

Sediments in the southern Scotia Sea are primarily deposited by contourite currents along the pathway of the Antarctic Circumpolar Current (ACC). Pirie Basin is located farther north and closer to the center of the ACC than Dove Basin and is expected to be less influenced by Weddell Sea Deep Water. The contourites are generally lens shaped and have a total thickness of as much as 1 km, similar to the sediment deposition observed above basement in Dove Basin (Maldonado et al., 2006).

At Site U1538, the main objective was to obtain a complete record of ice and ocean dynamics in the center of “Iceberg Alley” since the late Neogene in the more northerly of our two drilling areas in the Scotia Sea. Specific objectives in Pirie Basin included (1) the reconstruction of past variability in Antarctic Ice Sheet mass loss and the related sea level history at a site with potentially more iceberg-rafted debris (IBRD) derived directly from the Pacific side of the West Antarctic Ice Sheet through clockwise transport in the ACC; (2) the capture of the northern, more Circumpolar Deep Water-dominated part of the Drake Passage throughflow and associated north–south shifts of frontal systems, water mass properties, ocean temperature, and sea ice extent; and (3) the reconstruction of changes in atmospheric circulation and dust-climate couplings between Patagonia and Antarctica and related atmospheric circulation changes throughout the Pliocene–Pleistocene in a more proximal location relative to the main dust source, Patagonia.

¹ Weber, M.E., Raymo, M.E., Peck, V.L., Williams, T., Armbrecht, L.H., Bailey, I., Brachfeld, S.A., Cardillo, F.G., Du, Z., Fauth, G., García, M., Glüder, A., Guitard, M.E., Gutjahr, M., Hemming, S.R., Hernández-Almeida, I., Hoem, F.S., Hwang, J.-H., Iizuka, M., Kato, Y., Kenlee, B., Martos, Y.M., O'Connell, S., Pérez, L.F., Reilly, B.T., Ronge, T.A., Seki, O., Tauxe, L., Tripathi, S., Warnock, J.P., and Zheng, X., 2021. Site U1538. In Weber, M.E., Raymo, M.E., Peck, V.L., Williams, T., and the Expedition 382 Scientists, *Iceberg Alley and Subantarctic Ice and Ocean Dynamics*. Proceedings of the International Ocean Discovery Program, 382: College Station, TX (International Ocean Discovery Program). <https://doi.org/10.14379/iodp.proc.382.107.2021>

² Expedition 382 Scientists' affiliations.

MS 382-107: Published 20 May 2021

This work is distributed under the [Creative Commons Attribution 4.0 International](https://creativecommons.org/licenses/by/4.0/) (CC BY 4.0) license. 

Operations

We arrived at Site U1538 at 0240 h local time on 4 May 2019 after the 127 nmi transit northwest from the Dove Basin area. We lowered the thrusters, assembled the drill string, and lowered it to the seafloor.

We started Hole U1538A at 1615 h on 4 May. The seafloor depth was 3130.6 meters below sea level (mbsl), as calculated from the mudline. Over the next 6 days, Cores 382-U1538A-1H through 75X penetrated from the seafloor to 676.0 mbsf and recovered 476.4 m (70%) (Table T1). Formation temperature measurements were made while taking advanced piston corer (APC) Cores 6H, 9H, 12H, 15H, and 18H.

At 1130 h on 5 May after taking Core 382-U1538A-17H, an iceberg and a bergy bit entered the red zone, so we raised the drill string to 45 mbsf and offset 35 m northwest to allow the bergy bit to pass. The larger of the two icebergs was clear of the red zone at 1530 h, and we lowered the drill string back to 159.8 mbsf and resumed coring. Because Core 30H was difficult to extract from the formation and required a drillover to retrieve it, we switched to half-length APC (HLAPC) coring for Cores 31F–34F and reached 294.4 mbsf.

At that point, the hole was deep enough that we would want to reenter it if forced off site by an iceberg, so at 1720 h on 6 May we deployed a free-fall funnel (FFF) to enable reentry. We resumed coring at 1830 h and took Core 382-U1538A-35F, which also required a

Table T1. Core summary, Site U1538. DRF = drilling depth below rig floor, DSF = drilling depth below seafloor, CSF = core depth below seafloor. NA = not applicable. H = advanced piston corer (APC), F = half-length APC (HLAPC), X = extended core barrel (XCB). – = none. (Continued on next two pages.) [Download table in CSV format.](#)

Hole U1538A

Latitude: 57°26.5248'S
 Longitude: 43°21.4691'W
 Water depth (m): 3130.58
 Date started (UTC): 0545 h; 4 May 2019
 Date finished (UTC): 1930 h; 10 May 2019
 Time on hole (days): 6.57
 Seafloor depth DRF (m): 3141.7
 Seafloor depth est. method: APC calculated
 Rig floor to sea level (m): 11.12
 Penetration DSF (m): 676
 Cored interval (m): 676
 Recovered length (m): 476.43
 Recovery (%): 70.48
 Drilled interval (m): NA
 Drilled interval (N): 0
 Total cores (N): 75
 APC cores (M): 30
 HLAPC cores (N): 5
 XCB cores (M): 40

Hole U1538C

Latitude: 57°26.5387'S
 Longitude: 43°21.4521'W
 Water depth (m): 3130.21
 Date started (UTC): 2245 h; 10 May 2019
 Date finished (UTC): 1800 h; 11 May 2019
 Time on hole (days): 0.8
 Seafloor depth DRF (m): 3141.4
 Seafloor depth est. method: APC calculated
 Rig floor to sea level (m): 11.19
 Penetration DSF (m): 105.9
 Cored interval (m): 105.9
 Recovered length (m): 98.92
 Recovery (%): 93.41
 Drilled interval (m): NA
 Drilled interval (N): 0
 Total cores (N): 12
 APC cores (M): 11
 HLAPC cores (N): 1

Hole U1538B

Latitude: 57°26.5368'S
 Longitude: 43°21.4454'W
 Water depth (m): 3129.81
 Date started (UTC): 1930 h; 10 May 2019
 Date finished (UTC): 2245 h; 10 May 2019
 Time on hole (days): 0.14
 Seafloor depth DRF (m): 3141
 Seafloor depth est. method: APC calculated
 Rig floor to sea level (m): 11.19
 Penetration DSF (m): 8.5
 Cored interval (m): 8.5
 Recovered length (m): 8.49
 Recovery (%): 99.88
 Drilled interval (m): NA
 Drilled interval (N): 0
 Total cores (N): 1
 APC cores (M): 1

Hole U1538D

Latitude: 57°26.5335'S
 Longitude: 43°21.4723'W
 Water depth (m): 3130.4
 Date started (UTC): 2230 h; 12 May 2019
 Date finished (UTC): 0200 h; 14 May 2019
 Time on hole (days): 1.15
 Seafloor depth DRF (m): 3141.6
 Seafloor depth est. method: APC calculated
 Rig floor to sea level (m): 11.2
 Penetration DSF (m): 126.4
 Cored interval (m): 126.4
 Recovered length (m): 114.6
 Recovery (%): 90.66
 Drilled interval (m): NA
 Drilled interval (N): 0
 Total cores (N): 14
 APC cores (M): 14

Core	Date (2019)	Time on deck UTC (h)	Top depth drilled DSF (m)	Bottom depth drilled DSF (m)	Interval advanced (m)	Top depth cored CSF-A (m)	Bottom depth recovered CSF-A (m)	Recovered length (m)	Curated length (m)	Core recovery (%)	Sections (N)
382-U1538A-											
1H	4 May	1940	0.0	7.8	7.8	0.0	7.9	7.89	7.89	101	7
2H	4 May	2100	7.8	17.3	9.5	7.8	16.8	8.98	8.98	95	8
3H	4 May	2200	17.3	26.8	9.5	17.3	26.9	9.56	9.56	101	8
4H	4 May	2315	26.8	36.3	9.5	26.8	36.3	9.53	9.53	100	8
5H	5 May	0015	36.3	45.8	9.5	36.3	45.3	8.95	8.95	94	7
6H	5 May	0130	45.8	55.3	9.5	45.8	55.4	9.59	9.59	101	8
7H	5 May	0225	55.3	64.8	9.5	55.3	64.6	9.28	9.28	98	8

Table T1 (continued). (Continued on next page.)

Core	Date (2019)	Time on deck UTC (h)	Top depth drilled DSF (m)	Bottom depth drilled DSF (m)	Interval advanced (m)	Top depth cored CSF-A (m)	Bottom depth recovered CSF-A (m)	Recovered length (m)	Curated length (m)	Core recovery (%)	Sections (N)
8H	5 May	0330	64.8	74.3	9.5	64.8	72.7	7.86	7.86	83	7
9H	5 May	0440	74.3	83.8	9.5	74.3	84.6	10.22	10.29	108	8
10H	5 May	0550	83.8	93.3	9.5	83.8	93.3	9.49	9.49	100	8
11H	5 May	0700	93.3	102.8	9.5	93.3	102.6	9.28	9.28	98	8
12H	5 May	0815	102.8	112.3	9.5	102.8	113.0	10.02	10.18	105	8
13H	5 May	0940	112.3	121.8	9.5	112.3	121.9	9.59	9.59	101	9
14H	5 May	1045	121.8	131.3	9.5	121.8	131.2	9.38	9.38	99	8
15H	5 May	1205	131.3	140.8	9.5	131.3	141.3	10.00	10.02	105	8
16H	5 May	1315	140.8	150.3	9.5	140.8	149.9	9.05	9.06	95	7
17H	5 May	1425	150.3	159.8	9.5	150.3	159.2	8.87	8.87	93	7
18H	5 May	2140	159.8	169.3	9.5	159.8	169.3	9.52	9.52	100	7
19H	5 May	2240	169.3	178.8	9.5	169.3	179.4	10.07	10.07	106	8
20H	5 May	2345	178.8	188.3	9.5	178.8	188.8	9.97	10.01	105	8
21H	6 May	0045	188.3	197.8	9.5	188.3	197.9	9.51	9.59	100	8
22H	6 May	0145	197.8	207.3	9.5	197.8	208.0	10.17	10.17	107	8
23H	6 May	0345	207.3	216.8	9.5	207.3	211.4	4.12	4.12	43	4
24H	6 May	0450	216.8	226.3	9.5	216.8	226.9	10.11	10.11	106	8
25H	6 May	0555	226.3	235.8	9.5	226.3	226.4	0.10	0.10	1	1
26H	6 May	0650	235.8	245.3	9.5	235.8	245.7	9.92	9.92	104	8
27H	6 May	0800	245.3	254.8	9.5	245.3	252.5	7.13	7.19	75	8
28H	6 May	0905	254.8	264.3	9.5	254.8	264.7	9.88	9.88	104	8
29H	6 May	1000	264.3	273.8	9.5	264.3	273.1	8.79	8.79	93	8
30H	6 May	1155	273.8	283.3	9.5	273.8	283.7	9.86	9.86	104	8
31F	6 May	1350	283.3	288.1	4.8	283.3	288.3	5.02	5.02	105	5
32F	6 May	1500	288.1	292.9	4.8	288.1	292.9	4.84	4.84	101	5
33F	6 May	1625	292.9	297.7	4.8	292.9	297.9	4.96	4.96	103	5
34F	6 May	1715	297.7	302.5	4.8	297.7	302.5	4.82	4.82	100	5
35F	6 May	2325	302.5	307.3	4.8	302.5	307.5	5.02	5.02	105	5
36X	7 May	0055	307.3	316.0	8.7	307.3	316.9	9.59	9.59	110	8
37X	7 May	0200	316.0	325.5	9.5	316.0	324.2	8.24	8.24	87	7
38X	7 May	0310	325.5	335.0	9.5	325.5	334.0	8.51	8.51	90	7
39X	7 May	0435	335.0	344.5	9.5	335.0	344.3	9.33	9.33	98	8
40X	7 May	0545	344.5	354.0	9.5	344.5	353.5	8.98	8.98	95	7
41X	7 May	0705	354.0	363.5	9.5	354.0	359.8	5.79	5.79	61	5
42X	7 May	0820	363.5	373.0	9.5	363.5	372.1	8.57	8.57	90	7
43X	7 May	0925	373.0	382.5	9.5	373.0	378.7	5.74	5.74	60	5
44X	7 May	1040	382.5	392.0	9.5	382.5	387.4	4.92	4.92	52	5
45X	7 May	1155	392.0	401.5	9.5	392.0	400.0	8.56	8.56	90	7
46X	7 May	1325	401.5	411.0	9.5	401.5	409.5	8.03	8.03	85	7
47X	7 May	1450	411.0	420.6	9.6	411.0	416.0	5.04	5.04	53	5
48X	7 May	1605	420.6	430.2	9.6	420.6	426.0	5.36	5.36	56	5
49X	7 May	1930	430.2	439.8	9.6	430.2	436.5	6.28	6.28	65	5
50X	7 May	2050	439.8	449.4	9.6	439.8	449.5	9.68	9.68	101	8
51X	7 May	2220	449.4	459.0	9.6	449.4	450.3	0.92	0.92	10	2
52X	8 May	0040	459.0	468.6	9.6	459.0	460.2	1.22	1.22	13	2
53X	8 May	0310	468.6	478.2	9.6	468.6	477.9	9.33	9.33	97	8
54X	8 May	0515	478.2	487.8	9.6	478.2	484.9	6.73	6.73	70	6
55X	8 May	0725	487.8	497.4	9.6	487.8	488.6	0.81	0.81	8	2
56X	8 May	0925	497.4	507.0	9.6	497.4	504.7	7.26	7.26	76	6
57X	8 May	1135	507.0	516.6	9.6	507.0	509.9	2.90	2.90	30	3
58X	8 May	1420	516.6	526.2	9.6	516.6	519.2	2.57	2.57	27	3
59X	8 May	1630	526.2	535.8	9.6	526.2	533.8	7.55	7.55	79	6
60X	8 May	1915	535.8	545.4	9.6	535.8	539.1	3.27	3.27	34	4
61X	8 May	2110	545.4	555.0	9.6	545.4	550.1	4.74	4.74	49	5
62X	8 May	2325	555.0	564.6	9.6	555.0	558.0	2.97	2.97	31	5
63X	9 May	0150	564.6	574.1	9.5	564.6	564.6	—	—	NA	0
64X	9 May	0420	574.1	583.6	9.5	574.1	574.1	—	—	NA	0
65X	9 May	0635	583.6	593.1	9.5	583.6	589.0	5.40	5.40	57	5
66X	9 May	1335	593.1	597.9	4.8	593.1	593.2	0.06	0.06	1	1
67X	9 May	1920	597.9	602.7	4.8	597.9	598.1	0.18	0.18	4	1
68X	9 May	2225	602.7	612.2	9.5	602.7	603.2	0.49	0.49	5	2
69X	10 May	0200	612.2	621.8	9.6	612.2	614.9	2.70	2.70	28	3
70X	10 May	0405	621.8	631.4	9.6	621.8	622.1	0.28	0.28	3	1
71X	10 May	0630	631.4	641.0	9.6	631.4	632.5	0.74	1.10	8	2
72X	10 May	0850	641.0	650.6	9.6	641.0	643.7	2.74	2.74	29	4
73X	10 May	1105	650.6	660.2	9.6	650.6	653.5	2.92	2.92	30	3
74X	10 May	1340	660.2	669.8	9.6	660.2	663.8	3.60	3.60	38	4

Table T1 (continued).

Core	Date (2019)	Time on deck UTC (h)	Top depth drilled DSF (m)	Bottom depth drilled DSF (m)	Interval advanced (m)	Top depth cored CSF-A (m)	Bottom depth recovered CSF-A (m)	Recovered length (m)	Curated length (m)	Core recovery (%)	Sections (N)
75X	10 May	1615	669.8	676.0	6.2	669.8	672.9	3.08	3.08	50	4
					Hole U1538A totals:	676		476.43	476.43	70.48	
382-U1538B-											
1H	10 May	2240	0.0	8.5	8.5	0.0	8.5	8.49	8.49	100	7
					Hole U1538B totals:	8.5		8.49	8.49	99.88	
382-U1538C-											
1H	11 May	0100	0.0	6.1	6.1	0.0	6.1	6.13	6.13	100	5
2H	11 May	0215	6.1	15.6	9.5	6.1	15.7	9.54	9.56	100	8
3H	11 May	0310	15.6	25.1	9.5	15.6	24.6	9.03	9.03	95	8
4H	11 May	0410	25.1	34.6	9.5	25.1	34.2	9.13	9.13	96	8
5H	11 May	0510	34.6	44.1	9.5	34.6	42.8	8.16	8.16	86	7
6F	11 May	0640	44.1	48.9	4.8	44.1	48.0	3.92	3.92	82	4
7H	11 May	0730	48.9	58.4	9.5	48.9	58.5	9.57	9.57	101	8
8H	11 May	0820	58.4	67.9	9.5	58.4	66.2	7.79	7.79	82	7
9H	11 May	0915	67.9	77.4	9.5	67.9	77.4	9.45	9.45	99	8
10H	11 May	1020	77.4	86.9	9.5	77.4	85.4	7.98	7.98	84	7
11H	11 May	1130	86.9	96.4	9.5	86.9	96.1	9.13	9.19	96	7
12H	11 May	1250	96.4	105.9	9.5	96.4	105.5	9.09	9.11	96	8
					Hole U1538C totals:	105.9		98.92	98.92	93.41	
382-U1538D-											
1H	13 May	0110	0.0	2.9	2.9	0.0	2.9	2.93	2.93	101	3
2H	13 May	0225	2.9	12.4	9.5	2.9	11.7	8.78	8.78	92	7
3H	13 May	0330	12.4	21.9	9.5	12.4	21.8	9.36	9.36	99	8
4H	13 May	0440	21.9	31.4	9.5	21.9	30.4	8.54	8.54	90	7
5H	13 May	0545	31.4	40.9	9.5	31.4	41.0	9.59	9.59	101	8
6H	13 May	0705	40.9	50.4	9.5	40.9	49.8	8.91	8.91	94	7
7H	13 May	0805	50.4	59.9	9.5	50.4	60.2	9.81	9.81	103	8
8H	13 May	0910	59.9	69.4	9.5	59.9	68.5	8.61	8.61	91	8
9H	13 May	1010	69.4	78.9	9.5	69.4	78.3	8.88	8.88	93	7
10H	13 May	1110	78.9	88.4	9.5	78.9	86.8	7.91	7.91	83	7
11H	13 May	1210	88.4	97.9	9.5	88.4	97.5	9.08	9.08	96	7
12H	13 May	1325	97.9	107.4	9.5	97.9	107.2	9.27	9.27	98	7
13H	13 May	1445	107.4	116.9	9.5	107.4	111.7	4.29	4.29	45	4
14H	13 May	1540	116.9	126.4	9.5	116.9	125.5	8.64	8.64	91	8
					Hole U1538D totals:	126.4		114.6	114.6	90.66	
					Site U1538 totals:	916.8		698.44	698.44		

drillover, so we switched to extended core barrel (XCB) coring for the rest of Hole U1538A. From 1300 to 1500 h on 8 May, we waited for a large iceberg to pass the edge of the red zone (3 nmi from the ship) with the drill bit close to the bottom of the hole. Coring then continued until 2145 h, when another iceberg approached close to the red zone; however, it changed direction away from the ship, and we resumed coring at 2230 h. After taking Core 66X (597.9 mbsf), coring was interrupted from 0415 to 0900 h on 9 May when an iceberg passed through the red zone. We raised the drill string to 45 mbsf and waited until after the iceberg passed, its closest distance 1.2 nmi from the ship, before resuming coring. From 1930 to 2100 h, ship heave was about 4 m, which was too high to maintain a consistent weight on bit, so we stood by and waited for heave to subside. The final cores from Hole U1538A (69X–75X) were recovered without interruption. We stopped coring at 1315 h on 10 May after reaching the maximum depth of 676 mbsf permitted by the IODP Environmental Protection and Safety Panel for this site.

We decided to forgo downhole logging in Hole U1538A because ship heave exceeded 3 m and was forecast to become higher, which would pose a risk to the downhole logging tools and increase uncertainty in the depth registration of the logging data. Because the hole has a FFE, it was possible that we could return to log it if sea and heave conditions became calmer before the end of operations at this

site. We displaced the hole with 10.5 lb/gal heavy mud to help stabilize the borehole walls in case we returned to log the hole.

We started Hole U1538B at 1900 h on 10 May. Core 382-U1538B-1H recovered 7.8 m and was sampled for interstitial water (IW) at high resolution. We then offset 20 m to the south.

We started Hole U1538C at 2135 h on 10 May. Cores 382-U1538C-1H through 12H penetrated from the seafloor to 105.9 mbsf and recovered 98.9 m (93%). One HLAPC core (6F) was taken to adjust the depth offset to splice over core breaks in Hole U1538A. At 1000 h on 11 May, the sea and wind conditions had deteriorated to the extent that we could not safely handle the core barrel on the rig floor. We waited with the drill string in the hole, but it was apparent that conditions would not improve that day, so at 1500 h we raised the drill string clear of the seafloor, ending Hole U1538C. The next 28.5 h were spent waiting on weather. At midnight, the ship's pitch, roll, and heave were 3.5°, 3.8°, and 6 m, respectively. The ship's heave (maximum peak to peak heave over a 10 min interval) remained above 5 m until 1930 h on 12 May. At that time, we were able to resume rig floor operations.

Hole U1538D was started at 2145 h on 12 May. Cores 382-U1538D-1H through 14H penetrated from the seafloor to 126.4 mbsf and recovered 114.6 m (91%). A formation temperature measurement was made while taking Core 12H. The last core came on

deck at 1240 h on 13 May, and the bit was clear of the seafloor at 1430 h, ending Hole U1538D. We had to stop coring to leave time to raise the drill string and secure the bottom-hole assembly (BHA) for transit before stormy weather and high seas arrived early on 14 May. At 2345 h, the rig floor was secure.

Having completed operations at Site U1538, we started the sea voyage to Punta Arenas, Chile, at 0000 h on 14 May. We had to leave Site U1538 earlier than originally planned because of deteriorating weather and sea conditions. This earlier departure briefly opened a short time window that could have been used to core an additional ~100 m hole at Site U1534, which lies almost directly along the course from Site U1538 to Punta Arenas. However, headwinds slowed our progress to the extent that we no longer had time to carry out this plan. Instead, we slowed to 5 kt and made a single line 3.5 kHz subbottom profiler survey east-to-west over Sites U1535 and U1534. The survey recorded reflections to about 70 mbsf, and the profile will help to correlate the stratigraphies between the two sites. We then continued directly to Punta Arenas, arriving at 1530 h on 19 May.

Lithostratigraphy

Based on visual core description, sediment composition, smear slide analysis, and X-radiographs, we identified two lithostratigraphic units (Figures F1, F2). Unit II is divided into three subunits. Unit classification was based on major and minor terrestrial and biogenic components and on lithification (e.g., the change from diatom ooze to diatomite).

Most APC and HLAPC cores are relatively undisturbed. We used the XCB system for the first time at this site (Hole U1538A; 307–676 mbsf), and it provided moderately to heavily disturbed (biscuited and fall-in) cores throughout the hole. However, most biscuits appear to be stratigraphically in place and internally undisturbed.

Unit descriptions

Unit I

Intervals: 382-U1538A-1H-1 to 35F-CC; 382-U1538B-1H-1 to 1H-CC; 382-U1538C-1H-1 to 12H-CC; 382-U1538D-1H-1 to 14H-CC

Depths: Hole U1538A = 0–307.52 mbsf; Hole U1538B = 0–8.49 mbsf; Hole U1538C = 0–105.51 mbsf; Hole U1538D = 0–126.4 mbsf

Age: mid-Pleistocene to Holocene

Lithostratigraphic Unit I predominantly consists of interbedded dark greenish gray diatom oozes with variable terrigenous components and biosilica-rich/bearing silty clays (Figures F3, F4).

The biogenic fraction consists predominantly of biosilica dominated by diatoms (>50%) and minor components of spicules (5%–10%), radiolarians (5%–10%), and rare carbonaceous fossils, such as foraminifers (Table T2) and nannofossils, in some core sections. Smear slide analyses of the terrigenous fraction indicates a composition dominated by quartz (~25% to >50%) with minor components of feldspar (10%–25%). The most abundant accessory minerals are unspecified opaques, glauconite, mica, and amphibole. A distinctive greenish gray biogenic carbonate-bearing interval was identified in Cores 382-U1538A-13H and 14H and 382-U1538D-4H. Based on the preliminary shipboard stratigraphy, this nannofossil- and foraminifer-bearing interval is interpreted to represent MIS 11.

Thin, centimeter- to decimeter-thick carbonate layers are present throughout this unit (Figure F5; Table T3). A common feature in all holes is a 10–15 cm thick layer of dark greenish gray volcanoclastic-rich diatom ooze found in Section 382-U1538D-2H-4 (~8 mbsf) and at equivalent depths in Holes U1538A and U1538C.

Color banding of sediments is common in most cores throughout this unit. True laminations are rare (e.g., Section 382-U1538A-8H-2). Transitions between the minor and major lithologies are typically gradual.

The average core recovery in Unit I was 95.5%.

Unit II

Lithostratigraphic Unit II is marked by a pronounced change in the compaction of retrieved sediments. The subunits are dominated by lithified biosilicate-bearing/rich silty clays interbedded with silty clay-bearing/rich diatomites (Figure F2). Minor and major lithologic components are similar to Unit I. The average recovery in Unit II was 51.8%.

Subunit IIA

Interval: 382-U1538A-36X-1 to 42X-1, 21 cm

Depth: 307.52–363.75 mbsf

Age: early to mid-Pleistocene

Lithostratigraphic Subunit IIA is dominated by silty clay-rich diatomites with interbedded intervals of biosilica-rich silty clay. Several layers of coarse-grained sand to very fine gravel layers as well as biosilica-bearing sandy mud (Figure F6) were observed throughout Subunit IIA (Table T4). Color banding of both the silty clays and diatomites is common throughout this unit. True laminations, however, are only present in Sections 382-U1538A-36X-1 and 39X-CC (Figure F7).

Drilling disturbance in this subunit is much more pronounced than in Unit I. Every core suffered from moderate to high biscuiting and uparching, and fall-in was common. As far as we can tell from the biscuited record, most lithologic transitions are gradational.

Of the three Unit II subunits, Subunit IIA had the highest recovery rates, averaging 90%.

Subunit IIB

Interval: 382-U1538A-42X-1, 25 cm, to 51X-1, 6 cm

Depth: 363.75–449.46 mbsf

Age: Pliocene to early Pleistocene

In contrast to Subunit IIA, Subunit IIB is almost exclusively dominated by lithified biosilica-bearing and diatom-bearing/rich silty clay.

IBRD was observed throughout most core sections. At the top of Section 382-U1538A-42X-1 (fall-in) and in Section 47X-CC, larger dropstones and gravel layers are present. Layers of silty sand and biosilica-bearing sandy mud are rare but present throughout Subunit IIB (Table T4). Core 49X, however, is an exception. It is composed of interbedded diatom-bearing silty clays, prominent sandy mud layers, and several larger (>2 cm) dropstones. With the exception of Cores 37X–39X, all cores contain foraminifers (Table T2).

Throughout the entire unit, the silty clays display distinctive color banding, mottling, and several bioturbated intervals with pyritized (halo) burrows. All cores and sections in Subunit IIB are moderately to highly disturbed (biscuited), yet the biscuits themselves are stratigraphically in order and internally undisturbed.

On average, recovery in Subunit IIB was 66.2%.

Figure F1. Visual core description, Hole U1538A. This is the only hole where all units described were cored. CSF-A = core depth below seafloor, Method A. Pebble abundance >2 mm is semiquantitative visual assessment of concentration from 1 (no gravel or pebbles) to 5 (many gravel and pebble pieces) per core; pebble abundance >2 cm is semiquantitative count of >2 cm pebbles per core.

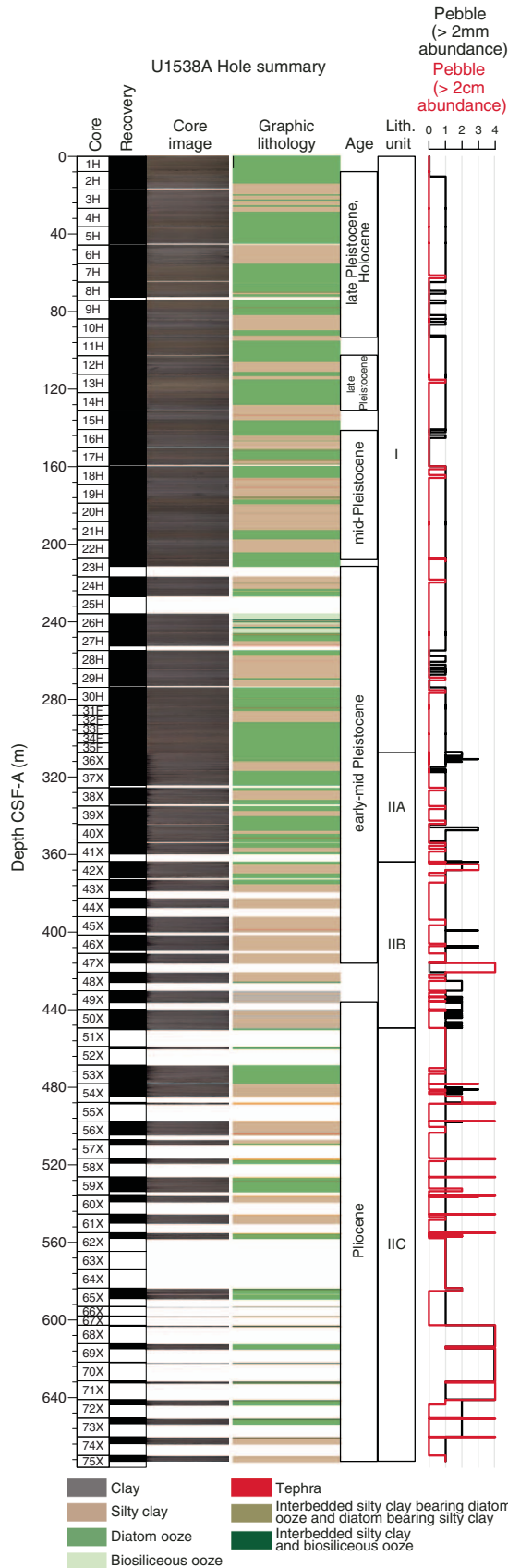


Figure F2. Main lithologies. A. Diatom ooze (382-U1538A-7H-4, 50–80 cm). B. Diatomite (40X-2, 50–80 cm). C. Silty clay (20H-5, 30–60 cm). D. Lithified silty clay (44X-2, 50–80 cm).



Figure F3. Silty clay–bearing diatom ooze (382-U1538A-2H-3, 35 cm).

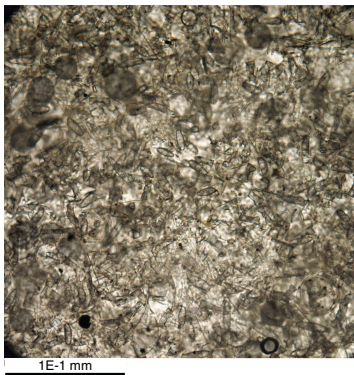
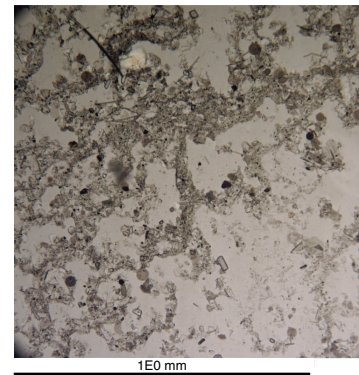


Figure F4. Biosilica-rich silty clay (382-U1538A-24H-1, 128 cm).



Subunit IIC

Interval: 382-U1538A-51X-1, 6 cm, to 75X-CC
 Depth: 449.46–672.82 mbsf
 Age: Pliocene

Lithostratigraphic Subunit IIC consists of lithified biosilica-rich silty clays and silty clay–rich diatomites similar to Subunit IIA. However, Subunit IIC is characterized by significantly larger and more common dropstones (Figure F8). These dropstones aggregate as fall-in in the uppermost sections of each core (Figure F8C, F8E, F8F) but also occur in situ throughout the subunit (Figure F9).

A preliminary analysis of core catcher samples showed the presence of planktonic foraminifers (*Neogloboquadrina pachyderma* sinistral) in Cores 382-U1538A-47X and 56X. Because of severe biscuiting and the abundant coring gaps, it is hard to identify lithologic boundaries between lithologic intervals.

With 33.8% recovery, Subunit IIC had the lowest recovery rate of all the units.

Foraminifer abundance

Because planktonic foraminifers were observed at Site U1537, paleontology (PAL) samples from Cores 382-U1538A-1H through

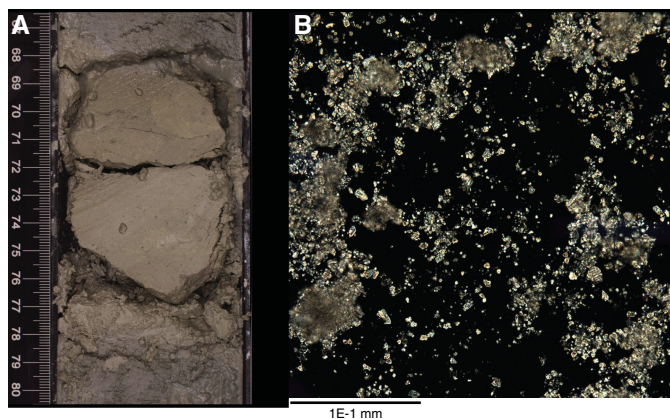
Table T2. Planktonic and benthic foraminifers found in core catcher samples, Hole U1538A. — = none found. [Download table in CSV format.](#)

Core	<i>N. pachyderma</i> sinistral	Calcareous benthics
382-U1538A-		
1H	Common	<i>Melonis</i>
2H	Common	—
5H	Common	<i>Pullenia</i>
6H	Rare	<i>Melonis</i>
7H	Common	<i>Pullenia</i>
11H	Common	<i>Melonis</i>
12H	Rare	<i>Melonis</i>
13H	Common	—
14H	Rare (yellow)	<i>Pullenia</i>
18H	Rare (yellow)	—
19H	Rare (yellow)	—
28H	Rare (yellow)	—
32F	Common	—
34F	Rare	—
36X	Common	—
39X	Common (yellow)	—
40X	Common	—
41X	Common	—
42X	Common	<i>Pullenia</i>
43X	Common	—

Table T3. Carbonate layers observed, Site U1538. [Download table in CSV format.](#)

Core, section, interval (cm)	
382-U1538A-	
5H-2, 0–96	
8H-4, 68–78	
9H-3, 68–74	
9H-3, 91–94	
15H-2, 93–101	
16H-6, 138–142	
16H-CC, 0–5	
17H-1, 96–108	
17H-5, 90–94	
18H-5, 72–76	
19H-1, 113–121	
27H-1, 97–112	
27H-CC, 19–24	
27H-CC, 31–37	
28H-4, 81–88	
28H-4, 118–121	
28H-4, 135–140	
30H-4, 112–119	
35F-CC, 15–20	
36X-7, 78–84	
39X-5, 13–18	
40X-4, 18–20	
40X-5, 31–33	
40X-5, 49–53	
40X-5, 56–61	
43X-1, 147–150	
43X-2, 0–2	
73X-1, 19–38	
382-U1538C-	
9H-3, 79–88	
12H-5, 56–60	
382-U1538D-	
8H-7, 29–30	
8H-7, 35–38	
10H-1, 0–18	

Figure F5. Carbonate layer (382-U1538A-8H-4, 67–80 cm).



50X were sieved to assess the presence of foraminifers. Below Core 50X, the onset of lithification made samples difficult to disaggregate. Planktonic species *N. pachyderma* sinistral was found in almost half of the analyzed samples from Units I and II. One yellow, heavily recalcified specimen of *Globigerinoides bulloides* was observed in Sample 39X-CC (Subunit IIA). The abundance of *N. pachyderma* sinistral (>125 μm) is reported in Table T2, where rare indicates fewer than 5 specimens per 20 cm^3 sample. Common indicates that 16 specimens or more were found in the sample. Specimens appear to be well preserved in most samples, although samples bearing yellow recalcified tests are noted in the table. Agglutinated benthic foraminifers were observed, as were rare occurrences of small calcareous benthics, namely *Pullenia bulloides* and *Melonis affinis*.

X-radiographs

X-ray images were taken from all four holes at Site U1538 (4045 images from Hole U1538A, 73 images from Hole U1538B, 842 images from Hole U1538C, and 978 images from Hole U1538D). This

report includes the visual analysis of images from Hole U1538A APC/HLAPC and XCB cores. The preliminary study focused on the background texture, presence of IBRD, and other features such as pyritized burrows, carbonate or sandy layers, and internal structure. The lithified sediment in XCB cores only allowed identification of IBRDs and burrows. The two dominant lithologies (diatom ooze and silty clay) show textures similar to those from Sites U1536 and U1537 (see [Lithostratigraphy](#) in the Site U1536 chapter and [Lithostratigraphy](#) in the Site U1537 chapter [Weber et al., 2021b, 2021c]). IBRDs and a variety of burrows are also common at Site U1538.

A correlation of IBRDs and burrows with the main lithologies and physical properties (magnetic susceptibility [MS]; Figure F10) was established in the shallower intervals with good core recovery from 0 to about 230 mbsf (Core 382-U1538A-23H). The correlation indicates that the highest IBRD occurrence correlates with the upward transition from silty clay to diatom ooze intervals, where MS decreases above the maximum peaks. The IBRD presence increases below 230 mbsf and becomes less variable with depth. Between 540 and 640 mbsf (Cores 60X–71X), IBRDs become more common before their presence reduces again deeper in the hole.

The presence of burrows is, however, directly correlated with the silty clay intervals displaying high MS values (Figure F10). Dark

Figure F6. Sandy/gravel layer (382-U1538A-36X-3, 47–55 cm).

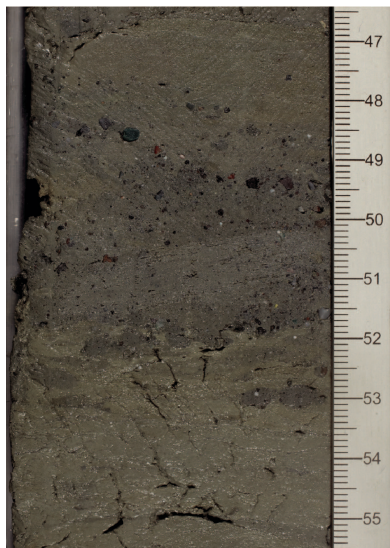


Figure F7. Laminated sediments (382-U1538A-36X-1, 42–59 cm).



Table T4. Sand and mud layers observed, Hole U1538A. [Download table in CSV format.](#)

Core, section, interval (cm)
382-U1538A-
36X-2, 82–87
36X-3, 49–53
36X-4, 36–42
40X-2, 27–37
40X-2, 135–150
40X-3, 0–3
42X-1, 10–14
42X-1, 20–22
43X-3, 79–85
45X-5, 116–120
46X-4, 92–99
46X-5, 59–67
49X-1-CC
50X-1-CC
51X-1, 0–6
54X-2-CC
56X-1, 52–55
56X-4, 6–11
56X-4, 77–84
56X-4, 140–145

fine burrows (possibly pyritized) are very common throughout the entire core, whereas wide ones occur at 30–50 and 100–380 mbsf and less frequently at 400–570 mbsf. White burrows only occur in

the shallower cores between 30 and 120 mbsf (Cores 382-U1538A-3H through 12H) and become rare at greater depths.

Postsedimentary deformation is revealed in detail by the X-ray images, and drilling disturbances showing as fluidized or broken-looking background textures are common at the top of the first sections of many cores.

Summary

Two lithostratigraphic units were identified based on sediment composition in smear slides and visual core description (Figure F1). The dominant lithologies are diatom oozes and silty clays in Unit I and lithified silty clays and diatomites in Unit II. Unit II consists of three subunits. Most cores in Unit I are relatively undisturbed, whereas the more lithified Unit II suffered from moderate to severe disturbance (biscuiting). Drilling disturbance is most prevalent in the core tops, which commonly are soupy or fall-in. Uparching and brecciated disturbance is rare.

Figure F8. IBRD. A. 382-U1538A-29H-4, 107–116 cm. B. 50X-7, 21–32 cm. C. 56X-1, 6–20 cm. D. 72X-2, 16–21 cm. E. 61X-1, 10–26 cm. F. 72X-1, 0–17 cm. C, E, and F show fall-in.

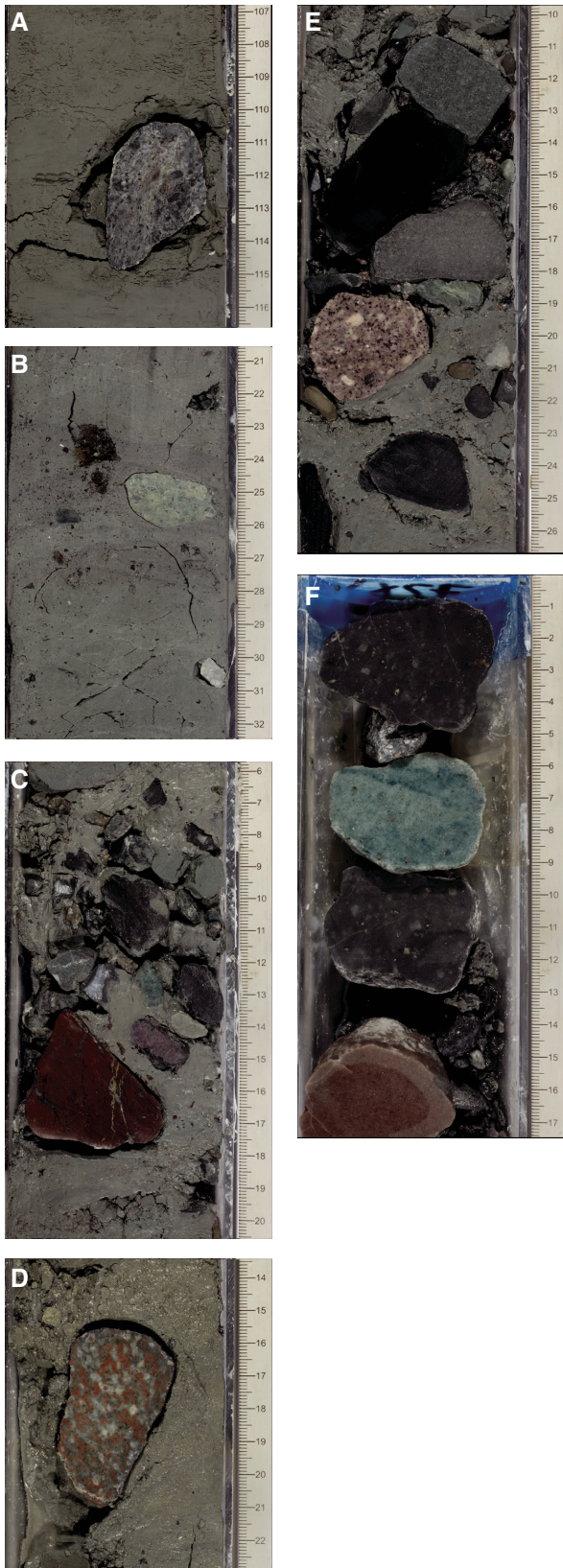


Figure F9. Fine-grained pinkish-gray volcanic rock (382-U1538A-62X-4). A. In situ. B. Normal light. C. Cross-polarized light.

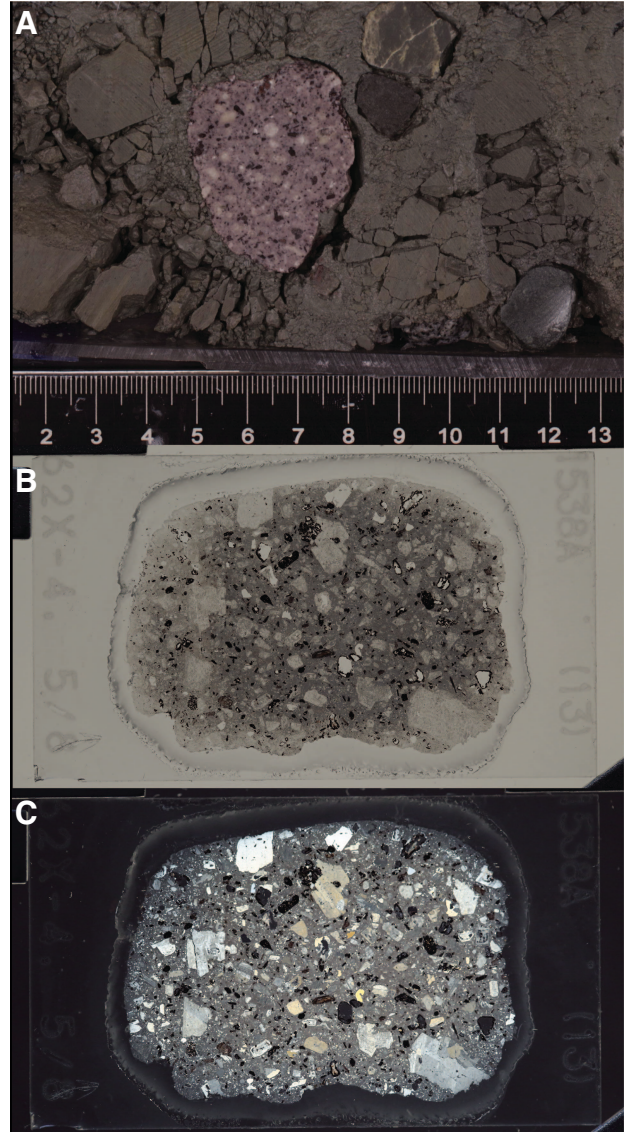
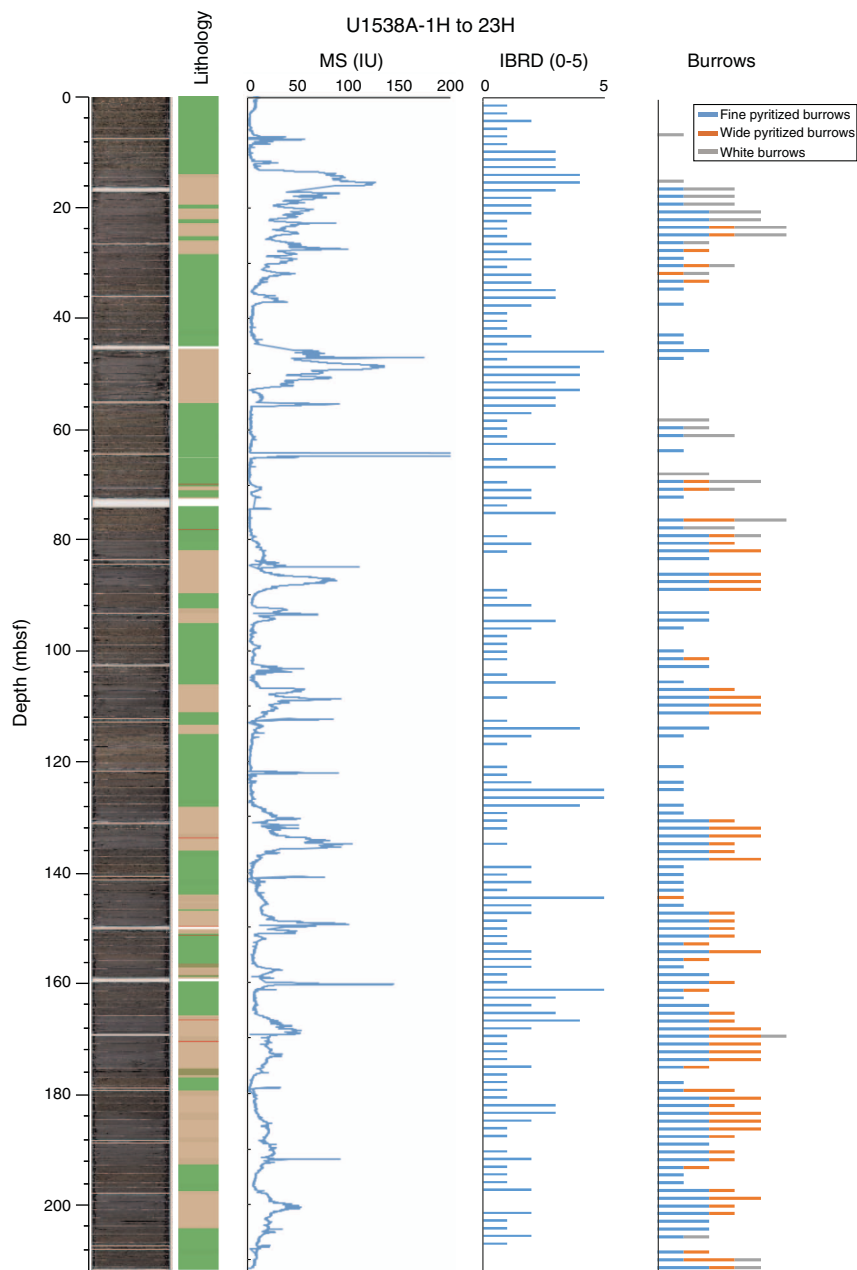


Figure F10. X-radiograph–based semiquantitative assessment of IBRD and burrow occurrence, Hole U1538A.



Biostratigraphy

Core catcher sediments primarily composed of diatom oozes and diatom-rich silty clays were analyzed for diatoms, radiolarians, palynomorphs, and foraminifers. Selected additional samples were analyzed for diatoms and radiolarians. Preservation and abundance are variable throughout the analyzed intervals; however, diatoms, radiolarians, and palynomorphs were found in nearly all analyzed sediments. Core catcher samples from Cores 382-U1538A-50X, 51X, 74X, and 75X have barren to very rare assemblages of in situ dinoflagellate cysts (dinocysts). Sediments range in age from Holocene to early Pliocene (Table T5). The specific age datums used are given in Table T6. A biostratigraphically derived age-depth model is presented in Figure F11.

Siliceous microfossils

Diatoms

Diatoms are present in all analyzed samples. Specific species relative abundances, diatom overall abundance, and initial diatom preservation data are given in Table T7. Diatom dissolution is variable throughout the analyzed samples, but in general dissolution is minimal. Diatom fragmentation increases downcore. In general, fragmentation is more extreme than dissolution. Reworking of diatom fossils occurs rarely at Site U1538 and was typically easy to detect (e.g., trace abundances of Miocene/Pliocene diatoms in otherwise late Pleistocene assemblages).

A Holocene and late Pleistocene assemblage composed of extant diatoms was identified in the mudline sample. This assemblage is

Table T5. Summary of biostratigraphically assigned ages to sample ranges by microfossil group, Site U1538. [Download table in CSV format.](#)

Interval	Depth CSF-A (m)	Diatoms	Radiolarians	Palynomorphs
382-U1538A-				
1H-CC to 10H-CC	7.84–93.29	Holocene, late Pleistocene	Holocene, late Pleistocene	
11H-CC to 14H-CC	102.53–131.18	late Pleistocene	late Pleistocene	
15H-CC to 22H-CC	141.27–207.97	mid-Pleistocene	mid-Pleistocene	
23H-CC to 47X-CC	211.37–416.04	mid-early Pleistocene	mid-early Pleistocene	
49X-CC to 75X-CC	436.19–672.88	Pliocene	Pliocene	Pliocene

Table T6. Biostratigraphic datums, Hole U1538A. DIAT = diatom, RAD = radiolarian, PALY = palynomorph. LO = last occurrence, FO = first occurrence. (Continued on next page.) [Download table in CSV format.](#)

Type	Event	Published age (Ma)	Top core, section, interval (cm)	Bottom core, section, interval (cm)	Top depth (mbsf)	Bottom depth (mbsf)	Middepth (mbsf)
			382-U1538A-	382-U1538A-			
RAD	LO <i>Stylatractus universus</i>	0.43	10H-CC	11H-CC	93.27	102.56	97.91
DIAT	LO <i>Rouxia leventerae</i>	0.14	10H-CC	11H-CC	93.27	102.56	97.91
DIAT	LO <i>Hemidiscus karstenii</i>	0.2	12H-CC	13H-CC	112.96	121.87	117.41
DIAT	LO <i>Rouxia constricta</i>	0.3	14H-CC	15H-CC	131.16	141.30	136.23
DIAT	LO <i>Actinocyclus ingens</i>	0.6	15H-CC	16H-CC	141.30	149.84	145.57
DIAT	LO <i>Rhizosolenia harwoodii</i>	0.6	15H-CC	16H-CC	141.30	149.84	145.57
DIAT	LO <i>Thalassiosira elliptipora</i>	0.7	16H-CC	17H-CC	149.84	159.15	154.49
RAD	LO <i>Antarctissa cylindrica</i>	0.64	17H-CC	18H-CC	159.12	169.27	164.20
DIAT	LO <i>Thalassiosira fasciculata</i>	0.9	22H-1, 74–75	22H-4, 74–75	198.55	202.98	200.76
RAD	LO <i>Pterocanium trilobum</i>	0.86	23H-CC	24H-1, 74–75	211.37	217.54	214.46
DIAT	FO <i>Rouxia constricta</i>	1.4	26H-CC	27H-CC	245.70	252.47	249.08
DIAT	LO <i>Fragilariopsis barronii</i>	1.3	30H-CC	32F-CC	283.64	292.92	288.28
DIAT	LO <i>Shionodiscus tetraoestrupii</i> var. <i>reimeri</i>	1.3	34F-CC	36X-CC	302.50	316.87	309.68
DIAT	FO <i>Asteromphalus hyalinus</i>	1.6	36X-CC	37X-CC	316.87	324.22	320.54
DIAT	FO <i>Fragilariopsis rhombica</i>	1.4	39X-CC	40X-CC	344.31	353.46	348.88
DIAT	FO <i>Fragilariopsis separanda</i>	1.4	39X-CC	40X-CC	344.31	353.46	348.88
DIAT	LO <i>Rouxia antarctica</i>	1.5	41X-CC	42X-CC	359.77	372.05	365.91
DIAT	FO <i>Fragilariopsis obliquecostata</i>	1.7	44X-CC	45X-CC	387.40	399.98	393.69
DIAT	LO <i>Proboscia barboi</i>	1.8	45X-CC	46X-CC	399.98	409.51	404.74
DIAT	LO <i>Thalassiosira inura</i>	1.8–2.0	45X-CC	46X-CC	399.98	409.51	404.74
RAD	LO <i>Cycladophora pliocenica</i>	1.81	46X-4, 70–71	46X-CC	406.70	409.48	408.09
RAD	FO <i>Phormospyris antarctica</i>	1.88	46X-CC	47X-CC	409.48	415.99	412.74
DIAT	LO <i>Thalassiosira kolbei</i>	1.9	47X-CC	48X-CC	416.02	425.94	420.98
DIAT	LO <i>Thalassiosira torokina</i>	1.9	47X-CC	48X-CC	416.02	425.94	420.98
DIAT	LO <i>Fragilariopsis bohaty</i>	1.9	48X-CC	49X-1, 75–75	425.94	430.95	428.44
RAD	LO <i>Eucyrtidium calvertense</i>	1.92	48X-CC	49X-CC	425.91	436.43	431.17
RAD	LO <i>Helotholus vema</i>	2.4	48X-CC	49X-CC	425.91	436.43	431.17
RAD	LO <i>Desmospyris spongiosa</i>	2.47	48X-CC	49X-CC	425.91	436.43	431.17
DIAT	LO <i>Actinocyclus fasciculatus</i>	2.0	49X-1, 75–75	49X-2, 75–75	430.95	432.43	431.69
DIAT	FO <i>Fragilariopsis kerguelensis</i>	2.3	49X-2, 75–75	49X-3, 75–75	432.43	433.93	433.18
DIAT	FO <i>Shionodiscus tetraoestrupii</i> var. <i>reimeri</i>	2.3	49X-2, 75–75	49X-3, 75–75	432.43	433.93	433.18
DIAT	FO <i>Porosira pseudodenticulata</i>	2.3	48X-CC	49X-1, 75–75	425.94	430.95	428.44
DIAT	FO <i>Shionodiscus gracilis</i>	2.3	48X-CC	49X-1, 75–75	425.94	430.95	428.44
DIAT	LO <i>Thalassiosira vulnifica</i>	2.2	49X-3, 74–75	49X-4, 74–75	433.93	435.44	434.69
DIAT	FO <i>Rouxia leventerae</i>	2.5	49X-4, 74–75	49X-CC	435.44	436.46	435.95
DIAT	LO <i>Fragilariopsis interfrigidaria</i>	2.4	49X-4, 74–75	49X-CC	435.44	436.46	435.95
DIAT	LO <i>Fragilariopsis interfrigidaria</i>	2.4	49X-4, 74–75	49X-CC	435.44	436.46	435.95
DIAT	LO <i>Thalassiosira insigna</i>	2.6	49X-4, 74–75	49X-CC	435.44	436.46	435.95
DIAT	FO <i>Actinocyclus maccollumii</i>	2.8	49X-4, 74–75	49X-CC	435.44	436.46	435.95
RAD	FO <i>Cycladophora davisiana</i>	2.61	49X-CC	50X-CC	436.46	449.46	442.96
DIAT	LO <i>Fragilariopsis weaveri</i>	2.7	49X-CC	50X-CC	436.46	449.46	442.96
DIAT	FO <i>Actinocyclus actinochilus</i>	2.75	49X-CC	50X-CC	436.46	449.46	442.96
DIAT	FO <i>Actinocyclus fasciculatus</i>	2.7	50X-CC	51X-1, 40–40	449.46	449.80	449.63
DIAT	LO <i>Rouxia heteropolara</i>	3.0	51X-1, 40–40	51X-CC	449.80	450.30	450.05
DIAT	LO <i>Thalassiosira complicata</i>	2.5	51X-CC	52X-CC	450.30	460.20	455.25
DIAT	FO <i>Fragilariopsis bohaty</i>	3.1	51X-CC	52X-CC	450.30	460.20	455.25
DIAT	FO <i>Thalassiosira vulnifica</i>	3.2	51X-CC	52X-CC	450.30	460.20	455.25
DIAT	FO <i>Thalassiosira insigna</i>	3.4	51X-CC	52X-CC	450.30	460.20	455.25
DIAT	LO <i>Fragilariopsis praeinterfrigidaria</i>	3.5	51X-CC	52X-CC	450.30	460.20	455.25
DIAT	LO <i>Rouxia diploneides</i>	2.4	52X-CC	53X-CC	460.20	477.86	469.03
DIAT	LO <i>Thalassiosira striata</i>	2.9	52X-CC	53X-CC	460.20	477.86	469.03
DIAT	FO <i>Fragilariopsis weaveri</i>	3.5	52X-CC	53X-CC	460.20	477.86	469.03
DIAT	LO <i>Fragilariopsis reinholdii</i>	3.0	54X-1, 75–76	54X-2, 75–76	478.96	480.46	479.71

Table T6 (continued).

Type	Event	Published age (Ma)	Top core, section, interval (cm)	Bottom core, section, interval (cm)	Top depth (mbsf)	Bottom depth (mbsf)	Middepth (mbsf)
DIAT	FO <i>Thalassiosira elliptipora</i>	3.3	54X-1, 75–76	54X-2, 75–76	478.96	480.46	479.71
DIAT	LO <i>Thalassiosira jacksonii</i>	3.8	53X-CC	54X-1, 75–76	477.86	478.96	478.41
DIAT	FO <i>Thalassiosira kolbei</i>	4.1	54X-3, 75–75	54X-4, 75–75	481.96	483.46	482.71
RAD	LO <i>Lampromitra coronata</i>	3.72	54X-CC	55X-CC	484.98	488.56	486.77
PALY	LO <i>Batiacasphaera micropapillata</i>	3.74	55X-CC	56X-CC	488.59	504.64	496.61
DIAT	FO <i>Thalassiosira striata</i>	4.5	55X-CC	56X-CC	488.59	504.64	496.61
DIAT	FO <i>Fragilariopsis interfrigidaria</i>	3.9	56X-CC	57X-CC	504.64	509.88	507.26
DIAT	FO <i>Rhizosolenia harwoodii</i>	3.6	58X-CC	59X-CC	519.15	533.73	526.44
DIAT	FO <i>Thalassiosira lentiginosa</i>	4.0	58X-CC	59X-CC	519.15	533.73	526.44
DIAT	LO <i>Rouxia californica</i>	4.2	58X-CC	59X-CC	519.15	533.73	526.44
DIAT	FO <i>Fragilariopsis barronii</i>	4.4	60X-CC	61X-CC	539.05	550.12	544.58
DIAT	FO <i>Rouxia diploneides</i>	4.5	60X-CC	61X-CC	539.05	550.12	544.58
DIAT	LO <i>Fragilariopsis praecurta</i>	4.2	61X-CC	62X-CC	550.12	557.95	554.03
DIAT	LO <i>Fragilariopsis lacrima</i>	3.0	62X-CC	65X-CC	557.95	588.98	573.46
DIAT	LO <i>Denticulopsis delicata</i>	4.45	62X-CC	65X-CC	557.95	588.98	573.46
DIAT	LO <i>Fragilariopsis cylindrica</i>	4.2	65X-CC	68X-CC	588.98	603.17	596.07
DIAT	LO <i>Fragilariopsis aurica</i>	4.2	68X-CC	69X-CC	603.17	614.88	609.02
DIAT	LO <i>Rhizosolenia costata</i>	4.2	68X-CC	69X-CC	603.17	614.88	609.02
DIAT	FO <i>Thalassiosira fasciculata</i>	4.5	68X-CC	69X-CC	603.17	614.88	609.02
DIAT	LO <i>Fragilariopsis arcuata</i>	4.5	68X-CC	69X-CC	603.17	614.88	609.02
RAD	LO <i>Larcopele polyacantha titan</i>	3.48	73X-CC	74X-CC	643.69	653.47	648.58
RAD	LO <i>Lychnocanium grande</i>	4.24–4.55	72X-CC	73X-CC	643.69	653.47	648.58
RAD	FO <i>Helotholus vema</i>	4.59	74X-CC	75X-CC	653.47	672.30	662.89

dominated by *Eucampia antarctica*, *Fragilariopsis kerguelensis*, and *Thalassiosira lentiginosa*. It also contains variable amounts of common Southern Ocean species including *Actinocyclus actinochilus*, *Azpeitia tabularis*, *Fragilariopsis curta*, *Fragilariopsis obliquecostata*, *Fragilariopsis rhombica*, *Fragilariopsis ritscheri*, *Fragilariopsis separanda*, *Porosira glacialis*, *Shionodiscus gracilis*, *Shionodiscus oestrupii*, *Stellarima microtrias*, *Thalassiosira antarctica*, *Thalassiosira oliverana*, *Thalassiosira scotia*, and *Thalassiothrix antarctica* (Figure F12). This assemblage also occurs in Samples 382-U1538A-1H-CC to 10H-CC. *Actinocyclus ingens*, *Hemidiscus karstenii*, and *Rhizosolenia harwoodii* are occasionally reworked in this interval. The lowest stratigraphic occurrence of *Thalassiosira antarctica* was identified in Sample 8H-CC. However, this is not taken to be the true first occurrence (FO) datum of this species (0.65 Ma) because of its position relative to the other last occurrences (LOs) and FOs identified at Site U1538. Similarly, the lowest occurrence of *P. glacialis* (FO = 1.15 Ma) was identified in Sample 15H-CC; however, this is also not likely a true FO datum. Because of its gracile nature, this species is easily destroyed in sediments.

A late Pleistocene assemblage was identified in Samples 382-U1538A-11H-CC to 14H-CC. In addition to the species identified above, *Rouxia leventerae* (LO = 0.14 Ma) has its highest stratigraphic occurrence in Sample 11H-CC. *H. karstenii* (LO = 0.2 Ma) was identified in Sample 13H-CC; this is considered to be the highest stratigraphic occurrence in which the species is not reworked because of its position downcore of *R. leventerae*. *Rouxia constricta* (LO = 0.3 Ma) has a highest stratigraphic occurrence in Sample 15H-CC.

Interval 382-U1538A-16H-CC through 30H-CC represents the middle Pleistocene. The uppermost sample in this interval is taken as the highest in situ stratigraphic occurrence of *A. ingens* and *R. harwoodii*. The uppermost occurrence of *Thalassiosira elliptipora* (LO = 0.7 Ma) was identified in Sample 17H-CC. *Thalassiosira fasciculata* (LO = 0.9 Ma) has a highest stratigraphic occurrence in Sample 22H-1, 74–75 cm. The lowest stratigraphic occurrence of *F.*

separanda (FO = 1.4 Ma) was identified in Sample 25H-CC, and the lowest stratigraphic occurrence of *R. constricta* (FO = 1.4 Ma) was found in Sample 26H-CC.

The highest stratigraphic occurrence of *Fragilariopsis barronii* (LO = 1.3 Ma) in Sample 382-U1538A-32F-CC to the highest stratigraphic occurrence of *Thalassiosira insigna* (LO = 2.6 Ma) in Sample 49X-CC defines an early Pleistocene–late Pliocene age. The lowest occurrence of *A. actinochilus* (FO = 2.75 Ma) was also found in Sample 49X-CC. This interval contains the lowest occurrence of *F. rhombica* (FO = 1.4 Ma) in Sample 39X-CC. Given its position relative to the LO of *F. barronii*, this datum is considered more reliable than the FOs of *F. separanda* and *R. constricta* (1.4 Ma) seen above. All of these species are easily lost to fragmentation and dissolution, which is likely why only one was seen at the appropriate depth. Furthermore, the highest stratigraphic occurrence of *Rouxia antarctica* (LO = 1.5 Ma) was found in Sample 42X-CC. This interval also contains the highest stratigraphic occurrence of *Proboscia barboi* (LO = 1.8 Ma) in Sample 46X-CC. *Thalassiosira kolbei* and *Thalassiosira torokina* both have a highest stratigraphic occurrence in Sample 48X-CC (LO of both = 1.9 Ma). Additionally, the lowest occurrence of *F. kerguelensis* (FO = 2.3 Ma) was identified in Sample 49X-2, 75 cm, and the lowest occurrence of *S. gracilis* (FO = 2.3 Ma) was identified in Sample 48X-CC. Therefore, the lowest occurrence of *F. kerguelensis* is likely a true FO, whereas *S. gracilis* was simply not found below Sample 48X-CC.

Samples 382-U1538A-50X-CC to 53X-CC represent the late Pliocene. This interval contains the highest (Sample 50X-CC) and lowest (Sample 52X-CC) occurrences of *Fragilariopsis weaveri* (LO = 2.7 Ma; FO = 3.5 Ma). The deepest occurrence of *Thalassiosira vulnifica* (FO = 3.2 Ma) was found in Sample 51X-CC. The highest occurrence of *Fragilariopsis praeinterfrigidaria* (LO = 3.5 Ma) was recorded in Sample 53X-CC.

Early Pliocene assemblages occur from Sample 382-U1538A-54X-1, 75–76 cm, to the deepest recovered sediments in Sample 75X-CC. Sample 54X-1, 75–76 cm, contains the stratigraphically

Figure F11. Biostratigraphic age-depth plot, Hole U1538A. FO datums are plotted using the median depth between the upper sample where the fossil was observed and the lower sample where it was not observed (Table T6). LO datums are plotted using the median depth between the upper sample where a species was not seen and the lower sample where it was seen.

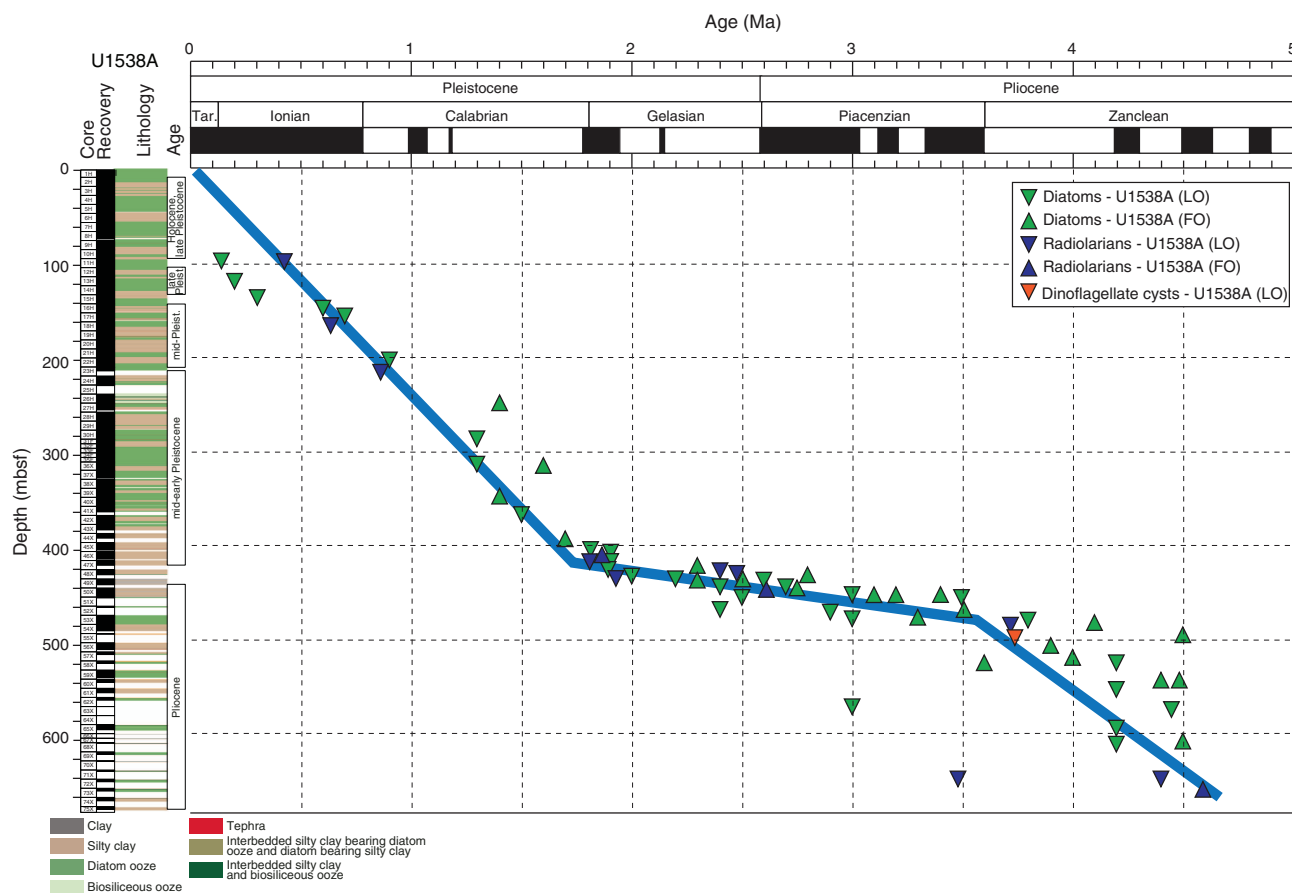


Table T7. Diatom occurrences, abundance, and preservation state, Site U1538. [Download table in CSV format.](#)

highest recorded instance of *Thalassiosira jacksonii* (LO = 3.8 Ma). The deepest occurrence of *Fragilariopsis interfrigidaria* (FO = 3.9 Ma) was found in Sample 56X-CC. *Fragilariopsis aurica* (LO = 4.2 Ma) has a highest stratigraphic occurrence in Sample 57X-1, 75–76 cm. The deepest occurrence of *F. barronii* (FO = 4.4 Ma) was identified in Sample 60X-CC. The highest stratigraphic occurrence of *Denticulopsis delicata* (LO = 4.45 Ma) was found in Sample 65X-CC. *Fragilariopsis arcuata* (LO = 4.5 Ma) has a highest stratigraphic occurrence in Sample 69X-CC. The assemblage in the lowest analyzed interval (Sample 75X-CC) contains *Denticulopsis simonsenii*, *F. aurica*, *Fragilariopsis praecurta*, *F. praeinterfrigidaria*, *Fragilariopsis reinholdii*, and *S. oestrupii* along with other species of lesser biostratigraphic significance.

Radiolarians

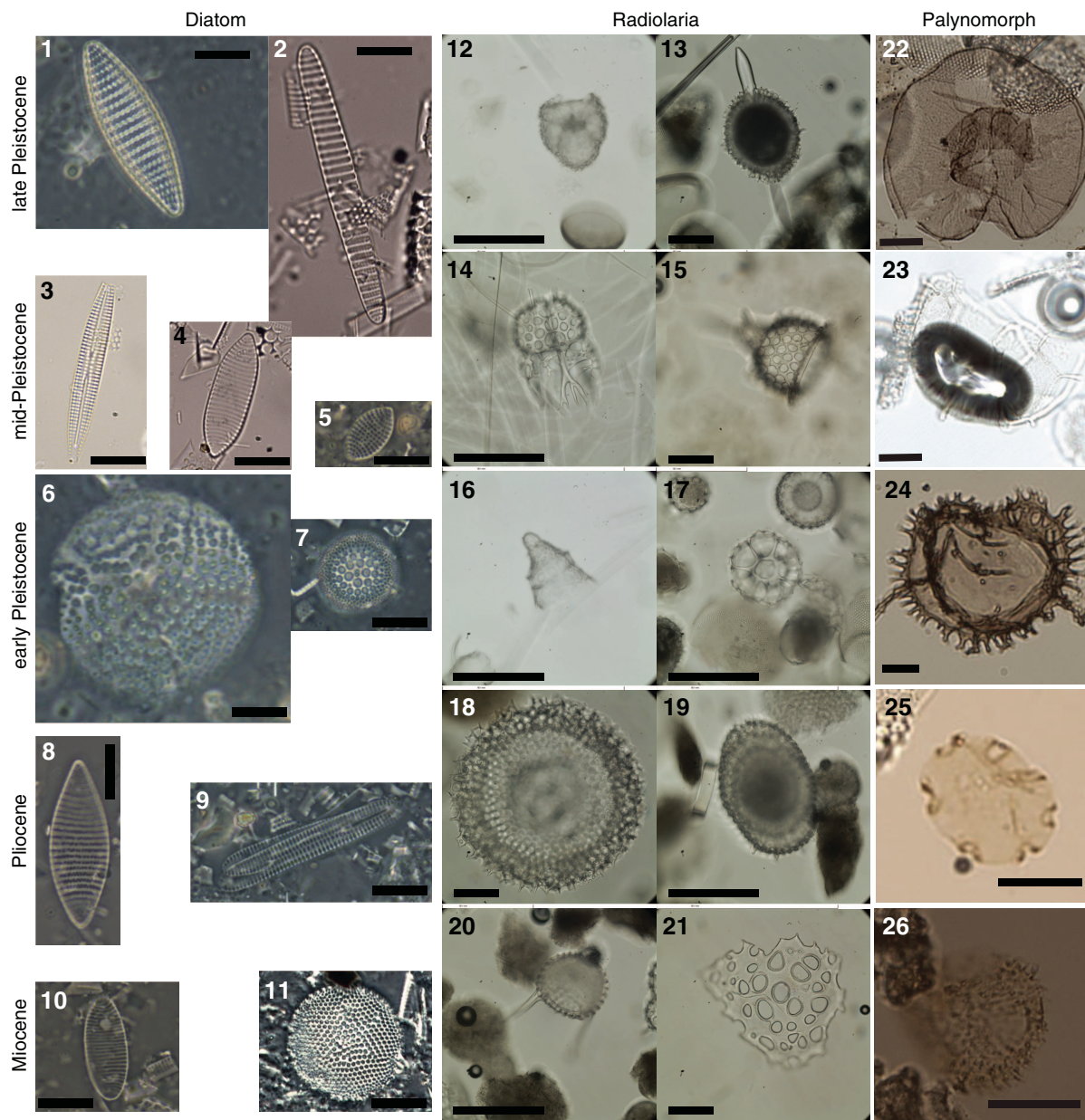
Radiolarians are common to abundant and well preserved in most samples examined; in the first two core catcher samples, radiolarians are rare because of dilution by diatoms (Table T8). Based on the LO of *Stylatractus universus* (0.41 Ma; Figure F12), the base of the Omega Zone occurs between Samples 382-U1538A-10H-CC and 11H-CC. The radiolarian assemblage of this zone is dominated by *Antarctissa denticulata*. Other species commonly present in these samples are *Cycladophora davisiana*, *Cycladophora*

cornutoides, *Antarctissa strelkovi*, and *Actinomma boreale*. Samples 13H-CC and 14H-CC contain Pliocene species, such as *Helotholus vema*, that are interpreted to be reworked.

Sample 382-U1538A-18H-CC corresponds to the Psi Zone based on the presence of *Antarctissa cylindrica* (LO = 0.64 Ma). The LO of *Cycladophora pliocenica* (1.81 Ma) occurs between Samples 46X-4, 70–71 cm, and 46X-CC. Samples 23H-CC to 46X-4, 70–71 cm, are assigned to the Chi Zone. The top of this zone is defined according to the highest stratigraphic occurrence of *Pterocanium trilobum* (LO = 0.86 Ma), which occurs between Samples 23H-CC and 24H-1, 74–75 cm. The base of this zone occurs between Samples 46X-CC and 47X-CC based on the LO of *Phormospyris antarctica* (1.92 Ma). The LO of *Eucyrtidium calvertense* (1.92 Ma) also marks the base of the Chi Zone, but in Hole U1538A this event was found between Samples 48X-CC and 49X-CC at the same depth as the LO of *H. vema* (2.4 Ma). This suggests that the true LO datum of *E. calvertense* might occur higher in the core. However, it would require higher resolution sampling to determine it correctly.

Samples 382-U1538A-49X-CC to 75X-CC are assigned to the Upsilon Zone based on the presence of *H. vema* and *Desmospyris spongiosa* (LO = 2.47 Ma). The absence of *C. davisiana* below Sample 49X-CC and the absence of species such as *Lampromitra coronata* and *Larcopyle polyacantha titan* correspond to the upper part of the Upsilon Zone. The LO of *L. coronata* (3.72 Ma) occurs between Samples 54X-CC and 55X-CC, indicating the lower Upsilon Zone.

Figure F12. Biostratigraphically important diatoms and radiolarians and selected palynomorphs found at Expedition 382 sites. Diatoms (scale bars = 10 μm): 1. *Fragilariopsis kerguelensis* (382-U1538A-16H-CC), 2. *Fragilariopsis obliquecostata* (382-U1537A-3H-CC), 3. *Rouxia constricta* (382-U1536A-14H-CC), 4. *Fragilariopsis rhombica* (382-U1537A-3H-CC), 5. *Fragilariopsis separanda* (382-U1536A-10H-1, 75 cm), 6. *Actinocyclus fasciculatus* (382-U1538A-49X-3, 75 cm), 7. *Shionodiscus oestrupii* var. *reimeri* (382-U1538A-45X-CC), 8. *Fragilariopsis barronii* (382-U1536A-40F-CC), 9. *Rouxia antarctica* (382-U1538A-51X-1), 10. *Fragilariopsis aurica* (382-U1536C-40F-CC), 11. *Thalassiosira miocenica* (382-U1536E-22R-CC). Radiolarians (scale bars = 50 μm): 12. *Antarctissa cylindrica* (382-U1537A-10H-CC), 13. *Stylatractus univertus* (382-U1536A-14H-CC), 14. *Phormospyris antarctica* (382-U1538A-6H-CC), 15. *Cycladophora pliocenica* (382-U1534A-29F-CC), 16. *Cycladophora davisiana* (382-U1537A-13H-CC), 17. *Helotholus? vema* (382-U1537D-40F-CC), 18. *Lampromitra coronata* (382-U1536E-4R-CC), 19. *Larcopyle polyacantha titan* (382-U1538A-73X-CC), 20. *Lychnocanium grande* (73X-CC), 21. *Acrosphaera labrata* (382-U1536E-18R-CC). Palynomorphs (scale bars = 20 μm): 22. *Selenopemphix* sp. 1 sensu Esper and Zonneveld (2007) (382-U1536A-3H-CC), 23. *Impagidinium* spp. (382-U1534A-9H-CC), 24. *Selenopemphix dionaeacysta* (16F-CC), 25. *Nothofagidites flemingii* (382-U1538A-60X-CC), 26. *Operculodinium? eirikianum* (382-U1536E-26R-CC).



Sample 382-U1538A-74X-CC contains the LO of *L. polyacantha titan* (3.48 Ma). However, because this species was only found in one sample and given its lower position relative to the observed LO of *L. coronata*, which is older, we suggest that this is not the real datum; a more systematic sampling at shallower levels would be needed to find the correct depth for this event. The LO of *Lychnocanium grande* (4.22–4.5 Ma) occurs between Samples 72X-CC and

73X-CC. The abundance of *Helotholus praevema* increases progressively with depth below Sample 62X-CC; this is typical in early Pliocene sediments in the Southern Ocean (Weaver, 1983). The base of the Upsilon Zone was placed immediately below the lowest occurrence of *H. vema* (FO = 4.59 Ma), which occurs between Samples 74X-CC and 75X-CC.

Palynology

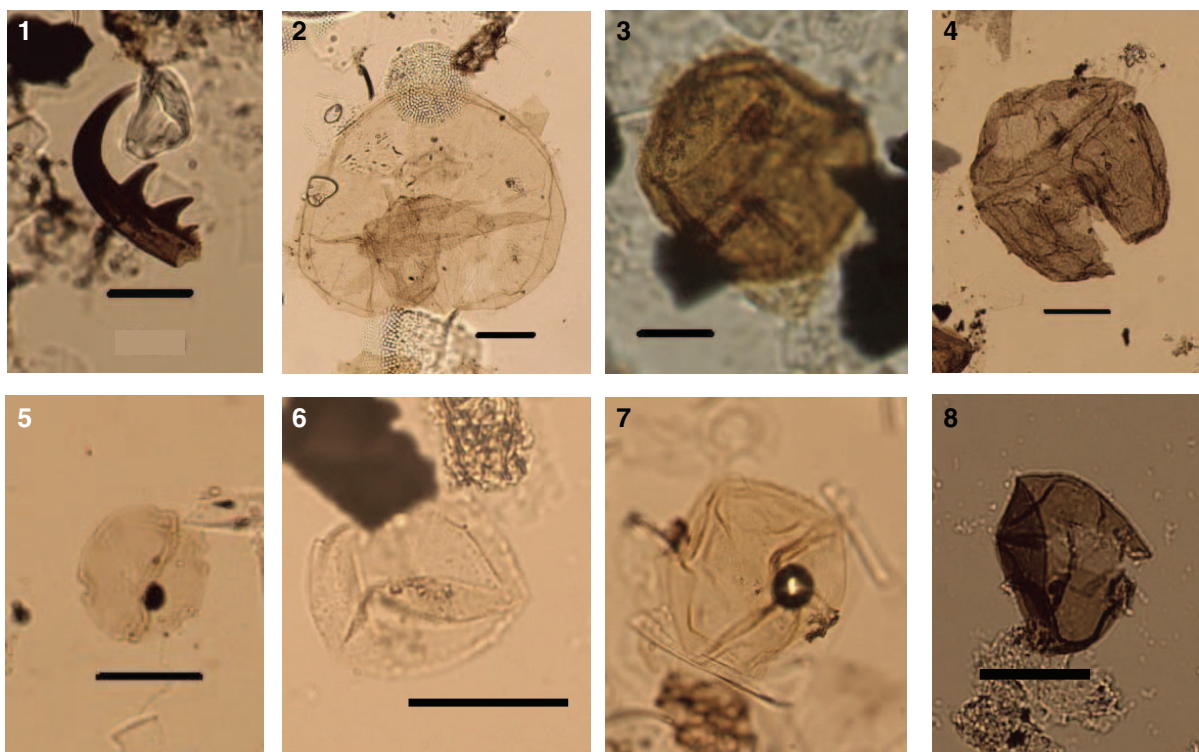
A total of 30 core catcher samples from Hole U1538A were processed and analyzed for palynomorph assemblages. Palynomorphs (dinocysts, acritarchs, prasinophytes, pollen, spores, and copepod and fungi remains) were identified in all samples processed. The presence of marine palynomorphs and semiquantitative estimates of the abundance of the different palynofacies together with the processing method used is accessible in Table T9. Supportive age control from dinocysts is presented in Table T6. Selected palynomorphs are shown in Figure F13.

All samples analyzed have a broad range in preservation, relative abundance, reworking, and diversity of palynomorphs. A few samples (Cores 382-U1538A-50X, 51X, 74X, and 75X) are barren of in situ dinocysts. In situ dinocyst assemblages normally consist of the heterotrophic protoperidinioid genera *Brigantedinium* spp. and *Selenopemphix* spp. Reworked dinocysts of Cenozoic origin were observed in Samples 17H-CC, 26H-CC, and 40X-CC. Prasinophyte algae *Leiosphaeridia* sp. and *Cymatiosphaera* sp. were observed in most samples below 92 mbsf. Presumed contemporaneous *Podocarpidites* sp. and *Nothofagidites* sp. miospores were found in a few samples (Figure F12), whereas reworked miospores occur in all samples. The reworked specimens include a few Cenozoic forms but are mainly composed of Permian to Mesozoic miospores. Other palynofacies such as acritarchs, foraminifer test linings, pyritized si-

Table T8. Radiolarian occurrences, preservation, and abundance, Site U1538. [Download table in CSV format.](#)

Table T9. Palynomorph occurrences, preservation, and abundance, Site U1538. [Download table in CSV format.](#)

Figure F13. Selected palynomorphs. All scale bars = 20 μm . 1. Copepod remain (382-U1538A-4H-CC). 2. *Selenopemphix* sp. 1 sensu Esper and Zonneveld (2007) (4H-CC). 3. *Deflandrea antarctica* (10H-CC). 4. *Nucicla umbiliphora* (17H-CC). 5. *Nothofagidites flemingii* (38X-CC). 6. *Batiacasphaera micropapillata* (56X-CC). 7. *Leiosphaeridia* sp. (29H-CC). 8. *Brigantedinium simplex* (71X-CC).



liceous microfossils, copepod remains, and amorphous organic matter were also commonly recorded throughout Site U1538. Most of the dinocysts found are long ranging and have poor age diagnostics. The only age constraint from dinocysts at Site U1538 is the occurrence of *Batiacasphaera micropapillata* (LO = 3.74 Ma) in Sample 56X-CC, giving supportive age control to the Pliocene.

Marine sedimentary ancient DNA

Ancient DNA

Samples for ancient DNA (aDNA) analysis were collected from Holes U1538C and U1538D following the catwalk sampling methodology (see [Biostratigraphy](#) in the Expedition 382 methods chapter [Weber et al., 2021a]). One mudline sample (~12 mL) was taken, and two sediment samples were collected from Section 382-U1538C-1H-1 (top and bottom of the section). For Sections 1H-2 through 8H-3, the bottom of most sections was sampled to capture the Holocene and glacial–interglacial transitions as far back as Termination II (as estimated by preliminary physical property data). Additional samples were collected at the bottom of Sections 382-U1538C-10H-5, 382-U1538D-14H-1, and 14H-6 to test for DNA preservation in even older material. All samples were immediately stored at -80°C and will be analyzed at the home laboratory, Australian Centre for Ancient DNA (ACAD), Adelaide (see [Biostratigraphy](#) in the Expedition 382 methods chapter [Weber et al., 2021a]).

Contamination control

An air control sample (empty tube) and a drilling fluid control with perfluoromethyl decaline (PFMD) tracer (12 mL) were collected after aDNA sampling from Hole U1538C. Chemical tracers (PFMD) were run at a flow rate of 1 ppm, as at Site U1537. Inner (center of core) and outer (periphery) sediment samples for PFMD

testing were collected at the same depths as aDNA samples. Samples were stored at 4°C and analyzed approximately 7 days after collection. PFMD was detected in most samples taken from the periphery of the core in concentrations of 0.3 ± 0.25 ng/mL on average (minimum = 0; maximum = 1.14 ng/mL). Only three samples from the core center (Sections 382-U1538C-4H-1, 10H-1, and 382-U1538D-14H-1) had PFMD concentrations above the detection limit (0.4, 0.6, and 0.4 ng/mL, respectively) (i.e., drilling fluid contamination of the aDNA samples collected at these depths cannot be excluded), so they will be analyzed and evaluated with caution.

Summary

Diatom, radiolarian, foraminifer, and palynomorph biostratigraphic results are consistent for all samples from Hole U1538A. These analyses showed 75 biostratigraphic events (Table T6). Based on these events, we estimate sedimentation rates of ~22 cm/ky between the seafloor and 432 mbsf, ~2.5 cm/ky from 432 to 469 mbsf, and ~12 cm/ky from 447 mbsf to the bottom of the site (Figure F11). Estimated sedimentation rate changes may indicate variations in past ocean current strength, IBRD delivery, taphonomic processes, and/or paleoproductivity. One sample (382-U1538A-70X-CC) contains a Pleistocene assemblage at great depth and likely represents fall-in during coring operations. Our analyses reveal an extremely high sedimentation rate during the Holocene–Pleistocene and early Pliocene and a very low sedimentation rate during the late Pliocene.

Paleomagnetism

Paleomagnetic measurements were made on 281 APC and 20 HLAPC core sections from Holes U1538A ($N = 191$ APC/20 HLAPC), U1538B ($N = 6$ APC), U1538C ($N = 7$ APC), and U1538D ($N = 77$ APC) to investigate the natural remanent magnetization (NRM). In addition, 374 XCB sections from Hole U1538A were analyzed, although these have highly variable continuity and quality. All archive-half measurements were made on the initial magnetization and the magnetization following peak alternating field (AF) demagnetization at 10 and 15 mT. As a result of unsuccessful tests and application of the Icefield MI-5 core orientation tool throughout Expedition 382 (see [Paleomagnetism](#) in the Expedition 382 methods chapter [Weber et al., 2021a]), orientation data were not collected for any core at Site U1538.

A total of 339 discrete cube samples were taken from the working halves from Holes U1538A (all cores) and U1538C (Cores 382-U1538C-6H and 7H only). In general, we took one sample per section. We measured the NRMs of 334 cubes on the superconducting rock magnetometer (SRM) using the discrete sample tray (the rest were unoriented cubes taken for rock magnetic analysis), followed by stepwise demagnetization at peak AF steps of 5, 10, and 15 mT. A subset of 95 cubes selected to span a stratigraphic range where the presence of greigite was suspected was stepwise demagnetized up to 20 mT at 5 mT increments followed by demagnetization to 50 mT at 10 mT intervals to investigate the demagnetization behavior of the NRM. For all NRM demagnetization measurements at 10 mT and subsequent steps, we demagnetized and measured the specimens in three orthogonal positions (top-away, top-right, and away-bottom settings in the SRM measurement program) and averaged the three measurements to insure data quality.

Natural remanent magnetization

The data from the 15 mT step on the archive halves prior to any editing for Holes U1538A, U1538B, U1538C, and U1538D are shown as black dots in Figures F14, F15, F16, and F17, respectively. Cyan dots show the data after editing (see [Paleomagnetism](#) in the Site U1536 chapter [Weber et al., 2021b]), averaging core declinations, and adjusting each core to have a mean normal declination of 90° for purposes of plotting. We assess the reliability of polarity determinations in several ways:

- Examination of lithologic descriptions and X-ray images for disturbance,
- Stepwise AF demagnetization of discrete samples,
- Examination of histograms of inclinations (which should be bimodal at the expected geocentric axial dipole [GAD] inclinations at the site; see [Paleomagnetism](#) in the Expedition 382 methods chapter [Weber et al., 2021a]) and declinations (which should be uniformly distributed owing to presumably random orientations of core double lines), and
- Agreement of the interpreted magnetostratigraphy with available biostratigraphic constraints.

Tables T10, T11, T12, and T13 are the DESClogik tables used to perform the editing for disturbance noted in visual core description, and Tables T14, T15, T16, and T17 document the X-ray disturbance observations used to edit data from Holes U1538A–U1538D.

Discrete sample data

We subjected all oriented cube samples to demagnetization up to 15 mT. An early warning of problematic specimens is the circular standard deviation (CSD) of the three positions averaged during the demagnetization procedure. High CSDs could be related to measuring weak specimens on the shipboard instrument situated in a magnetically noisy environment or from the acquisition of spurious remanences during AF demagnetization such as anhysteretic remanent magnetization or gyroremanent magnetization (GRM).

The behavior of the CSDs for Site U1538 is summarized in Figure F18. Figure F18A is a histogram of the CSDs. Although most of the specimens have CSDs <15°, a long tail of higher CSDs extends to >80°. Figure F18B shows CSDs plotted against the magnetic moment after 15 mT peak AF demagnetization of the samples. Although some of the high CSD samples have weak magnetizations, by far the majority are surprisingly strong, and the high CSD is likely related to the acquisition of spurious induced remanences. In Figure F18C, CSDs are plotted in the context of polarity determinations. The low CSD (<15°) discrete specimens have a bimodal distribution consistent with two polarities, but the high CSD data are unimodal with a peak centered on zero. No polarity determination can be made based on these specimens.

To further investigate the origin of high CSDs, we selected a set of 95 discrete samples for stepwise AF demagnetization experiments up to an AF of 50 mT. Representative examples of the behavior during demagnetization are shown in Figure F19, including examples of normal, reversed, and indeterminate polarities. Typical behavior for a normal polarity (inclination up) specimen is shown in Figure F19A, and a reversed polarity is shown in Figure F19B. An example of a poorly behaved specimen of indeterminate polarity is

Figure F14. Intensity of remanence, declination, and inclination of NRM at 15 mT AF demagnetization level, Hole U1538A. Horizontal dashed lines = section breaks, black dots = original (unedited) data, large cyan dots = edited and adjusted values as described in text, red stars = discrete samples, vertical dashed lines in inclination = GAD predicted inclination values. (Continued on next three pages.)

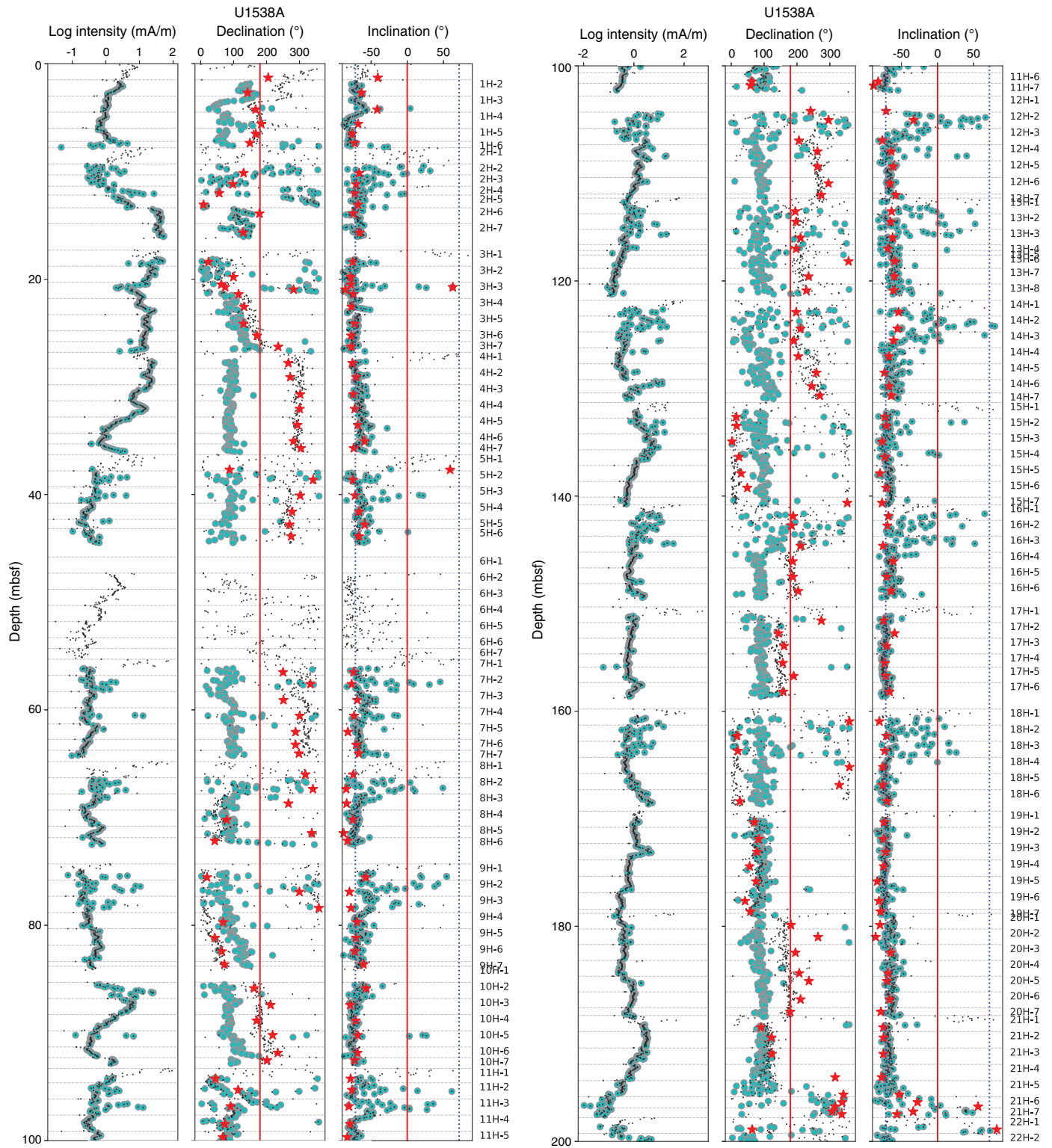


Figure F14 (continued). (Continued on next page.)

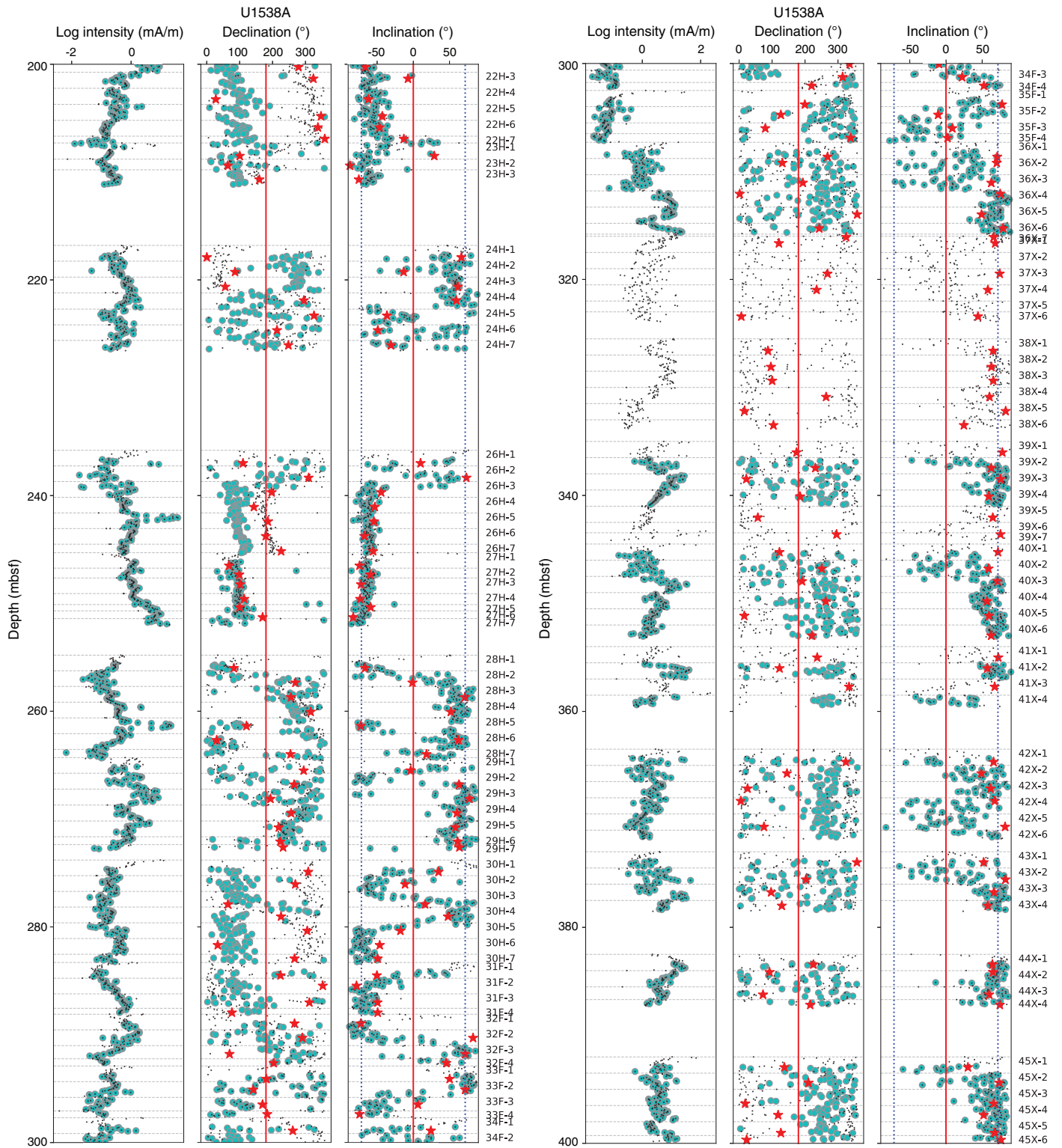


Figure F14 (continued). (Continued on next page.)

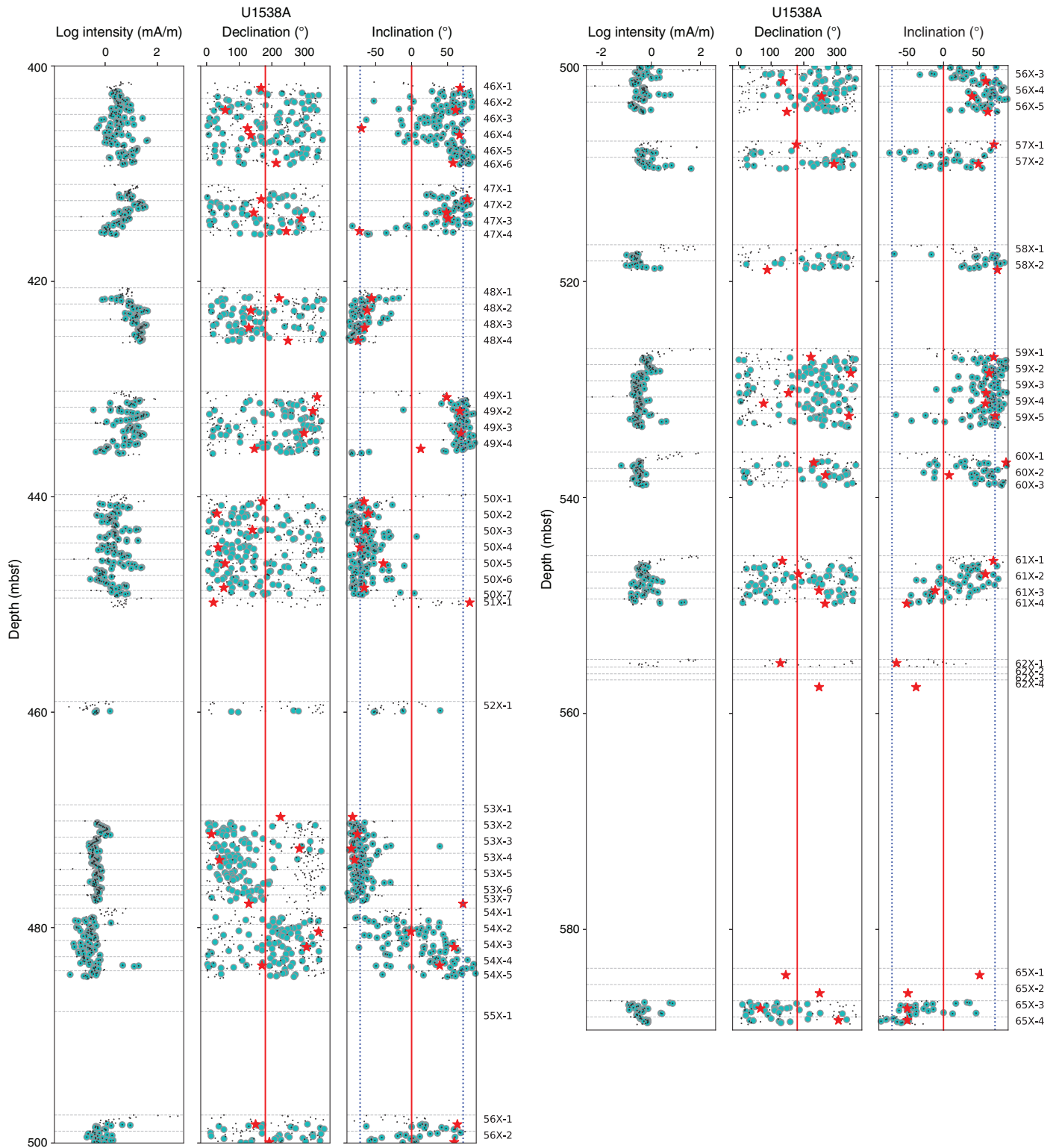


Figure F14 (continued).

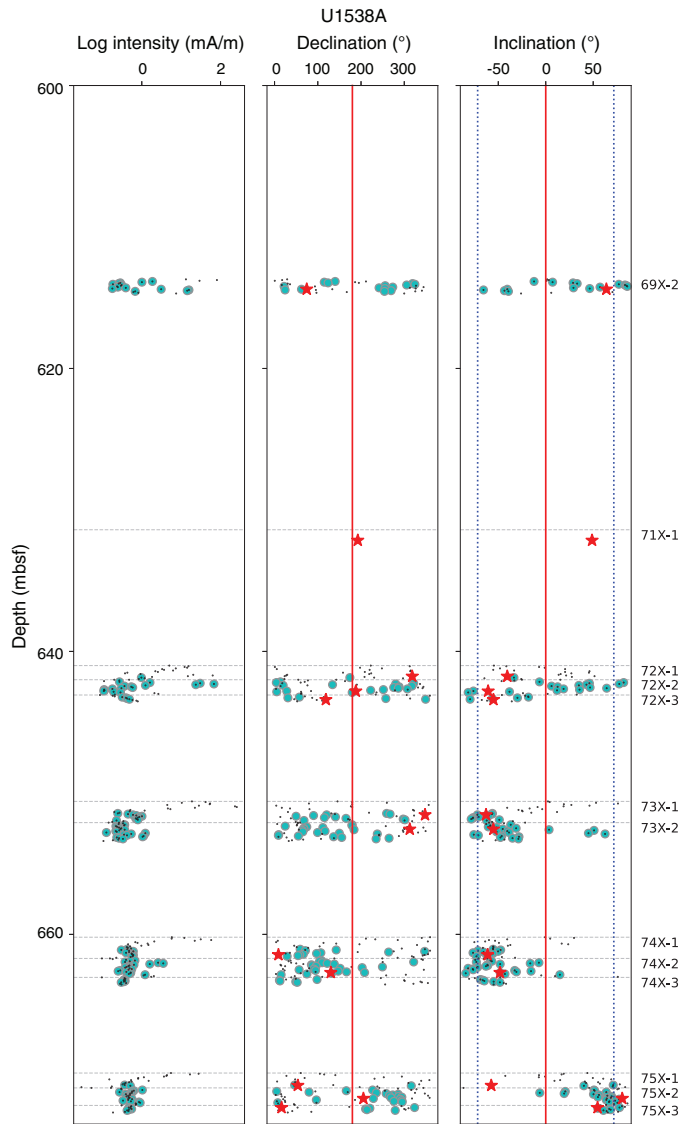


Figure F15. Intensity of remanence, declination, and inclination of NRM at 15 mT AF demagnetization level, Hole U1538B. Horizontal dashed lines = section breaks, black dots = original (unedited) data, large cyan dots = edited and adjusted values as described in text, red stars = discrete samples, vertical dashed lines in inclination = GAD predicted inclination values.

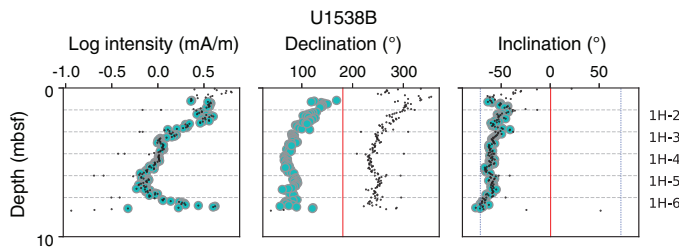


Figure F16. Intensity of remanence, declination, and inclination of NRM at 15 mT AF demagnetization level, Hole U1538C. Horizontal dashed lines = section breaks, black dots = original (unedited) data, large cyan dots = edited and adjusted values as described in text, red stars = discrete samples, vertical dashed lines in inclination = GAD predicted inclination values. (Continued on next page.)

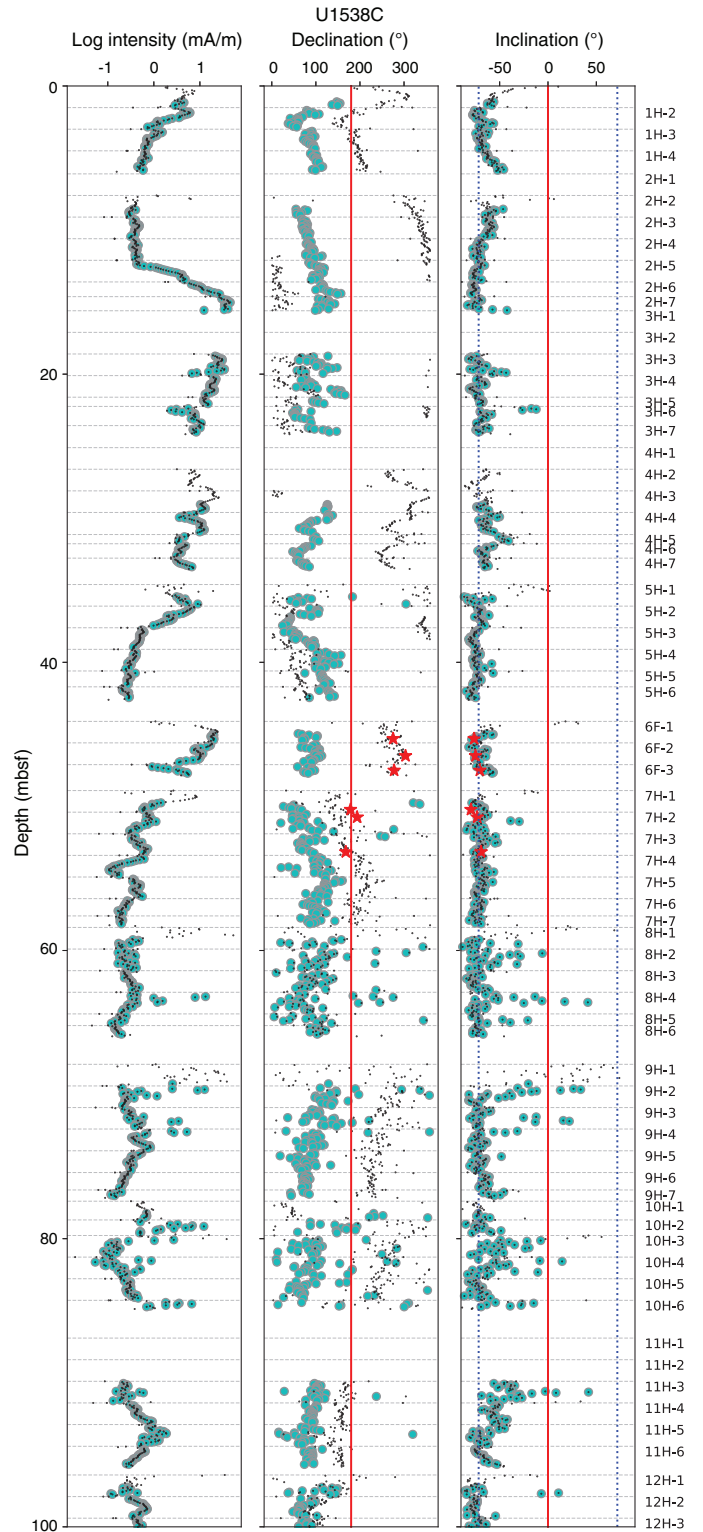
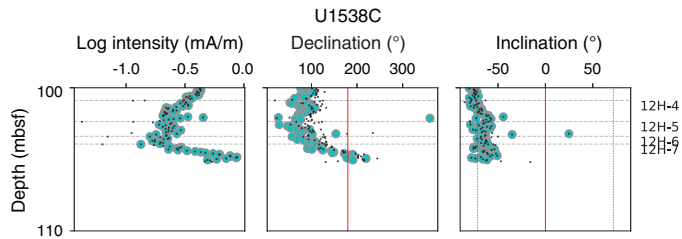


Figure F16 (continued).



shown in Figure F19C. In the first two figures, we observed smooth decay to the origin and removal of a very minor drilling overprint in a downward direction, generally removed by the 10 mT step. In Figure F19C, the magnetization appears unstable and grows in strength between the 20 mT step and the 50 mT step. We attribute this behavior to the acquisition of a GRM, often associated with the presence of the iron sulfide greigite (Roberts et al., 2011). We calculated the ratio of remanence remaining after demagnetization to 50 mT to that remaining after 30 mT and took a ratio greater than unity as a further indication of unreliable remanence.

Despite high CSDs and anomalous demagnetization behavior in some discrete samples, nearly all of the discrete sample data (red stars) agree well with the archive-half measurements in Figures F1, F15, F16, and F17, suggesting consistent observations between the two methods. Note that the declinations of the discrete samples were not adjusted, so they should be compared with the small black dots and not the adjusted cyan dots from the archive-half measurements. Discrete sample inclination data measured after demagnetization at 15 mT are also plotted along with the archive-half measurements in Figure F20. Low CSDs are plotted as red stars, high CSDs are plotted as white squares, and greater than unity 50 to 30 mT remanence ratios are plotted as an X.

Magnetic polarity stratigraphy

The preliminary magnetostratigraphic interpretations are based on the inclinations from archive-half and discrete sample measurements using only the discrete samples with low CSDs at the 15 mT step and ratios of remanence between the 50 and 30 mT steps less than unity (Figure F20). We defined polarity transition intervals as described in Paleomagnetism in the Site U1536 chapter (Weber et al., 2021b) with the additional constraint that high CSD and high remanence ratio intervals were left uninterpreted (shown in gray). The archive-half data from the upper portion of the hole was transformed to a “heat map” made from kernel density estimates (KDEs) for 5 m bins (left panel in Figure F20).

Our preferred correlations to the geomagnetic polarity time-scale (GPTS2012) are shown as red lines, and the depth ranges for polarity transitions are listed in Table T18. Hole U1538A preserves a succession of normal and reversed polarity zones that span Chrons C1n (Brunhes) to C3r (mid Gilbert) with several subchrons missing.

An age-depth plot for the paleomagnetic tie points compared to the biostratigraphic tie points is shown in Figure F21. A seventh order polynomial fit through the paleomagnetic tie points is used to illustrate the age-depth relationship. We also show the positions of the distinctive seismic horizons and their likely ages in the figure.

Figure F17. Intensity of remanence, declination, and inclination of NRM at 15 mT AF demagnetization level, Hole U1538D. Horizontal dashed lines = section breaks, black dots = original (unedited) data, large cyan dots = edited and adjusted values as described in text, vertical dashed lines in inclination = GAD predicted inclination values. (Continued on next page.)

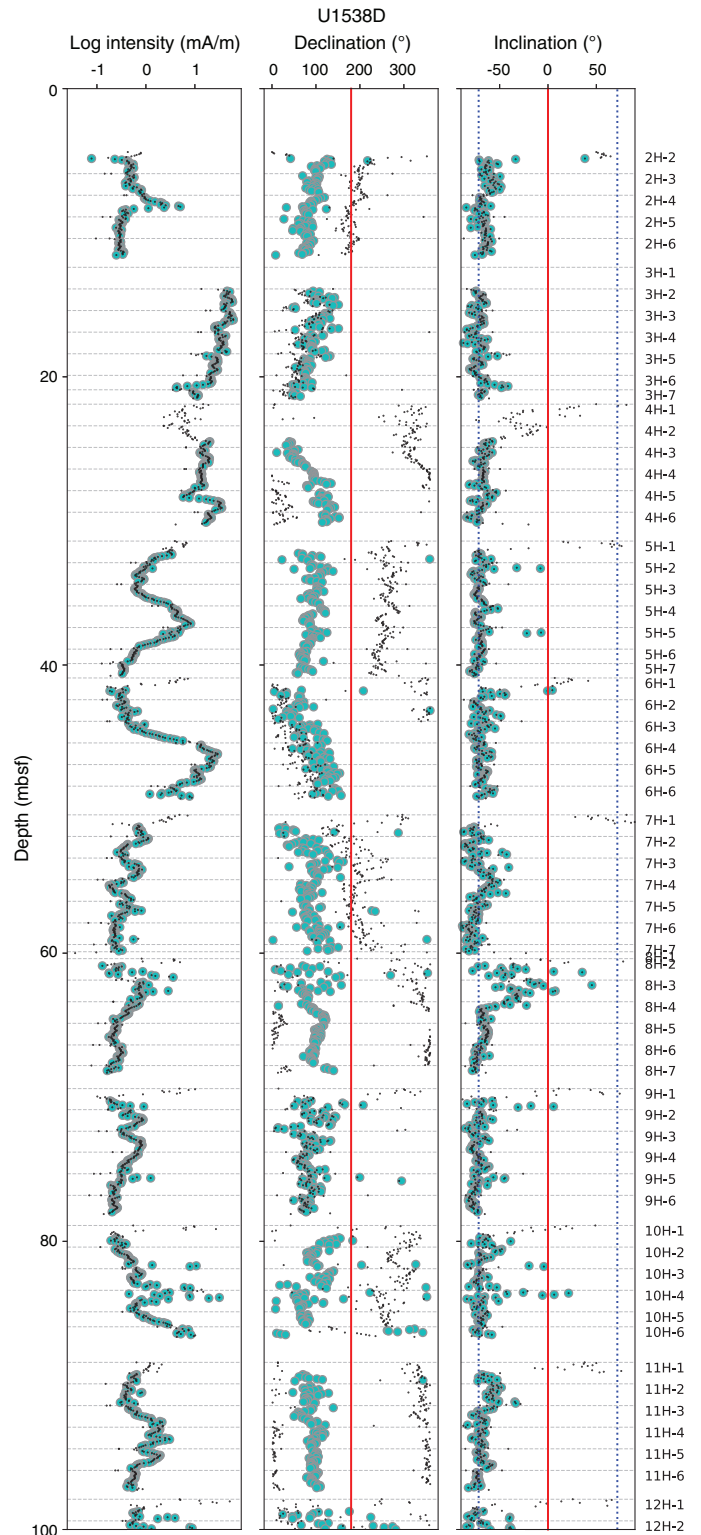
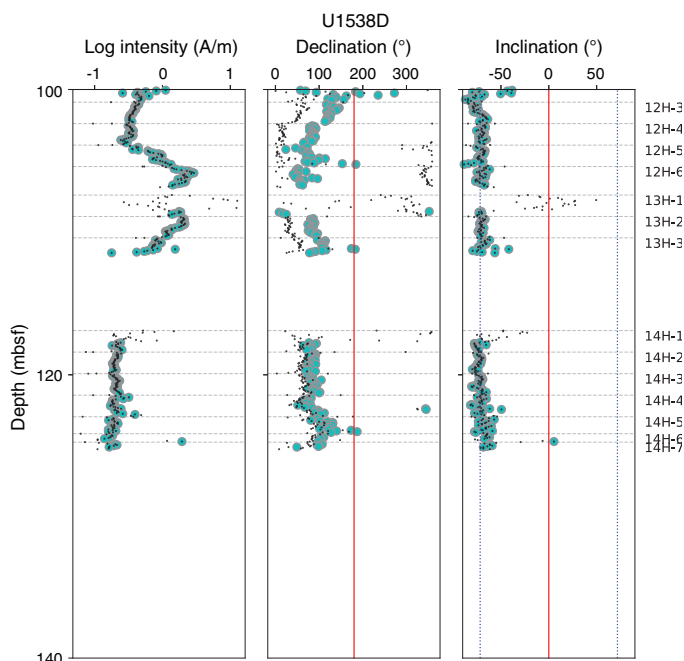


Figure F17 (continued).



Summary

Site U1538 APC cores record a succession of normal and reversed polarity zones; however, there are likely diagenetic alterations, particularly in middle Pleistocene sediments, that complicate the interpretation of the magnetostratigraphy. Paleomagnetic measurements made on archive halves were subjected to several levels of quality control tests using discrete samples, removal of intervals affected by large-scale coring-induced disturbance as determined during visual core description, and removal of intervals with centimeter-scale deformation as determined from inspection of X-rays of every core section. At this site, we introduced a new measure of quality control involving stepwise AF demagnetization and measuring the strength of remanence after 50 mT compared to that done previously at 30 mT to monitor for the acquisition of remanence with progressive peak AF. We did this to

Table T10. Intervals of high-intensity core disturbance as determined by visual inspection during core description, Hole U1538A. [Download table in CSV format.](#)

Table T11. Intervals of high-intensity core disturbance as determined by visual inspection during core description, Hole U1538B. [Download table in CSV format.](#)

Table T12. Intervals of high-intensity core disturbance as determined by visual inspection during core description, Hole U1538C. [Download table in CSV format.](#)

Table T13. Intervals of high-intensity core disturbance as determined by visual inspection during core description, Hole U1538D. [Download table in CSV format.](#)

Table T14. Intervals of disturbed sediment excluded from paleomagnetic determinations as determined from inspection of X-radiographs and core section photographs, Hole U1538A. [Download table in CSV format.](#)

Table T15. Intervals of disturbed sediment excluded from paleomagnetic determinations as determined from inspection of X-radiographs, Hole U1538B. [Download table in CSV format.](#)

Table T16. Intervals of disturbed sediment excluded from paleomagnetic determinations as determined from inspection of X-radiographs, Hole U1538C. [Download table in CSV format.](#)

Table T17. Intervals of disturbed sediment excluded from paleomagnetic determinations as determined from inspection of X-radiographs, Hole U1538D. [Download table in CSV format.](#)

detect the presence of the authigenic ferrimagnetic mineral greigite, a product of diagenesis and a complicating factor in sedimentary magnetizations (see Roberts et al., 2011). Based on this test, we excluded many more intervals, including the interval that likely spans the Matuyama/Brunhes boundary. Nonetheless, several polarity intervals were interpretable, including Chrons C1r.1n (Jaramillo), C2n (Olduvai), and C3n (Gauss) and with lesser confidence some of the subchrons of Chron C3n (Cochiti to Sidufjall).

Figure F18. Behavior of CSD at 15 mT demagnetization step for discrete specimens, Hole U1538A. A. Histogram of CSDs. B. CSD vs. remanence intensity. C. Histogram of inclinations for all archive-half measurements, discrete specimens with low CSD (<15°), and discrete specimens with high CSDs.

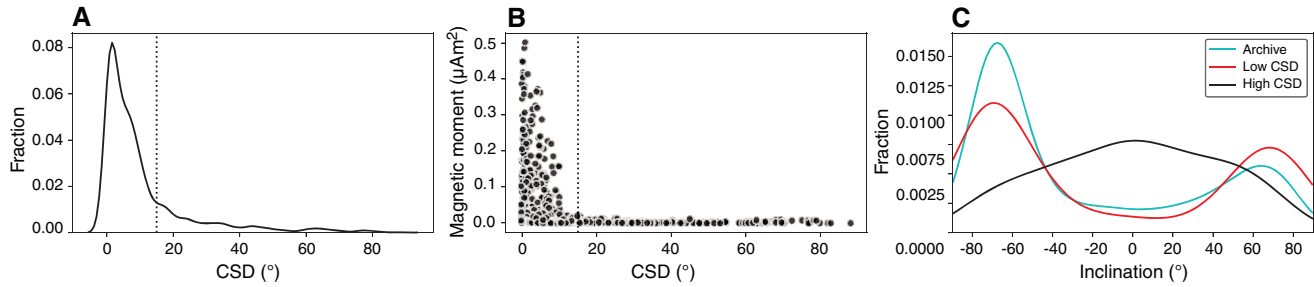


Figure F19. Representative vector endpoint diagrams showing progressive AF demagnetization behavior, Hole U1538A. Demagnetization steps: 1 = NRM, 2 = 5 mT, 3 = 10 mT, 4 = 15 mT, 5 = 20 mT, 6 = 30 mT, 7 = 40 mT, 8 = 50 mT. Green = vector magnitude change during AF demagnetization, purple = magnetic moment of sample. A. Normal specimen. B. Reversed specimen. C. Poorly behaved specimen. Remanence decays smoothly for specimens in A and B but increases with increasing AF for specimen in C.

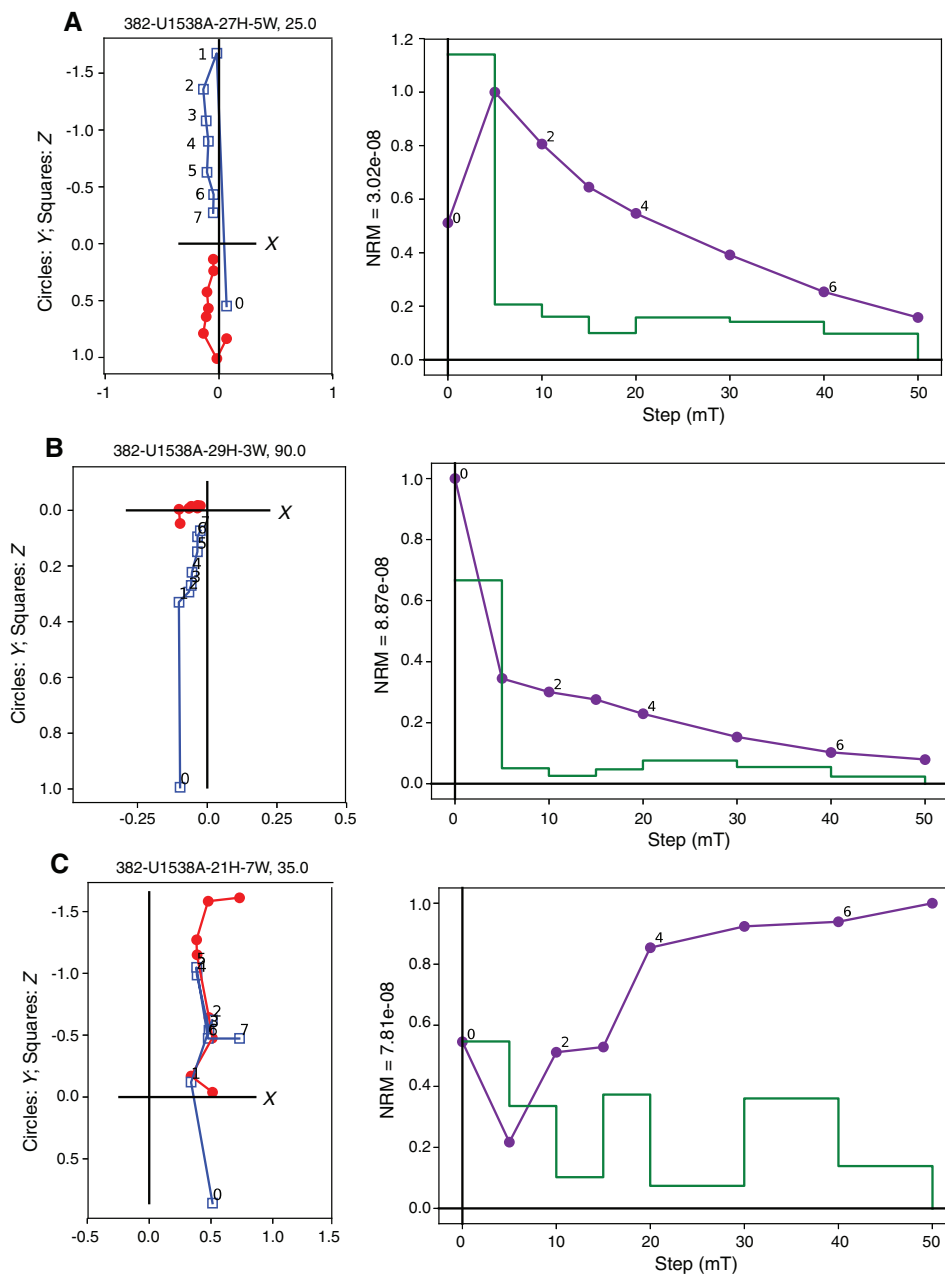


Figure F20. Magnetostratigraphic correlation, Hole U1538A. Archive-half data after 15 mT demagnetization step were grouped in 5 m bins and plotted as KDEs for upper part of hole (blue heat map); data for lower part of hole were not grouped (blue dots). Discrete sample data after 15 mT step: red stars = low CSDs, white squares = high CSDs, X = greater than unity remanence ratios (as discussed in text). Red lines = our ties to geomagnetic polarity timescale. Polarity: black = normal, white = reversed, gray = undetermined.

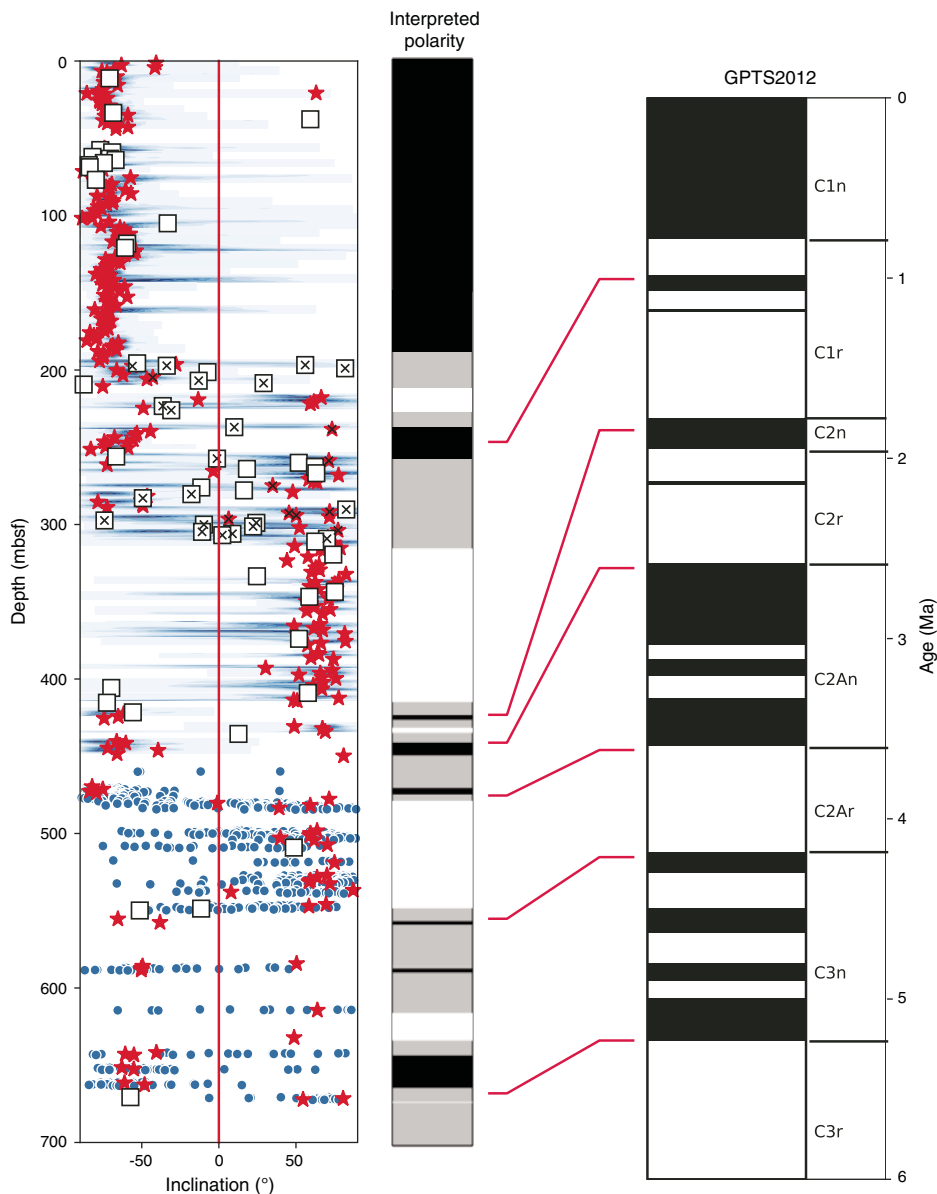


Table T18. Depth intervals of interpreted geomagnetic polarity, Hole U1538A. o = old, y = young. (Continued on next page.) [Download table in CSV format.](#)

Chron datum	Age (Ma)	Top core, section, interval (cm)	Top depth CSF-A (m)	Bottom core, section, interval (cm)	Bottom depth CSF-A (m)	Midpoint depth CSF-A (m)	Range (±) (m)
		382-U1538A-		382-U1538A-			
C1n (o)	0.781						
C1r.1n (y)	0.988	23H-1, 120	208.50	23H-2, 60	209.40	208.95	0.90
C1r.1n (o)	1.072	28H-1, 120	256.00	28H-3, 100	258.70	257.35	2.70
C1r.2n (y)	1.173						
C1r.2n (o)	1.19						
C2n (y)	1.778	47X-3, 16	414.17	48X-2, 61	422.71	418.44	8.54
C2n (o)	1.95	48X-4, 41	425.51	49X-1, 55	430.75	428.13	5.24
C2r.1n (y)	2.13						
C2r.1n (o)	2.15						
C2An.1n (y)	2.581	49X-4, 86	435.55	50X-1, 64	440.44	438.00	4.89

Table T18 (continued).

Chron datum	Age (Ma)	Top core, section, interval (cm)	Top depth CSF-A (m)	Bottom core, section, interval (cm)	Bottom depth CSF-A (m)	Midpoint depth CSF-A (m)	Range (±) (m)
C2An.1n (o)	3.03						
C2An.2n (y)	3.12						
C2An.2n (o)	3.21						
C2An.3n (y)	3.33						
C2An.3n (o)	3.596	53X-CC, 10	477.78	54X-3, 61	481.81	479.80	4.03
C3n.1n (y)	4.19	61X-2, 20	547.10	61X-4, 43	549.83	548.47	2.73
C3n.1n (o)	4.3						
C3n.2n (y)	4.49	65X-1, 63	584.23	65X-2, 81	585.91	585.07	1.68
C3n.2n (o)	4.63						
C3n.3n (y)	4.8	71X-1, 75	632.15	72X-1, 76	641.76	636.96	9.61
C3n.3n (o)	4.9	75X-1, 88	671.60	75X-2, 75	671.60	671.60	0.00
C3n.4n (y)	5						
C3n.4n (o)	5.24						
C3An.1n (y)	6.03						

Figure F21 Age-depth plot for data in Table T18, Site U1538. RAD = radiolarian, PMAG = paleomagnetism.

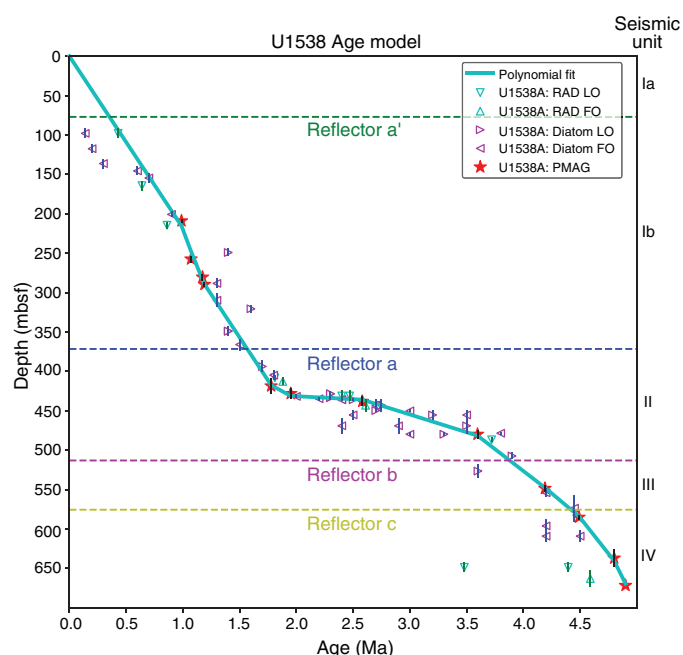


Figure F22. Methane concentrations, Hole U1538A.

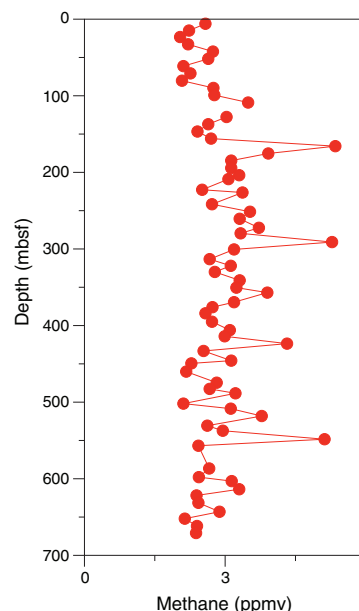


Table T19. Volatile hydrocarbon concentrations, Site U1538. [Download table in CSV format.](#)

Geochemistry

Volatile hydrocarbons

As part of the routine environmental protection and safety monitoring program, hydrocarbon concentrations in headspace gas were measured at a resolution of one sample per full-length core or one sample every other core for half-length cores throughout Hole U1538A. Methane concentrations are low throughout the core, ranging from 2.0 to 5.4 parts per million by volume (ppmv). Ethane (C₂H₆) concentrations are below the detection limit throughout the interval drilled (Figure F22; Table T19).

Interstitial water chemistry

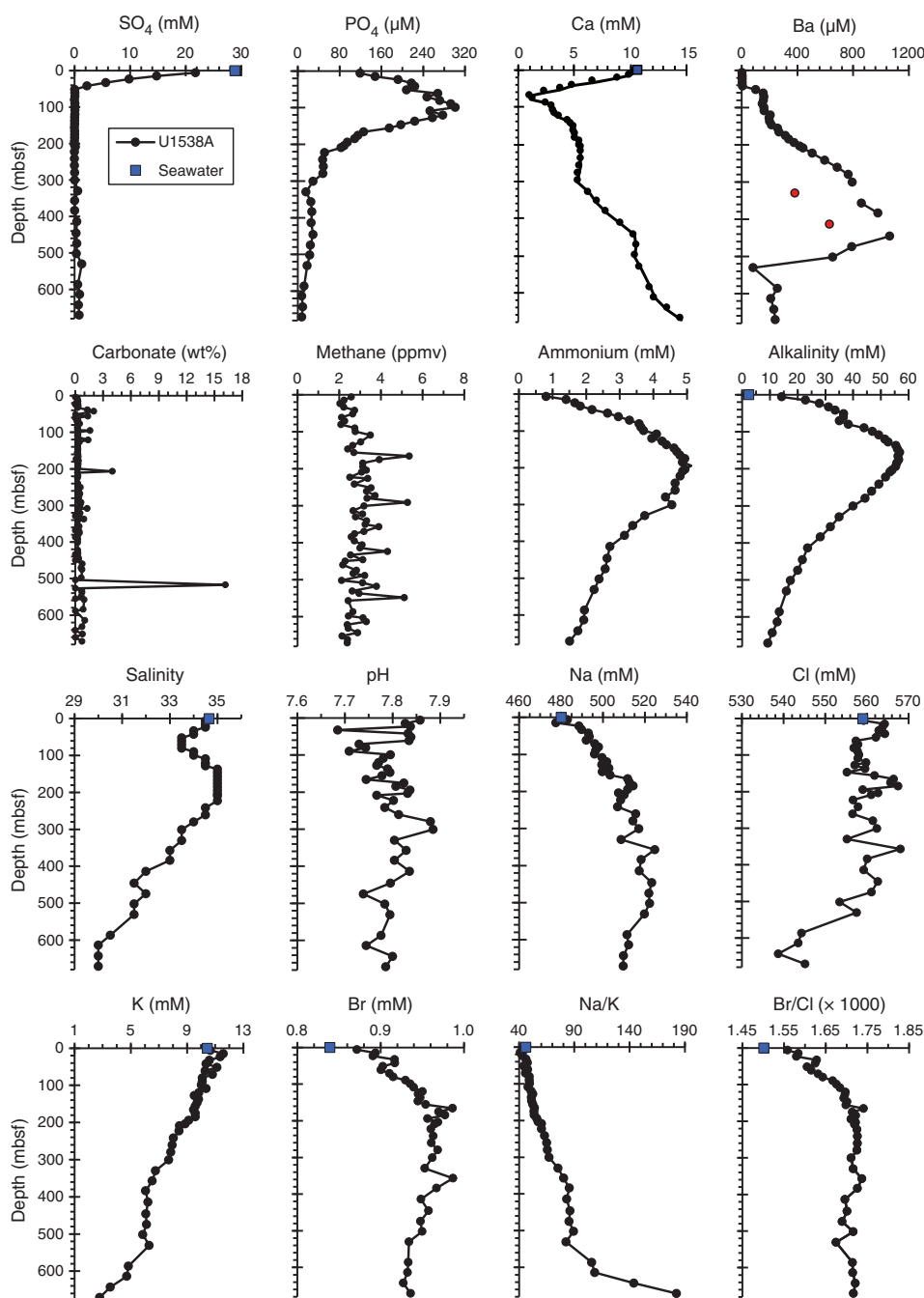
Shipboard chemical analysis of the IW from Site U1538 sediments followed the procedures detailed in [Geochemistry](#) in the Ex-

pedition 382 methods chapter (Weber et al., 2021a). Geochemical data were generated on 40 IW samples from Hole U1538A to 671 mbsf (Cores 382-U1538A-1H through 75X). The inorganic geochemical data at Site U1538 provide evidence for the presence of pronounced diagenetic processes—the most extreme enrichments in various IW parameters (see below) seen at any site during Expedition 382. Although recovered sediments are not methanogenic, sulfate is depleted below 52 mbsf. The main results from the shipboard analyses are presented in Figures F23, F24, and F25 and Tables T20 and T21.

Salinity, sulfate, alkalinity, ammonium, pH, phosphate, iron, and manganese

The reducing sedimentary conditions at Site U1538 result in clear-cut diagenetic profiles for the IW profiles of several species

Figure F23. IW properties (SO_4 , PO_4 , Ca, Ba, carbonate (from the solid), methane, ammonium, alkalinity, salinity, pH, Na, Cl, K, Br, Na/K, and Br/Cl), Site U1538. Blue squares = seawater concentrations or elemental ratios for reference (where applicable). Red dots = IW samples that experienced minor drilling fluid contamination during sampling (see Calcium, magnesium, silicon, barium, and other major and trace elements for discussion).

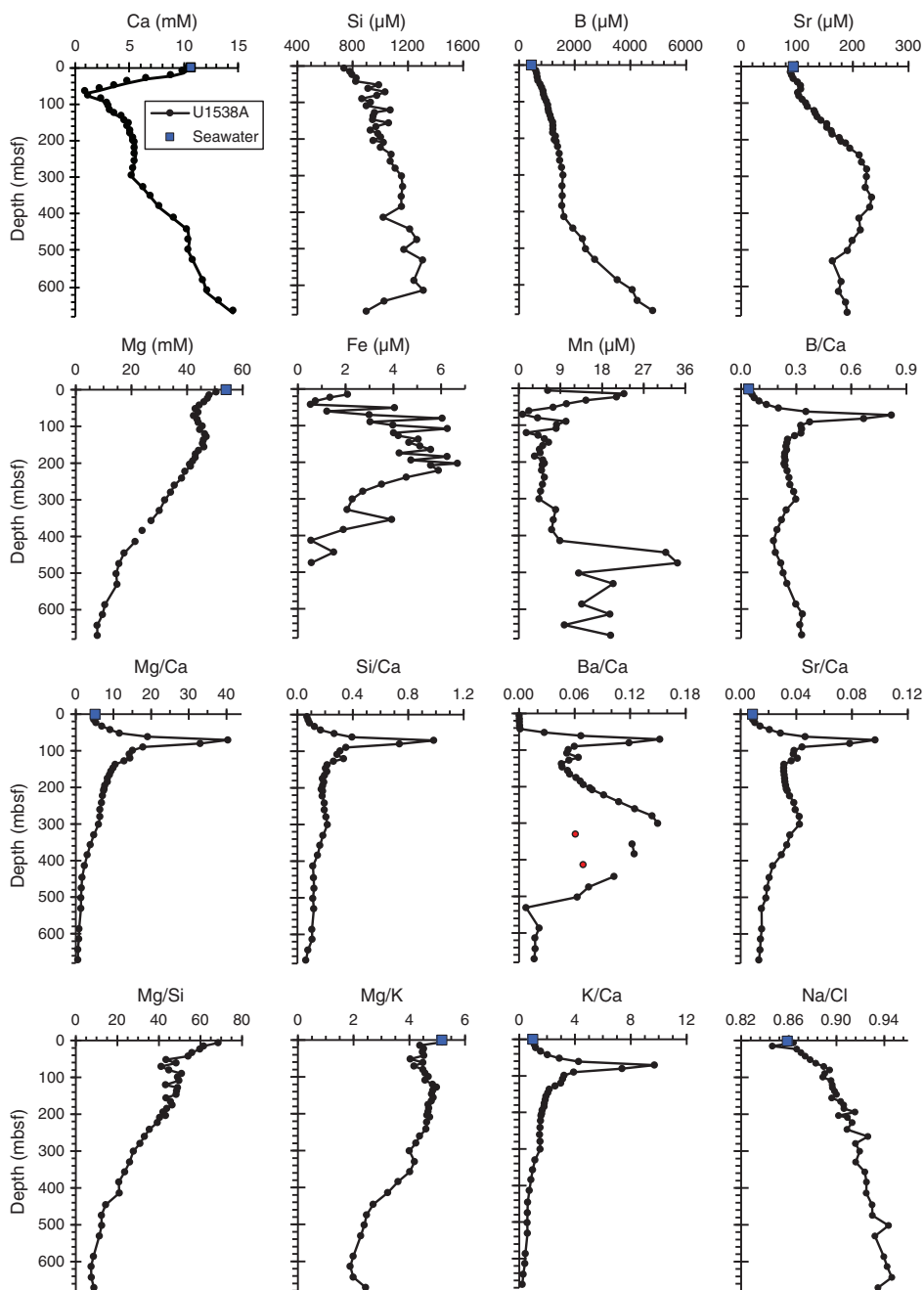


measured during shipboard analyses including alkalinity, Ca, Mn, Fe, PO_4 , ammonium, and Mn. Salinity decreases downcore in the sulfate reduction zone from surface salinity values within error of local seawater (i.e., 34.7 from the Global Ocean Data Analysis Project Version 2 [GLODAPv2]) (Olsen et al., 2016; Key et al., 2015) to 33.5. Salinity increases again to 35.0 between 146 and 222 mbsf and decreases below 222 mbsf to the lowest salinity values of 30.0 seen at 670 mbsf. Sulfate decreases from 22 mM at 6 mbsf to near zero at 52 mbsf. Minor dissolved sulfate concentrations were detected below 500 mbsf ($\text{SO}_4 < 1.5 \mu\text{M}$). The muted reappearance of dissolved

sulfate at depth is a feature seen at every Scotia Sea site (U1536–U1538). However, although dissolved sulfate is present at intermediate concentrations at the earlier sites, only traces of sulfate are observable at Site U1538.

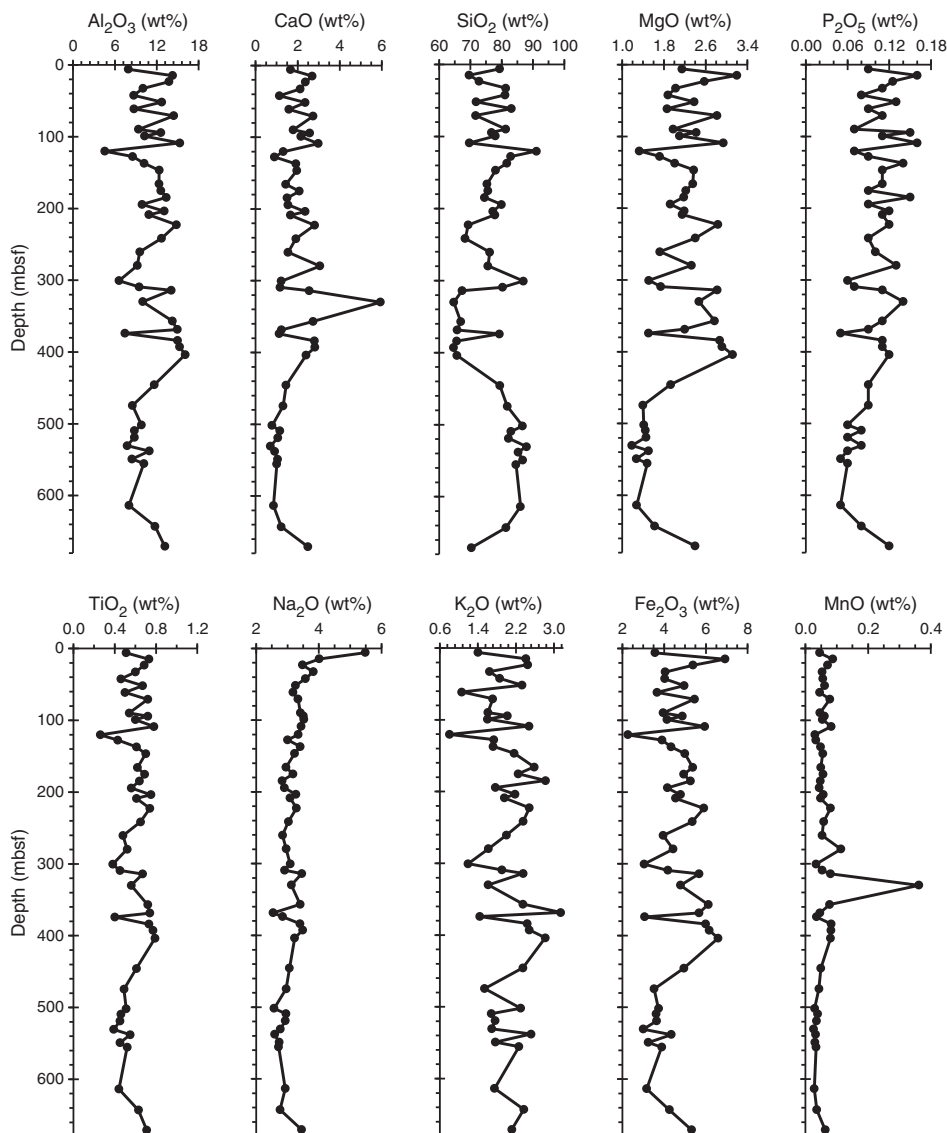
Alkalinity increases from 14 to 57 mM, ammonium increases from 0.8 to 5.2 mM, and phosphate increases from 119 to 301 μM with depth at Site U1538. As seen at the previous Scotia Sea sites, alkalinity levels are visually correlated with dissolved ammonium concentrations (Figure F23) and show a linear correlation with $R^2 = 0.83$.

Figure F24. IW properties (Ca, Si, B, Sr, Mg, Fe, Mn, B/Ca, Mg/Ca, Si/Ca, Ba/Ca, Sr/Ca, Mg/Si, Mg/K, K/Ca, and Na/Cl), Site U1538. Blue squares = seawater concentrations or elemental ratios for reference (where applicable). Red dots = IW samples inferred to have experienced minor drilling fluid contamination during sampling (see Calcium, magnesium, silicon, barium, and other major and trace elements for discussion).



Dissolved Mn enrichment is observable in the uppermost 32 m at Site U1538, followed by Fe enrichment below 32 mbsf, suggesting Mn-Fe oxide mobilization in the upper 260 mbsf. Fe concentrations in the sulfate reduction zone average ~1.2 µM and increase to 6.7 µM between 52 and 260 mbsf. The presence of detectable dissolved Mn concentrations seen at every depth at Site U1538 suggests that burial rates of iron and manganese oxides exceed those of microbial reduction of these metals because depletion of Mn oxides would also result in dissolved Mn concentrations below the detection

limit. In turn, relatively elevated dissolved Mn levels as high as 22.7 µM in the sulfate reduction zone suggest partial Mn oxide dissolution at shallow depths. The dissolved Fe enrichment seen between 50 and 220 mbsf at Site U1538 was not observed at the other Scotia Sea sites. Note that the reported dissolved Fe concentrations are qualitative reflections of in situ IW levels and need to be interpreted with caution because squeezed sediment samples for IW analysis were not extracted from bulk sediments under oxygen-free conditions.

Figure F25. Bulk sediment major element compositions (Al_2O_3 , CaO, SiO_2 , MgO, P_2O_5 , TiO_2 , Na_2O , K_2O , Fe_2O_3 , and MnO), Site U1538.Table T20. Interstitial water geochemical data, Site U1538. [Download table in CSV format.](#)Table T21. Inductively coupled plasma–atomic emission spectroscopy sediment data, Site U1538. [Download table in CSV format.](#)

Calcium, magnesium, silicon, barium, and other major and trace elements

Significant organic matter degradation is apparent in the upper 120 m, as evidenced by elevated phosphate concentrations and a pronounced Br/Cl gradient (Figure F23) (Berg and Solomon, 2016). High Ba concentration due to barite dissolution is evident at depths without resolvable sulfate between 60 and 445 mbsf; the highest dissolved barium concentrations of any Expedition 382 sites were observed here. The spatial evolution of the Ba enrichment with depth differs from the previous sites in that Ba concentrations increase over a more than 300 m interval and turn to a decreasing trend in the interval between 445 and 530 mbsf. Two IW samples (red in Figure F23) suggest suspiciously low dissolved Ba concentrations at

these two depths. Duplicates were generated for these samples, and the results were confirmed. We conclude that the reduced Ba concentrations at these two depths are most likely caused by traces of drilling fluid contamination on the order of 1% providing dissolved sulfate to the IW that led to barite precipitation after IW extraction in the laboratory. Note that this possible drilling fluid contribution did not affect the other parameters presented in Figures F23 and F24.

Calcium concentrations decrease significantly from 11.7 to 1.9 mM in the sulfate reduction zone, recover to stable intermediate concentrations throughout the upper half of Site U1538 between 146 and 300 mbsf, and become enriched deeper in sedimentary IW, reaching concentrations as high as 14.5 mM at 671 mbsf. The Ca depletion above the sulfate depletion depth was seen at every site during Expedition 382 and reflects authigenic carbonate fluorapatite formation. Significantly increased dissolved B concentrations are observable below 440 mbsf. Chloride concentrations generally decrease with depth below 474 mbsf, as does IW salinity, whereas sodium concentrations increase from the top of the core to 445

mbsf, leveling off toward slightly lower concentrations in the deepest core section. Authigenic clay formation may be indicated by the pattern of decreasing potassium and magnesium concentrations in the deeper parts of Site U1538.

Bulk sediment geochemistry

Total carbon (TC), total nitrogen (TN), and inorganic carbon were measured in Hole U1538 as the shipboard solid-phase analysis (Table T22; Figure F26). Total organic carbon (TOC) concentrations vary from 0 to 3.8 wt%, whereas TN contents range from 0.025 to 0.225 wt%. Calcium carbonate (CaCO_3) concentrations fluctuate between 0.02 and 16.2 wt%, and values in the vast majority of samples are below 2 wt%. TOC/TN ratios are lower than 10, suggesting a marine origin of sedimentary organic matter, except for one sample at 504 mbsf that has a significantly elevated value of 152, which suggests the presence of terrestrial organic matter.

Inorganic bulk sediment geochemistry

Overall, inorganic bulk geochemical profiles generated for Site U1538 are remarkably invariant for the entire sampled interval, displaying no clearly resolvable long-term changes as a function of depositional age. At a smaller scale (within tens of meters), the record appears noisier, likely reflecting glacial–interglacial variation in sediment delivery. A wide range of parameters were measured, and a selection of key elements and ratios are displayed in Figures F25 and F27. The full suite of results is presented in Table T21. The low Ca concentrations confirm the lack of significant carbonate at the site, whereas Si contents are very high throughout. To what extent the very high bulk Si contents in sediments from Site U1538 are controlled by biogenic or lithogenic in origin (as high as 91 wt% Si at 120 mbsf; Figure F25) needs a more in-depth inspection (see **Lithostratigraphy**). Although bulk sediment sampling was usually paired with IW sampling, the spacing is rather random, not tracing particular glacial or interglacial intervals. This needs to be considered when interpreting the geochemical profiles.

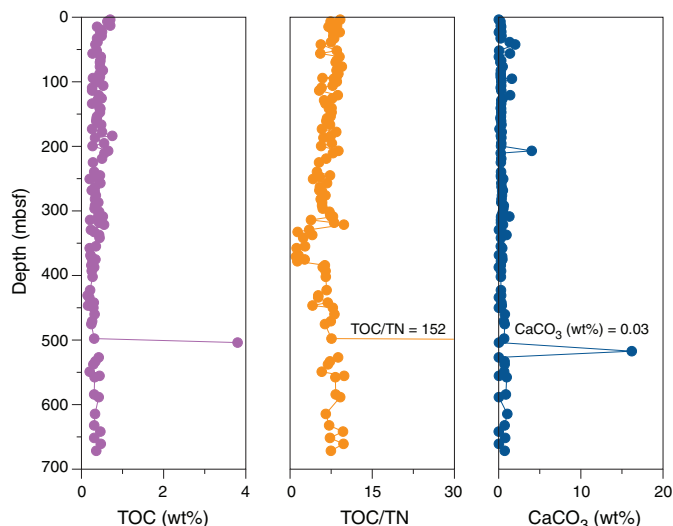
Ba/Ca in the bulk sediment shows no resemblance to IW dissolved Ba/Ca (Figures F23, F27). This lack of correspondence between bulk and IW values was also observed for K and Mg/Si. Overall, we attribute the lack of covariance between dissolved phase and bulk sediment composition to mass balance constraints because the respective element concentrations dissolved in IW are extremely dilute relative to concentrations in the particulate phase.

Rhizon interstitial water samples

A total of 25 Rhizon IW samples were taken from Sections 382-U1538B-1H-1 through 1H-6 (0–8.5 mbsf) following the IW sampling guidelines (see **Geochemistry** in the Expedition 382 methods chapter [Weber et al., 2021a]). The samples were collected at a 20 cm resolution for the upper 3 m and a 50 cm resolution from 3 to 8.5 mbsf. Shore-based analyses of $\delta^{18}\text{O}$, δD , $\delta^{13}\text{C}_{\text{DIC}}$, Li isotopes ($\delta^7\text{Li}$), Mg isotopes ($\delta^{26}\text{Mg}$), and K isotopes ($\delta^{41}\text{K}$) (~1 mL) using multicollector inductively coupled plasma–mass spectrometry will be carried out at the Korea Basic Science Institute for all collected samples.

Table T22. TOC, CaCO_3 , TN, and TOC/TN ratio, Site U1538. [Download table in CSV format.](#)

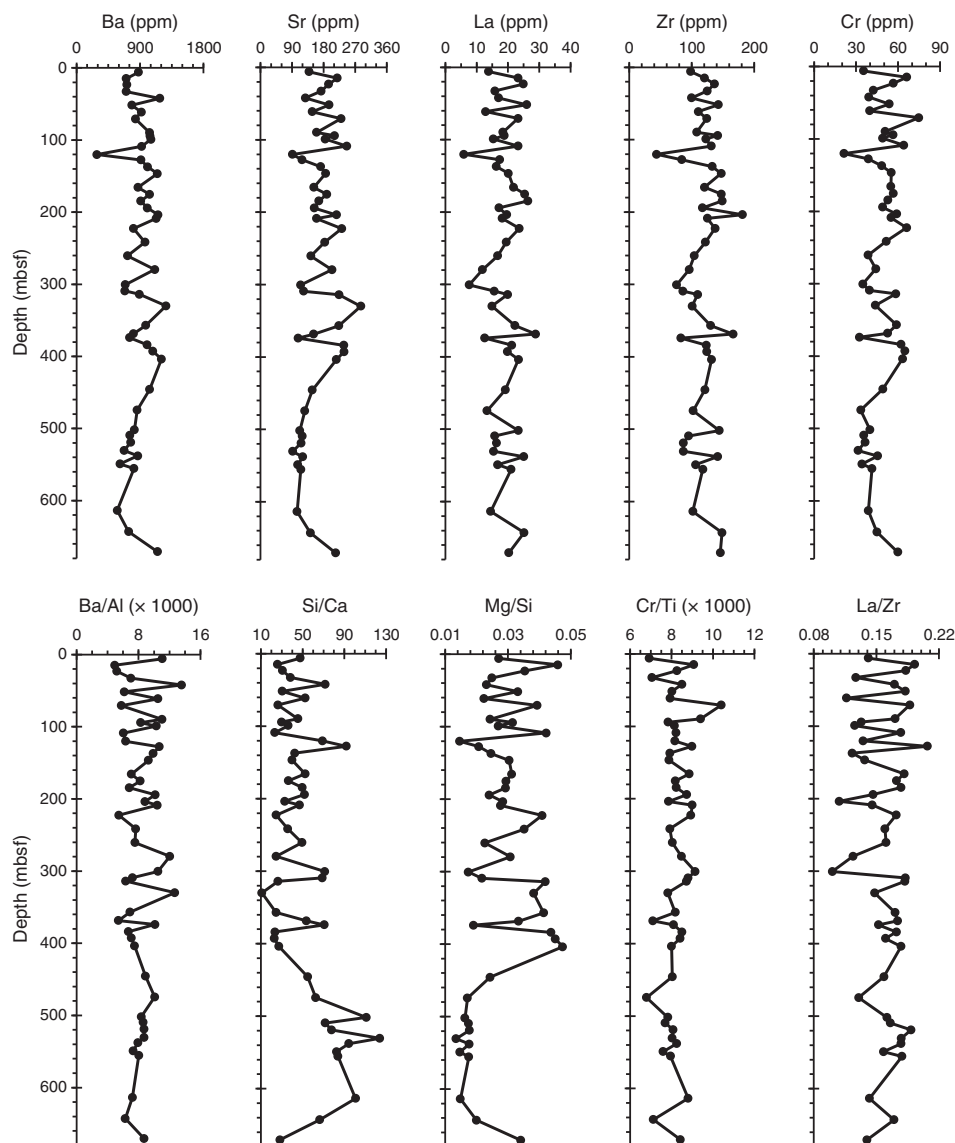
Figure F26. Bulk sediment TOC, TOC/TN ratio, and CaCO_3 , Site U1538.



Summary

Samples from Hole U1538A were analyzed for headspace gas, IW chemistry, and bulk sediment geochemistry. In Hole U1538A, methane is the dominant hydrocarbon present in low concentrations (2.0–5.4 ppmv) throughout. Ethane, propane, and higher molecular weight hydrocarbons concentrations are below the detection limit throughout the interval drilled. IW geochemical data were generated for 40 samples from Hole U1538A to 670.75 mbsf (Cores 382-U1538A-1H through 75X). The inorganic geochemical IW data at Site U1538 suggest that originally deposited or authigenically formed sedimentary phases are undergoing enhanced redox-controlled diagenetic alteration processes. Although the core is not methanogenic, sulfate is depleted below 60 mbsf. Bulk sediment TOC and TN contents are generally low, varying from 0.02 to 0.8 wt% and from 0.04 to 0.23 wt%, respectively. Inorganic bulk sediment analyses were carried out on 48 samples for an assessment of the sedimentary geochemical properties. Shorter timescale variations in geochemical compositions are observable, leading to a somewhat noisy appearance of the bulk sedimentary records at Site U1538. The noisy appearance of elemental concentrations and ratios is most likely the expression of provenance and process changes on glacial–interglacial timescales, and these geochemical trends appear less noisy in the lower part of the core where climate cycles are less pronounced. Major and trace elemental compositions found throughout the core are dominantly terrigenous except for the high silica concentrations that are most likely biosilica, and in almost all sampled depths the sediment is carbonate free. The lower part of the sedimentary record (below 380 mbsf) is geochemically more homogeneous than the upper part.

Figure F27. Selected sediment trace element compositions and elemental ratios, Site U1538. La is a rare earth element, and Zr is a high field strength element. Note that elemental ratios shown here are weight ratios.



Physical properties

High-resolution physical property measurements were made on all cores and most core catchers from Holes U1538A–U1538D to provide basic information on sediment composition and variability. The Whole-Round Multisensor Logger (WRMSL) measured gamma ray attenuation (GRA) bulk density, MS, and compressional wave velocity on the *P*-wave logger (PWL) at 1 cm intervals for Cores 382-U1538A-1H through 35F and at 2 cm intervals for the remaining cores. The PWL was used for all APC and HLAPC cores (Hole U1538A through Core 35F and Holes U1538B–U1538D) but not for cores retrieved with the XCB system (from Core 382-U1538A-36X downhole). Material recovered with the XCB system has a slightly smaller core diameter and does not fill the liner entirely. Hence, proper contact between the caliper and the sediment does not occur, which leads to erroneous measurements. On whole-round cores, we also measured natural gamma radiation (NGR; at

10 cm increments). Once the cores were split, the section halves were X-rayed and thermal conductivity measurements (2–4 per core) were made for all holes. *P*-wave velocity was acquired using the *P*-wave caliper (PWC) in at least three sections per APC and HLAPC core and in every section (if possible) for XCB cores to partially compensate for the lacking PWL measurements. For archive halves, point magnetic susceptibility (MSP) and color reflectance were measured at 1 cm increments for Cores 382-U1538A-1H through 35F and at 2 cm increments for the remaining cores using the Section Half Multisensor Logger (SHMSL) and digital color imaging (e.g., the Section Half Imaging Logger [SHIL]). Additionally, we took discrete samples from Hole U1538A for moisture and density (MAD) measurements (1–3 samples per core). Ideally, these samples represented the various lithologies, and they were used to determine water content, wet bulk density, dry bulk density, porosity, and grain density.

Whole-Round Multisensor Logger measurements

Results from WRMSL measurements for Holes U1538A, U1538C, and U1538D are compiled in Figures F28, F29, and F30, respectively. We measured high-resolution data (1 cm intervals) for all APC and HLAPC cores and the majority of the core catchers. At this site, nearly all cores rested for about 4 h before measurement to adjust to room temperature (~20°). Only the top sections of Holes U1538B and U1538C were measured as soon as they arrived in the laboratory for stratigraphic correlation purposes. These sections were later measured a second time when they were at room temperature.

Gamma ray attenuation bulk density

Wet bulk density values range from 1.3 to 1.9 g/cm³ and have a mean value of 1.5 g/cm³. Cyclic variability is observed downhole for GRA bulk density together with a general trend of increasing values in the upper 280 mbsf. Bulk density decreases to slightly lower values between 280 and 360 mbsf, is elevated between 360 and 450 mbsf, is relatively low between 450 and 600 mbsf, and reaches the highest values in Cores 382-U1538A-45X through 50X (390–450 mbsf). The lowest wet bulk density values are found in Cores 8H–13H (~65–120 mbsf) and 37X–43X (320–370 mbsf) (Figures F28, F29, F30). The observed cyclicity is highly correlated between

Holes U1538A, U1538C, and U1538D. A weak positive covariation is found for the relation of density and NGR counts and for density and MS (Figure F31). GRA bulk density values agree with calculated density values from the MAD discrete samples and hence confirm the high data quality.

Magnetic susceptibility

MS is sensitive to the concentration and type of magnetic minerals present in the sediments. Although usually appearing as sharp peaks of high-amplitude variability, MS also follows the lithologic changes that are inferred to represent glacial–interglacial cycles, with high MS associated with glacial silty clay intervals and lower MS associated with interglacial diatom ooze intervals. Values range from 0 to 180 × 10⁻⁵ SI. The baseline of the signal is relatively constant downhole through Core 382-U1538A-43X and then higher amplitude variability and an increase in the minimum values in MS is observed through Core 50X. This change also agrees with a major lithologic change from more diatom ooze to silty clay–dominant facies. High-amplitude variation in MS is observed in Cores 6H and 37X–50X (amplitude = 180 × 10⁻⁵ SI).

The highest MS values are found in Cores 382-U1538A-42X through 50X and 62X–71X (>25 × 10⁻⁵ SI), and the lowest values (<5 × 10⁻⁵ SI) are observed in Cores 6H–9H. Generally, we observe a positive correlation in the variability with depth for all physical

Figure F28. Physical property data, Hole U1538A. MS: red = WRMSL, gray = SHMSL (MSP). P-wave velocity: dots = WRMSL, squares = PWC. Wet bulk density: line = WRMSL, dots = discrete. cps = counts per second.

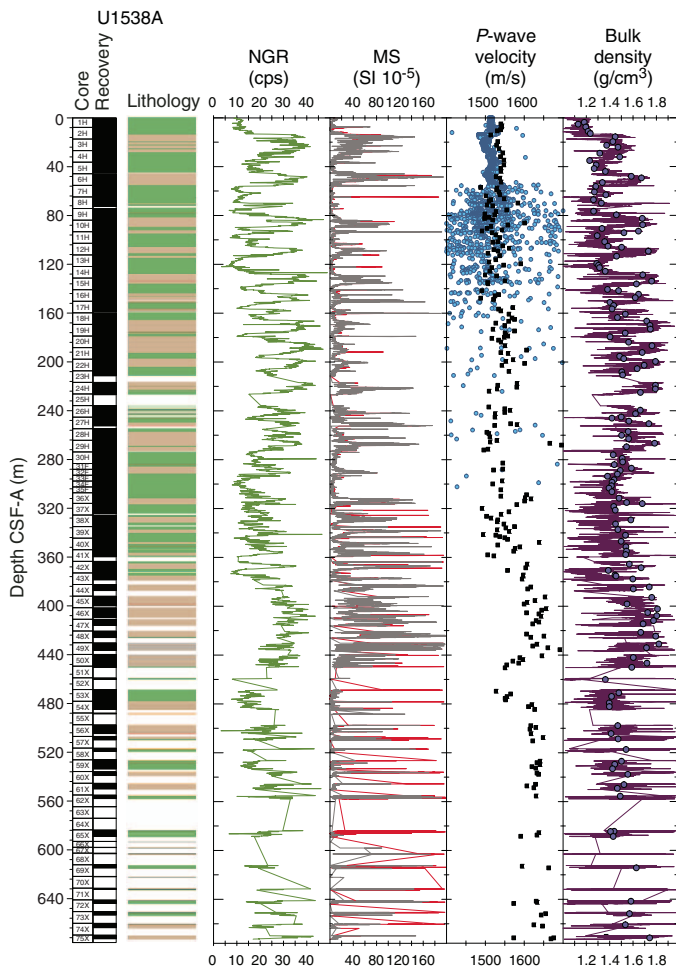
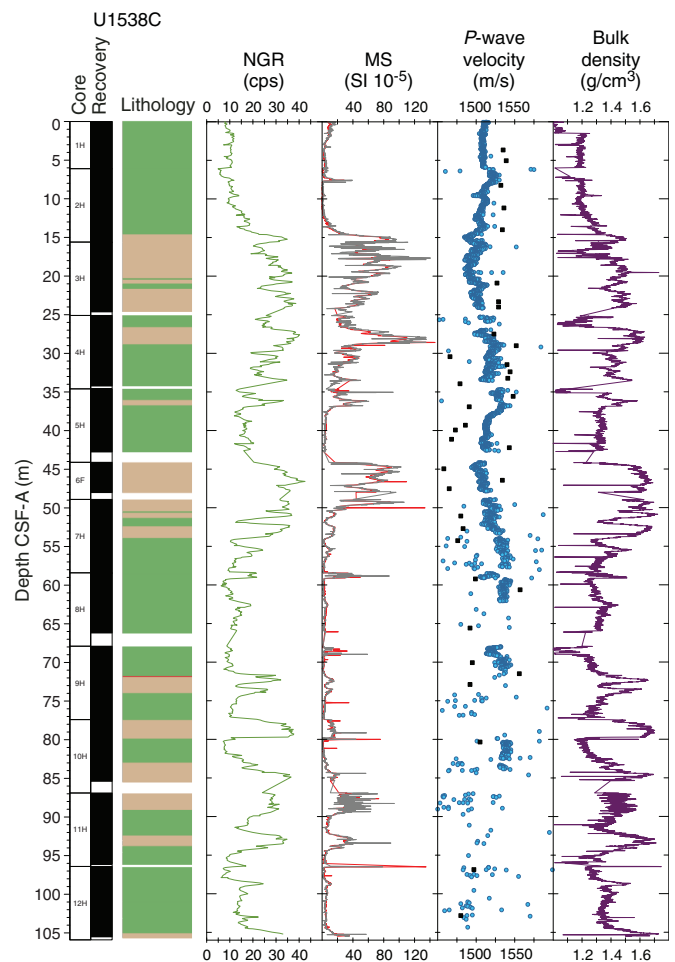


Figure F29. Physical property data, Hole U1538C. MS: red = WRMSL, gray = SHMSL (MSP). P-wave velocity: dots = WRMSL, squares = PWC.



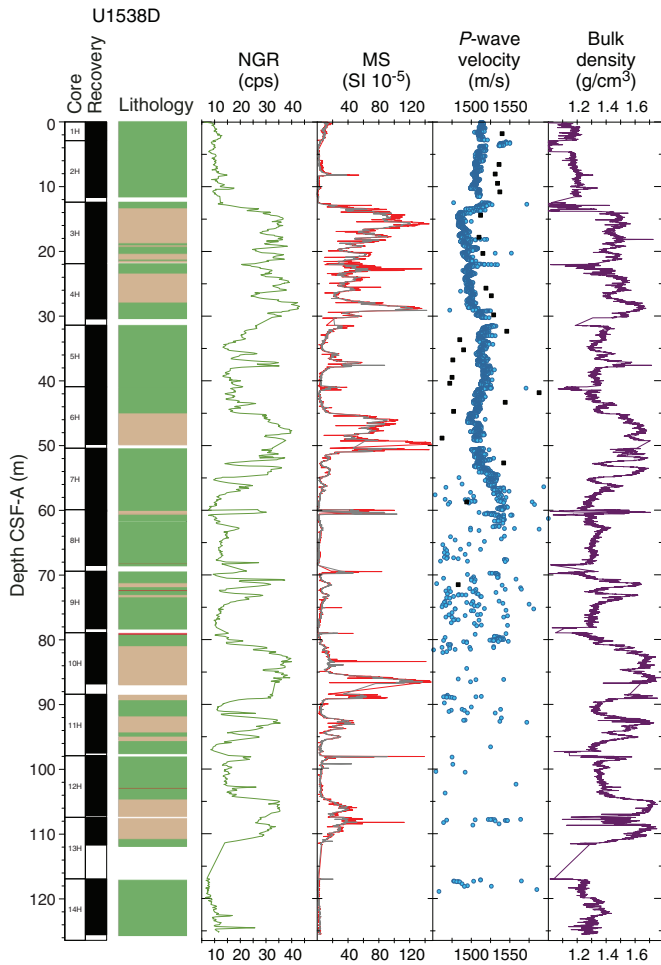
properties determined using the WRMSL. In addition, a weak positive correlation is found between MS and NGR in any given depth interval, and another is found between NGR and GRA (Figure F31).

P-wave velocity

P-wave velocity values measured with the PWL are erroneous if cracks or poor contact with the liner wall occur. The PWL was ac-

tive while measuring cores retrieved with the APC and HLAPC systems. The measurements were generally good through Core 382-U1538A-6H and range from 1470 to 1550 m/s. Deeper cores exhibited numerous cracks due to decompression, and the PWL values were characterized by spikes and large scatter (Figure F28). The lowest velocity values were found in Cores 3H and 6H (20 and 50 mbsf, respectively), and the highest values were in Core 2H (>10 mbsf). Below Core 382-U1538A-6H, realistic P-wave velocity values were only obtained by PWC measurements.

Figure F30. Physical property data, Hole U1538D. MS: red = WRMSL, gray = SHMSL (MSP). P-wave velocity: dots = WRMSL, squares = PWC.



Natural gamma radiation

Cyclic changes in NGR are observed throughout the cored site. Generally elevated NGR values are observed at 370–450 mbsf (>40 counts/s). NGR values display significant variations, and the lowest NGR counts are in Cores 382-U1538A-6H through 13H (~5–10 counts/s). High-amplitude variability is observed throughout the sediment column (e.g., in Core U1538A-10H; 10–37 counts/s), specifically for the upper 235 mbsf (Figures F28, F29, F30). Cyclic variation in NGR follows lithologic cycles, with high NGR associated with silty clay and low NGR associated with diatom ooze.

Thermal conductivity

Thermal conductivity was measured at a higher resolution in all holes at Site U1538 compared with previous sites and varies between 0.8 and 1.35 W/(m·K) (Figure F32). An overall positive secular trend with depth occurs through Core 382-U1538A-48X (~415 mbsf), whereas scattered values are observed below that depth to the bottom of the hole. The average observed thermal conductivity is 1.05 W/(m·K). The overall lowest values were measured in Cores 9H–13H (75–120 mbsf) where the highest variety of lithologies were found. The highest thermal conductivity values are observed in Cores 71X and 75X. Thermal conductivity measurements were combined with the borehole temperatures to provide heat flow estimates (see Downhole measurements).

Point magnetic susceptibility

MSP measurements were performed on archive halves. Results agree with the WRMSL MS data (Figures F28, F29, F30). MSP measurements were mostly acquired at 1 cm spacing through Core 382-U1538A-35F and at 2 cm spacing for the remaining cores taken in this hole. In some cases, higher variability is observed with this instrument because of the smaller integration volume of the sensor (~1 cm depth resolution; 1σ) compared with the loop sensor (~18 cm depth resolution; 1σ) used on the WRMSL (Weber et al., 1997).

Figure F31. Crossplots and linear relationships of NGR, GRA, and MS, Holes U1538A, U1538C, and U1538D.

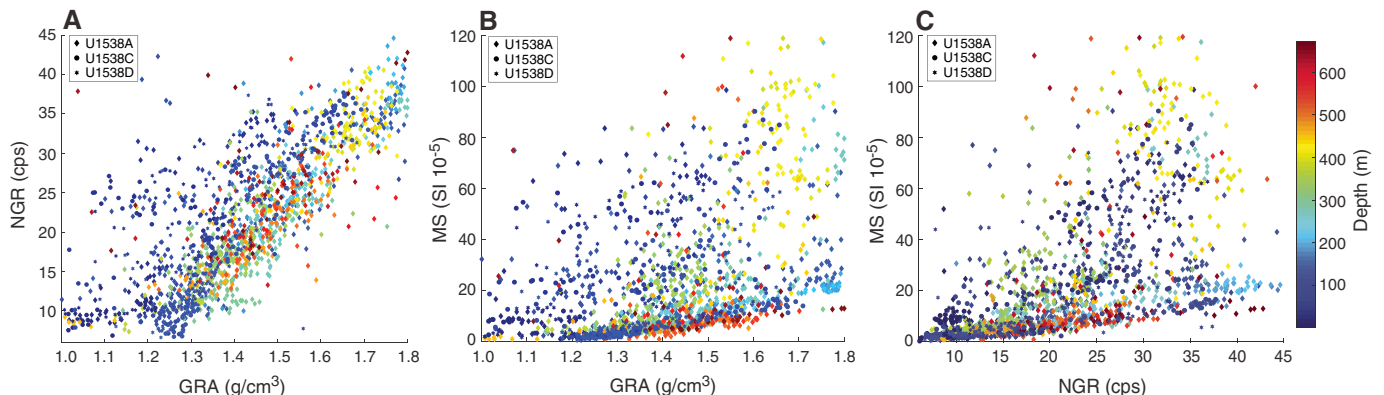
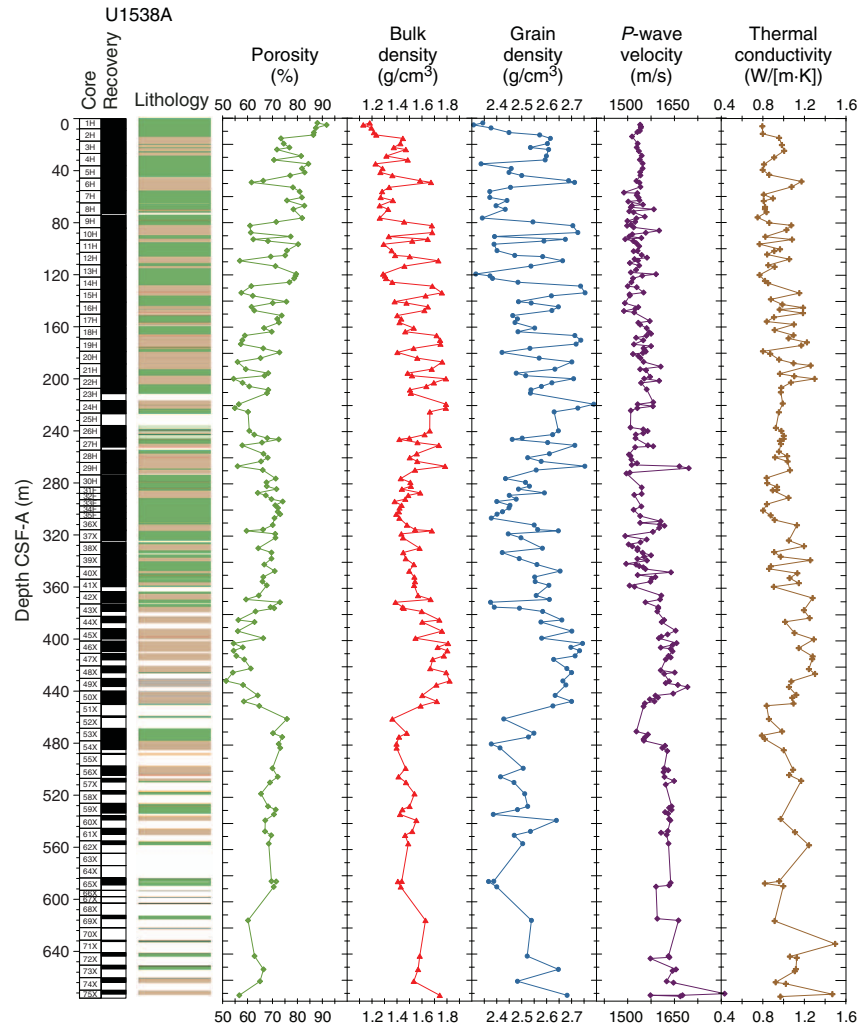


Figure F32. MAD results, Hole U1538A. *P*-wave velocity = caliper velocity measurements with automatic and manually picked first arrival times.

Discrete compressional wave velocity

Discrete *P*-wave measurements were made using the PWC (see [Physical properties](#) in the Expedition 382 methods chapter [Weber et al., 2021a]) on cores taken from Holes U1538A–U1538D. Two to three samples per APC core were measured for *P*-wave velocity using the PWC to provide a correlation for PWL values measured on the whole-round cores. Below Core 382-U1538A-9H (75 mbsf), the PWC sampling resolution increased to ~3–5 samples per APC and XCB core in an attempt to constrain the *P*-wave values downhole because the PWL system was not providing realistic measurements because of internal cracks in the sediment cores and the smaller diameter of the XCB cores farther downcore. An automated algorithm determined PWC values unless a weak signal or poor coupling required the instrument operator to manually determine a PWC value. Manually derived velocity values frequently needed to be collected between ~57 and 370 mbsf in Hole U1538A and in Holes U1538C and U1538D at equivalent depths (below ~57 mbsf).

Downhole PWC measurements from Holes U1538A, U1538C, and U1538D are not consistent with WRMSL PWL values (Figures [F28](#), [F29](#), [F30](#)). Holes U1538B and U1538D demonstrate relatively good agreement between PWL and PWC measurements. Where a visible trend in *P*-wave values from the PWL system occurs in Hole

U1538A, *P*-wave values measured using the PWC are ~10–30 m/s higher than those from the PWL. In Hole U1538C, no consistent offset occurs between PWL and PWC measurements because of relatively high variability observed in the PWC data. Site U1538 *P*-wave values measured using the PWC system are consistent across the same stratigraphic interval in Holes U1538A–U1538D (0–100 mbsf). An overall increase in *P*-wave velocity occurs throughout the Site U1538 stratigraphic sequence, with values ranging from ~1500 to 1800 m/s. Changes in *P*-wave velocity are consistent with changes in the dominant lithology, which include transitions from siliceous mud and ooze to diatomite and more consolidated gravel-bearing mud.

Moisture and density

Bulk density measurements were taken for Hole U1538A, and values were calculated from moisture and volume measurements made on discrete samples taken from the working halves of split cores (see [Physical properties](#) in the Expedition 382 methods chapter [Weber et al., 2021a]). The sample resolution in each core varied depending on lithology, recovery, and quality, and at least three samples per APC core, at least two samples per HLAPC, and two to three samples per XCB core were taken. A total of 153 samples were taken for MAD estimates from Hole U1538A.

MAD density values correspond very well to GRA bulk density values measured on the WRMSL (Figure F28). Hole U1538A bulk density values range from ~ 1.1 to ~ 1.8 g/cm³ and demonstrate an overall downhole increase over the upper ~ 430 m. Bulk density values increase from ~ 1.1 g/cm³ at the top of the hole to ~ 1.8 g/cm³ at ~ 220 mbsf and fluctuate by 0.3 – 0.5 g/cm³ every ~ 10 to ~ 20 mbsf through this section. From ~ 220 to ~ 300 mbsf, bulk density values decrease to ~ 1.4 g/cm³. They increase to ~ 1.8 g/cm³ between ~ 300 and ~ 430 mbsf, which is consistent with a change in lithology from less consolidated diatom ooze/silty clay to a more consolidated diatomite. The signal amplitude observed between ~ 300 and ~ 430 mbsf demonstrates relatively little variability compared to the signal shallower than ~ 300 mbsf. A decrease in bulk density to ~ 1.4 g/cm³ occurs between ~ 430 and ~ 460 mbsf before values increase steadily to ~ 1.7 g/cm³ from ~ 460 mbsf to the bottom of the hole. Changes in observed trends below 300 mbsf correlate well with lithologic transitions from siliceous-bearing ooze and mud to lithologies dominated by consolidated clays, muds, and gravelly breccias.

The overall downhole increase in Hole U1538A grain density follows the trend observed in the bulk density values (Figure F32). Hole U1538A grain density values range from ~ 2.3 to 2.8 g/cm³. As with bulk density, Hole U1538A grain density demonstrates a higher signal amplitude between the top of the hole and ~ 300 mbsf, and grain density fluctuates by ~ 0.2 – 0.5 g/cm³ every ~ 10 mbsf. The overall downhole trends of bulk and grain density are similar, and the grain density trend observed between ~ 460 mbsf and the bottom of the hole scatters around lower mean densities than those seen in the interval above.

Porosity (percent of pore space of the wet sediment volume) is included in the suite of MAD measurements and indicates a general decrease in volume percent (Figure F32). Discrete porosity values range from $\sim 90\%$ to $\sim 50\%$ throughout Hole U1538A. Relatively high porosity values at the top of the sequence are consistent with the presence of biosilica-rich muds and clays; conversely, a decrease in porosity correlates well with the presence of more consolidated sediments. The sudden increase in porosity between 450 and 460 mbsf reflects a change in lithology from silty clay to diatomite.

Color reflectance

$L^*a^*b^*$ color reflectance measurements describe coordinates in a spherical system with 16.8 million possible variations (Weber, 1998; Blum, 1997). The L^* axis measures the black–white color component and is known as the lightness or gray value. It is a reliable tracer for the content of biogenic carbonate in marine sediment (Weber, 1998). A very subtle decrease in L^* values for Holes U1538A, U1538C, and U1538D is observed downhole (Figures F33, F34, F35).

The a^* axis is the green–red component and is usually a tracer of changing redox conditions in the sediments. For Holes U1538A, U1538C, and U1538D, a^* values are low yet very noisy, presenting little amplitude variation along the entire hole.

The b^* axis is the yellow–blue component, and it is a proxy for the relative opal content in cores from the Scotia Sea (Sprenk et al., 2013). More positive values (more yellow) correspond to higher opal (usually diatoms) contents. A decreasing downhole trend is observed for this component, which reaches constant values in Core 382-U1538A-44X. The highest values are found in Cores 1H and 13H. Both a^* and b^* measurements show a cyclical variation downhole.

Physical properties and relationship with facies

In general, Site U1538 sediments are composed of greenish gray diatom-bearing/rich silty clay and greenish gray clay-bearing diatom ooze. Although carbonate and TOC contents are generally low, a number of intervals contain significant quantities of foraminifers (see Lithostratigraphy). The silty clays are typically associated with higher MS, NGR, and density and lower P -wave velocity and b^* sediment color. Glauconite is present, and variations in its abundance likely play a strong role in controlling changes in sediment color and lightness.

The stratigraphy at Site U1538 is divided into two units. Lithostratigraphic Unit I (middle and late Pleistocene) spans the uppermost ~ 300 m and consists of interbedded silty clay and diatom ooze with highly variable MS, NGR, density, P -wave velocity, and b^* color. Lithostratigraphic Unit II (Pliocene–early Pleistocene) spans ~ 300 – 676 mbsf, consists largely of diatom-bearing/rich silty clay with abundant ice-rafted lithic grains concentrated in layers, and is associated with overall higher but equally variable MS, NGR, and GRA and lower b^* color. In addition to the abundant in situ coarse sand and pebbles in the cores, abundant pebbles with a variety of lithologies are concentrated near the tops of the cores by washing down during the coring process.

It is most likely that changes in the physical properties of these units are a product of variations in the proportion of their biogenic particles (dominantly diatom opal) and terrigenous clastic content. In the case of MS, variations in these data are controlled by dilution of the terrigenous magnetic carrier by diamagnetic biogenic opal. This signal is further modulated by a diagenetic overprint below ~ 50 mbsf (see Paleomagnetism).

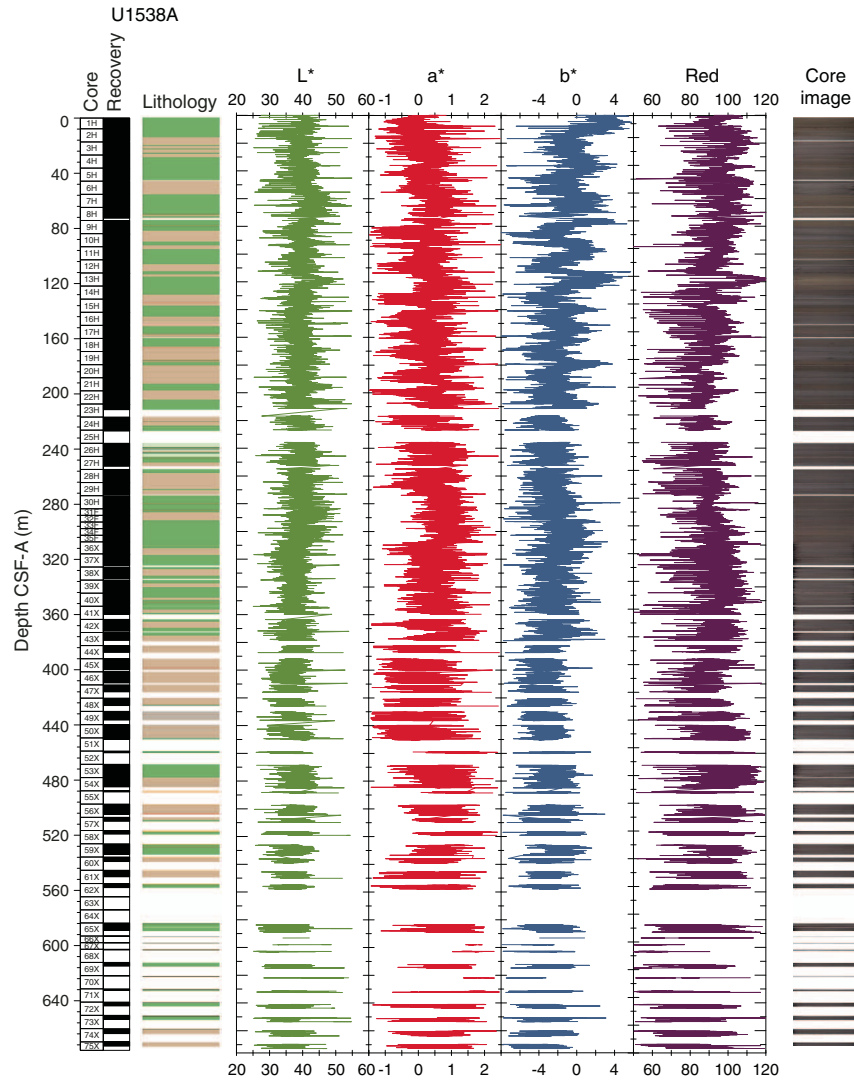
Core disturbances and data quality

All physical property measurements were possible for all cores, but the PWL was not used for XCB cores in Hole U1538A. Hole U1538A was a good hole in terms of the number of cores used for affine ties in the stratigraphic correlation. A lot of the first and second sections of cores recovered at Site U1538 in all holes were negatively affected by weather conditions during coring because of the high heave. In these sections, physical property data were not realistic or indicative of the formation properties. Core disturbances such as uparching of layers did not diminish the quality of the physical property data in a way that prevents meaningful core-seismic integration in the splice, but a few flow-in cases do.

Summary

Physical property data were acquired on all cores from Site U1538 using the WRMSL for GRA wet bulk density, volume-specific MS, and P -wave velocity (PWL). We also measured NGR in all sections longer than 50 cm. Once the whole rounds were split in two halves, we acquired X-ray images of all the archive halves and measured thermal conductivity in at least three sections per core. The SHMSL was then used to measure MSP and color reflectance using the $L^*a^*b^*$ color system, and the red-green-blue (RGB) color of the sediments was measured with digital color imaging (SHIL). In addition, we determined P -wave velocity values (PWC) at discrete points on the working halves for all cores from Site U1538 and measured discrete samples for MAD of wet bulk density, dry bulk density, and grain density for Hole U1538A. The sensors worked correctly, and the data are of good quality except for those from the PWL below 50 mbsf.

Figure F33. SHMSL color reflectance L*, a*, and b* and color component R, Hole U1538A.



Diatom ooze and silty clay dominate the lithology for the upper 300 m, whereas silty clay and diatomite dominate from 310 mbsf downhole. Some sections in the lower part of Hole U1538A are characterized by intervals of gravel and gravel-rich rocks such as breccia and conglomerate. Sediment physical properties vary most strongly at depths where the transition between interglacial oozes and glacial clays are observed, as in Cores 382-U1538D-3H through

4H. Diatom-dominated lithologies have lower NGR, density, and MS than silty clay-dominated lithologies. Accordingly, the physical property data obtained for Holes U1538A-U1538D provide valid and reproducible information on sediment composition and variability for all cores. The physical property records show characteristic 1-10 m scale variations that likely reflect characteristic orbital-scale cyclicity in sedimentation during the Pliocene and Pleistocene.

Figure F34. SHMSL color reflectance L*, a*, and b* and color component R, Hole U1538C.

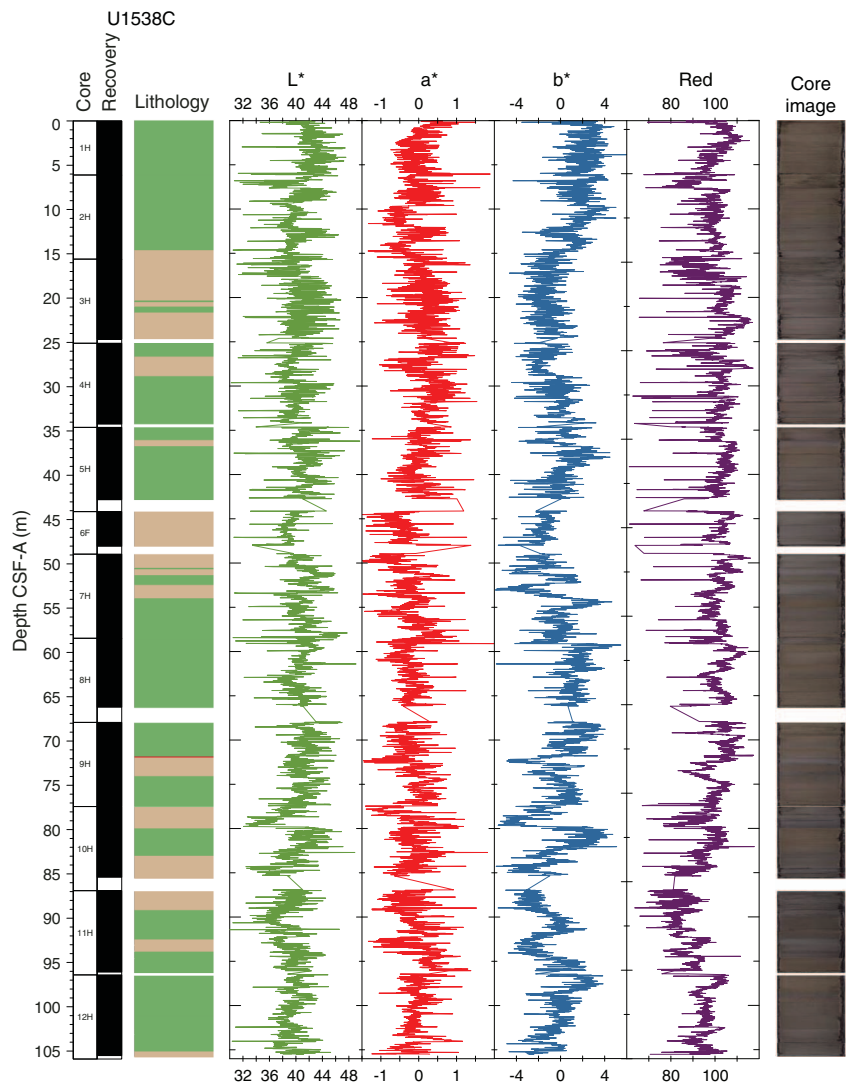
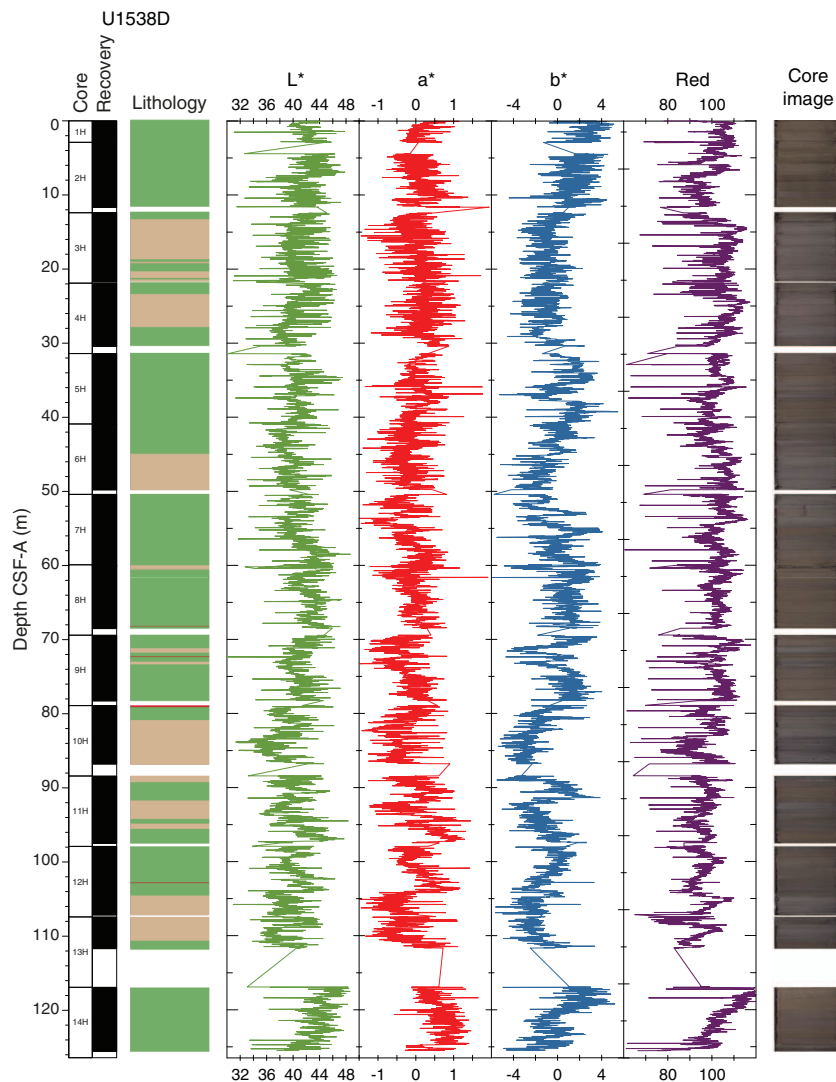


Figure F35. SHMSL color reflectance L*, a*, and b* and color component R, Hole U1538D.



Stratigraphic correlation

Physical property data from Holes U1538A–U1538D were stratigraphically correlated to construct as continuous a record as possible for the site. We used mainly GRA density, MS, and NGR intensity (see **Physical properties**; also see **Physical properties** in the Expedition 382 methods chapter [Weber et al., 2021a] for details). All core physical properties were determined after the cores had warmed up to room temperature. However, to minimize coring gap alignment during coring, the MS of some of the cores was determined at a 2 or 2.5 cm resolution on the WRMSL in near-real time as a first pass in advance of their reaching room temperature because tests showed minimal difference between MS measured at the initial temperature versus room temperature.

Correlation between holes

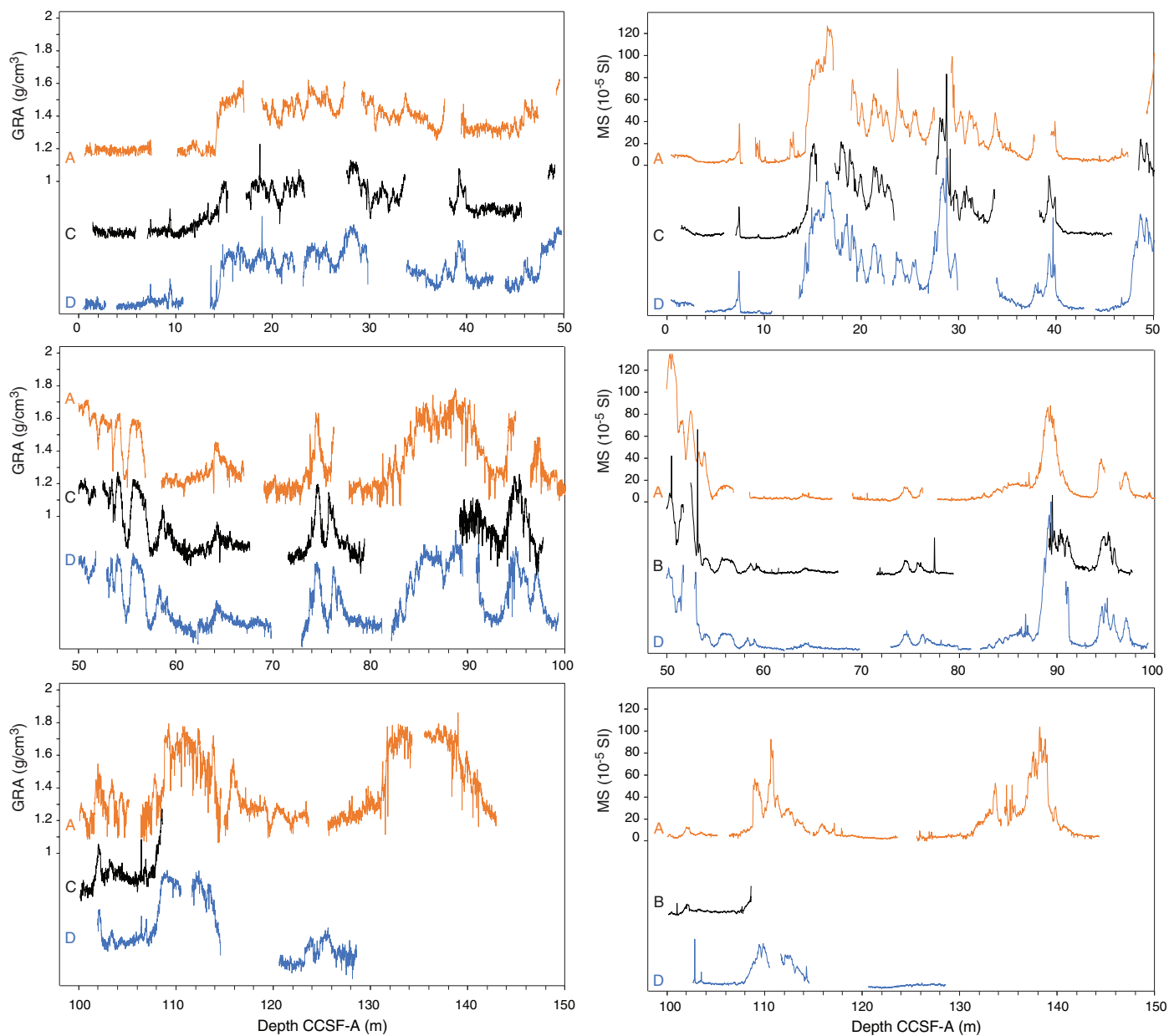
The top of Hole U1538A preserved the best mudline and was the longest first core in all four holes, so it served as the anchor (zero depth point) for generating the core composite depth below seafloor, Method A (CCSF-A), depth scale at this site (see **Stratigraphic correlation** in the Expedition 382 methods chapter [Weber et al., 2021a]). We attempted to document the relative depth offset

Table T23. Splice offsets, Site U1538. [Download table in CSV format.](#)

of each APC core from this reference by establishing affine ties between cores from Holes U1538A–U1538D to ~130 mbsf, based on the optimized correlation of predominantly WRMSL-derived MS and GRA density data. These depth offsets (or affine ties) are reported in Table T23, and the resulting correlations of GRA and MS are shown in Figure F36. We were able to establish two affine ties for most of the APC cores on the CCSF-A depth scale above ~130 mbsf. Core 382-U1538A-6H was significantly distorted during the coring process. Although we were able to link this core with Cores 382-U1538C-6F, 7H, 382-U1538D-6H, and 7H using its MS, its distortion led us not to include it in the splice. Instead, Core 382-U1538D-7H is appended to Core 6H, and the gap between these two cores is determined by the affine tie of Core 382-U1538D-7H to Core 382-U1538A-6H (Figure F37).

Poor recovery of Core 382-U1538D-13H (45%) meant that the coring gap between Cores 382-U1538A-12H and 13H was not bridged. This gap was covered in the splice by an append of Core 382-U1538A-13H onto Core 12H using the average affine growth of the splice above this depth (~1.08, or 8%). Several tenuous ties also occur in our affine table (see quality comments in Table T23) that

Figure F36. GRA density and MS data, Site U1538.



are attributed to the fact that overlaps between cores were sometimes small (making it necessary to connect a core to Section 1 or to the bottom section of a core) because a good offset was not always maintained for APC coring depths between holes above ~130 mbsf because of high heave conditions. Additionally, the high heave meant that some cores were stretched and often all of Section 1 and sometimes also the top halves of Section 2 in a number of cores were soupy (e.g., Cores 382-U1538A-6H, 10H, 12H, 382-U1538C-2H through 4H, 9H, 11H, 382-U1538D-2H through 4H, and 13H), so they could not be used for correlation.

Affine ties that require confirmation and/or refinement with postcruise X-ray fluorescence (XRF) core scanning are listed in Table T24. It is also worth stating that coring artifacts (such as post-coring expansion and/or stretching and compression, in particular, of Sections 1 and 7), as well as small differences in sedimentation rates between cores, mean that single depth offsets derived from af-

fine ties will result in inevitable misalignment of features in CCSF-A depths that can otherwise confidently be correlated visually between holes. This misalignment is an essential consideration for sampling out of the splice and for the use of age data based on shipboard micropaleontology (nearly all of which were derived from Hole U1538A core catchers, which are never in the splice).

Construction of the splice

Once the composite depth scale was created, selected sequences from Holes U1538A, U1538C, and U1538D were spliced together to create the most complete and representative section possible (Figure F37). Detailed sedimentological logs and archive-half X-ray images were consulted in the process of splice construction to avoid the inclusion of any significantly disturbed intervals and/or sections with unique features (relative to the other holes). The end product is reported in Table T25.

Figure F37. Spliced record of GRA density, NGR intensity, and MS, Site U1538. Sections used to construct spliced records are shown at base of figure (see Table T24).

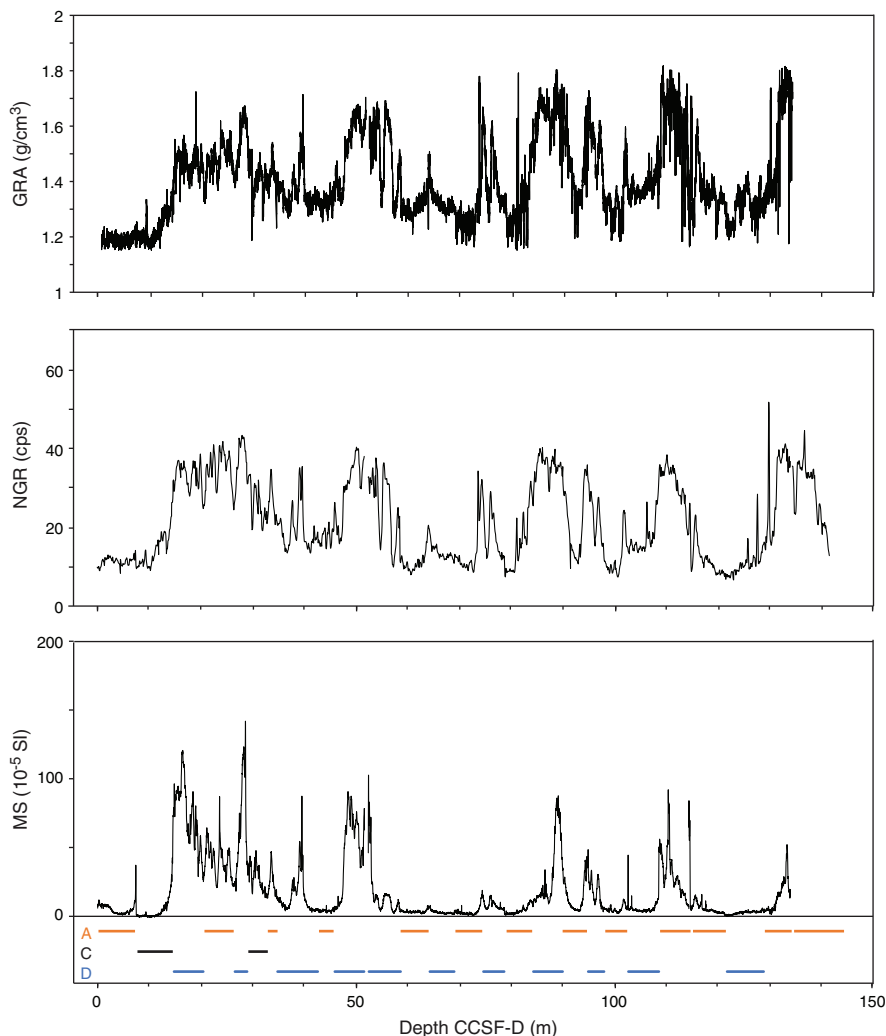


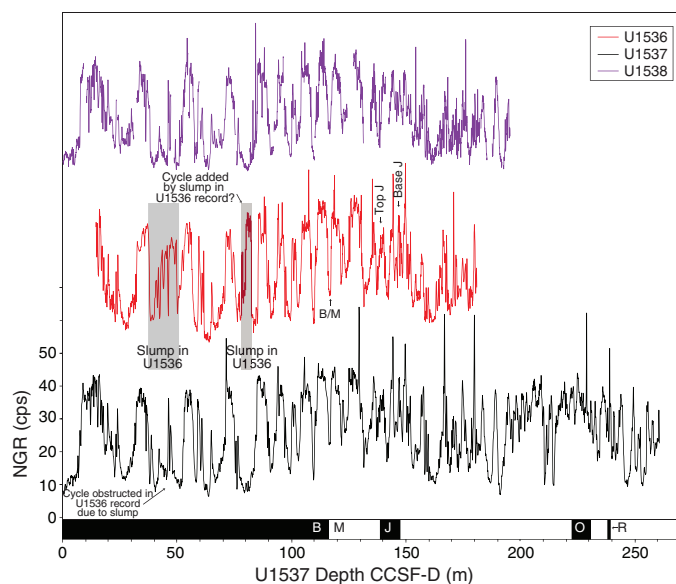
Table T24. Cores that need postcruise X-ray fluorescence (XRF) scanning to verify affine ties, Site U1538. MS = magnetic susceptibility. Sed = sedimentology, pmag = paleomagnetism. [Download table in CSV format.](#)

Hole, core	Hole, core	Reason
382-	382-	
U1538C-2H	U1538A-2H	MS tie not strong
U1538A-4H	U1538D-5H	MS looks like this is slightly wrong
U1538C-5H	U1538A-5H	Correlated with intervals of low variability in all parameters
U1538C-6H	U1538A-6H	Core 382-U1538A-6H is the core that the sed and pmag team call flow-in; I don't think it is flow-in but is a very stretched core of very low quality, but it can't be avoided if we want to splice; it needs running on XRF
U1538A-6H	U1538C-7H	Core 382-U1538A-6H is the core that the sed and pmag team call flow-in; I don't think it is flow-in, but is a very stretched core of very low quality, but it can't be avoided if we want to splice; it needs running on XRF
U1538D-7H	U1538A-7H	Correlated with intervals of low variability in all parameters
U1538A-7H	U1538C-8H	Correlated with intervals of low variability in all parameters
U1538A-7H	U1538D-8H	Correlated with intervals of low variability in all parameters
U1538D-8H	U1538A-8H	Correlated with intervals of low variability in all parameters, near end of Core 382-U1538D-8H
U1538C-9H	U1538A-9H	Correlated with intervals of low variability in all parameters, into top of Section 382-U1538A-9H-1
U1538C-10H	U1538D-10H	Not clear based on MS
U1538D-12H	U1538A-12H	Not clear based on MS
U1538D-13H	U1538A-13H	Does not correlate in our affine but we need to check in case it does
U1538A-13H	U1538D-14H	Not clear on any parameter apart from perhaps b*
U1538D-14H	U1538A-14H	Not clear on any parameter apart from perhaps b*

Table T25. Splice ties, Site U1538. [Download table in CSV format.](#)

Table T26. Depth tie points between Hole U1538A and the Site U1537 splice. [Download table in CSV format](#)

Figure F38. Comparison of Pleistocene stratigraphies, Sites U1536–U1538. NGR intensity data shown on Site U1537 CCSF-D scale after independent manual graphic correlation of Site U1536 record (on splice depths; see Stratigraphic correlation in the Site U1536 chapter [Weber et al., 2021b]) and Site U1538 record (on Hole U1538A mbsf depths; gaps in data series indicate core breaks; Table T26) with Site U1537 NGR splice. Site U1538 and U1536 data are offset vertically from y-axis values. Black and white horizontal bars at base of figure denote GPTS2012 interpretation of Site U1537 magnetostratigraphy (see Paleomagnetism) B/M = Brunhes/Matuyama boundary (0.781 Ma), J = Jaramillo (0.99–10.7 Ma), O = Olduvai (1.78–1.95 Ma), R = Reunion (2.13–2.15 Ma). Annotated arrows along top of figure = depth relationships of corresponding magnetochron reversals in Site U1536 stratigraphy to Site U1538 NGR record confirming that ties established between Site U1536 and U1537 stratigraphies are plausible. Diagenesis below ~60 m CCSF-D complicates generation of magnetostratigraphy for Site U1538 (see Paleomagnetism). Strong correlation presented here therefore also highlights how polarity chron interpretation for Site U1537 (for example) can be exported for use at Site U1538 via NGR correlation.



The primary splice for Site U1538 spans 0–124 m core composite depth below seafloor, Method D (CCSF-D). It is based predominantly on the correlation of sediment MS and GRA density data. Overall, Hole U1538A makes up ~49% of the splice, Hole U1538C makes up ~5% of the splice, and Hole U1538D makes up ~46% of the splice (Figure F37). Below 124 m CCSF-D (Core 382-U1538A-12H), we appended a chain (or floating splice) involving Cores 382-

U1538A-13H, 14H, and 382-U1538D-14H to ~135 m CCSF-D (base of Core 382-U1538A-14H). Below ~135 m CCSF-D, core recovery was good through Core 382-U1538A-22H, but no companion hole is available with which to splice.

Comparison of stratigraphy between Sites U1536, U1537, and U1538

Because the Site U1538 splice only extends to 124 m CCSF-D, to compare fully the Pleistocene stratigraphy from this site to those recovered from Sites U1537 and U1536, we tied the Hole U1538A NGR record on its meters below seafloor coring depths to the spliced NGR record from Site U1537 (Table T26; Figure F38). This exercise highlights four important observations:

- Remarkable similarities exist between all three records.
- Strong correlations can be made between Hole U1538A NGR data and the Site U1537 splice to ~377 mbsf in Hole U1538A.
- Unlike at Site U1536, the Site U1538 late Pleistocene stratigraphy is not affected by slumping.
- Sedimentation rates are substantially higher at Site U1538 than Site U1537 and relative to Site U1536 prior to the last glacial cycle (>70 m CCSF-D; Table T26; Figure F38). For reference, the bottom core from Site U1538 in this figure has a coring depth of 371.8 mbsf (bottom of Core 382-U1538A-42X) compared to ~195 m on the Site U1537 CCSF-D depth scale shown.

Downhole measurements

Downhole temperature and heat flow

Advanced piston corer temperature tool (APCT-3) downhole temperature measurements were made in Holes U1538A (Cores 382-U1538A-6H, 9H, 12H, 15H, and 18H) and U1538D (Core 382-U1538D-12H). The seafloor temperature was determined to be 0.2°C based on APCT-3 data taken while the tool was held at the mudline for 5 min during each run (Figure F39). The measurement on Core 382-U1538A-12H did not yield reliable results because of high heave conditions. The obtained temperatures range from 4.8°C at 55.3 mbsf to 13.8°C at 178.8 mbsf (Table T27; Figures F39, F40), giving an approximately linear temperature increase with depth and a geothermal gradient of 74°C/km.

Thermal conductivity under in situ conditions was estimated from laboratory-determined thermal conductivity for Hole U1538A using the method of Hyndman et al. (1974) (see [Physical properties](#) in the Expedition 382 methods chapter [Weber et al., 2021a]). The calculated in situ values are within 2% of the measured laboratory values. Thermal resistance was calculated by integrating the inverse of the in situ thermal conductivity over depth. Considering all thermal conductivity measurements down the hole, a heat flow of 75 mW/m² was estimated from the linear fit between temperature and thermal resistance following the method of Pribnow et al. (2000).

Figure F39. APCT-3 temperature-time series, Site U1538.

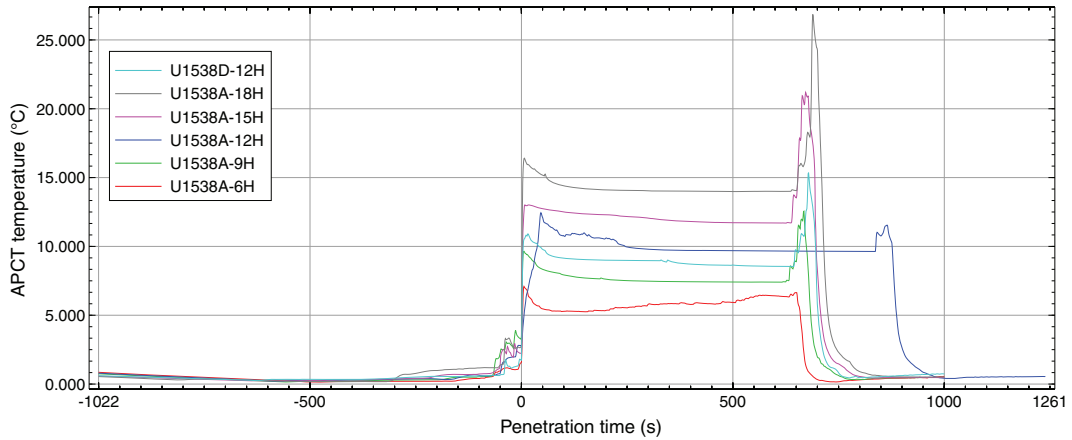
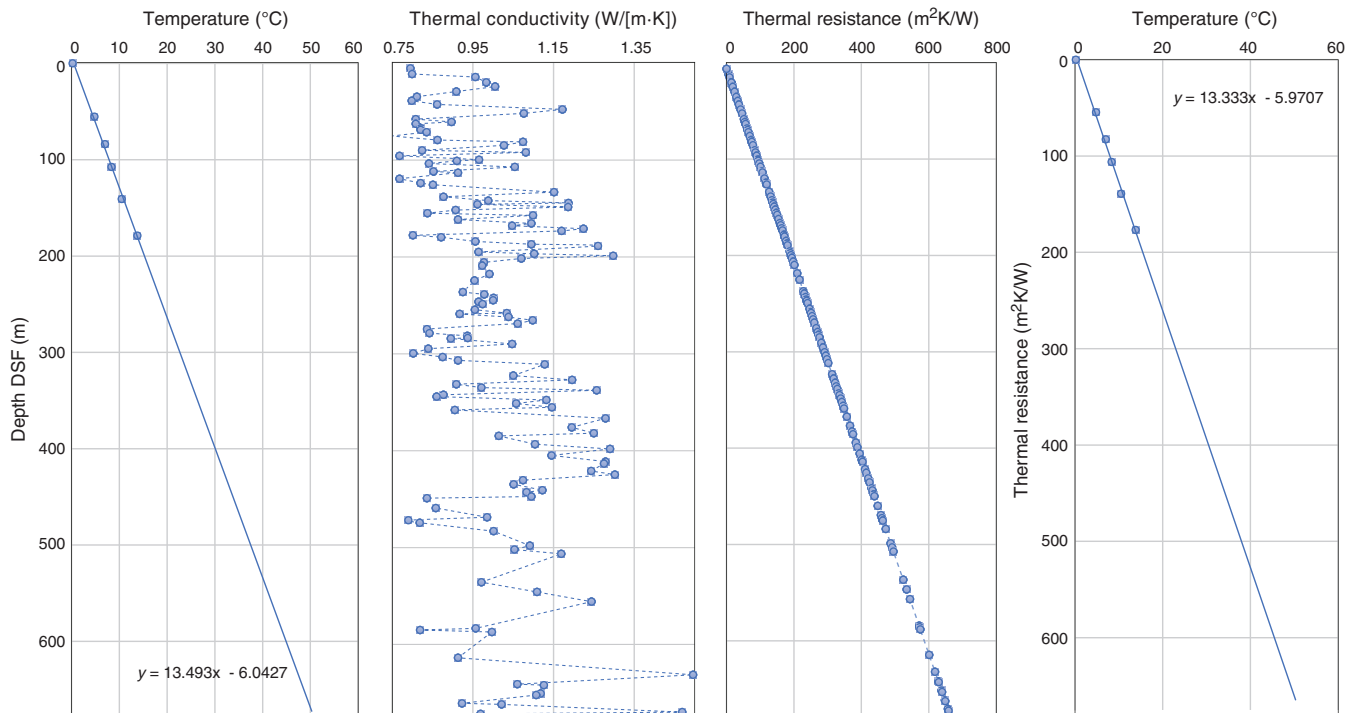


Table T27. Formation temperatures derived from APCT-3 measurements, Site U1538. APCT-3 = advanced piston corer temperature tool. [Download table in CSV format.](#)

Hole, core	APCT-3 depth DSF (m)	Temperature (°C)	Quality
382-			
Seafloor	0.0	0.2	Tentative value
U1538A-6H	55.3	4.8	Not good
U1538A-9H	83.8	7	Good
U1538A-12H	112.3	9.5	Really bad
U1538B-12H	107.4	8.35	Good
U1538A-15H	140.8	10.5	Fair
U1538A-18H	178.8	13.8	Good

Figure F40. Heat flow calculation, Site U1538. Thermal conductivity data are from Hole U1538A. Right panel shows Bullard plot of heat flow calculated from linear fit of temperature data. DSF = drilling depth below seafloor.



Core-log-seismic integration

The regional sedimentary record of the Scotia Sea is composed of five distinguishable seismic units (V–I in upward stratigraphic order). The seismic units are bounded by four stratigraphic discontinuities that form strong reflectors (d–a from bottom to top) (e.g., Maldonado et al., 2006; Martos et al., 2013; Pérez et al., 2014). In some of the local basins of the Scotia Sea, an additional stratigraphic discontinuity has been identified in Unit I and is named Reflector a' (Pérez et al., 2017). Reflector a' divides Unit I into Subunits Ib and Ia from bottom to top. In the *Scientific Prospectus* for this expedition (Weber et al., 2018), stratigraphic discontinuities were identified in the Pirie Basin MCS Line SCAN2013-SCS13 as Reflectors c, b, a, and a'. However, because this seismic line is noisy and because the Pirie Basin is geographically isolated from the basins to the south, the discontinuities and reflectors identified in the Pirie Basin (Site U1538) may not necessarily be contemporaneous with those previously identified in the Dove Basin (Sites U1536 and U1537) (e.g., Pérez et al., 2017). The relationship between the reflectors in the two basins will be refined in postcruise work.

At Site U1538, we recovered the sedimentary record from the seafloor to about 100 m below Reflector c. The physical properties measured on the cores recovered from Site U1538, Seismic Line SCAN2013-SCS13 (Figures F41, F42), and echo sounder topographic parametric sonar (TOPAS) Profile SCAN2013-L13 (Figures F43, F44) are integrated in this section. Correlation of the seismic signal with depth uses a velocity model based on the discrete PWC velocity measurements. Velocity measurements on cores are often underestimates of in situ velocity values, as was observed during logging operations in Hole U1536E, and the time-depth relationship and the correlation of physical properties with the seismic reflector need to be refined in postcruise work.

The physical properties and age models obtained during Expedition 382 allow us to constrain the age ranges of previously identified seismic units and develop an age model for the stratigraphic discontinuities (Table T28).

Physical properties and relationship with multichannel seismic interpretation

MCS Line SCAN2013-SCS13 allows the identification of the main seismic units at Site U1538. APC, HLAPC, and XCB coring recovered the sedimentary record to ~676 mbsf in Hole U1538A, reaching the upper part of Unit IV and a complete section of the three uppermost seismic units of the regional sedimentary record of the Scotia Sea (Units III–I) (e.g., Maldonado et al., 2006; Martos et al., 2013; Pérez et al., 2014). All identified stratigraphic discontinuities represent changes in the seismic record and in physical properties measured on the cores in the laboratory (Figures F41, F42). Details of core-log physical property variability at Site U1538 are described in detail in **Physical properties**. Here, we focus on the comparison to seismic data and show overview figures only.

Reflector c is located at ~575 mbsf, or ~4964 ms two-way travel-time (TWT), in Core 382-U1538A-64X. The seismic unit below Reflector c (upper portion of Unit IV) is characterized by relatively high and constant values of wet bulk density (MAD), which decline uphole from ~620 mbsf, and highly variable GRA density values. Loop magnetic susceptibility (MSL) values are high in Unit IV. In the seismic profile, this part of Unit IV matches a zone of high-amplitude, laterally continuous reflections.

Above Reflector c, Unit III is characterized by constant and slightly lower GRA density and MAD, both of which show a slight uphole increase throughout this unit. MSL and NGR values are similar to those in Unit IV. The general character of the physical property values correlates with an area of poorly defined reflections in the seismic profile that includes Unit III and the lower part of Unit II uphole to ~459 mbsf. Reflector b (top of Unit III) is located in this low-reflectivity area of the seismic profile and displayed as a slightly higher amplitude reflection at ~513 mbsf, or ~4893 ms TWT, in Core 382-U1538A-57X.

Unit II is above Reflector b and is observed from ~513 to ~370 mbsf. Following the poorly defined reflections continuing from Unit III, the seismic profile shows low-amplitude and discontinuous reflections from ~459 to ~371 mbsf. At ~459 mbsf, a laterally continuous reflection of intermediate amplitude coincides with a local minimum in PWC, MAD, and GRA values. This reflection marks the transition to an uphole increasing trend in all physical property values to ~405 mbsf. All physical properties values decrease from this depth to ~370 mbsf, or ~4711 ms TWT, in Core 43X, where Reflector a was identified in the seismic record as a laterally continuous and high-amplitude reflection marking the top of Unit II.

Unit I is above Reflector a from ~370 mbsf to the seafloor. Unit I is divided into Subunits Ib (lower) and Ia (upper) by Reflector a' at ~90 mbsf. Above Reflector a (in Subunit Ib), an uphole decreasing trend in all physical properties is identified to ~297 mbsf. This area coincides with high-amplitude and laterally continuous reflections in the seismic profile. Above ~297 mbsf, an area of low-amplitude, chaotic reflections correlates with a high variability and uphole increase in NGR, GRA density, and MAD values to ~228 mbsf. From ~228 mbsf to the top of the site (seafloor), MAD, GRA density, and PWC vary with high amplitude, probably reflecting glacial–interglacial variability. Reflector a' marks a change at ~90 mbsf, or ~4348 ms TWT, from higher (below) to lower (above) variability and is located in Core 382-U1538A-10H. In addition, Reflector a' represents a change in the seismic facies from high-amplitude and laterally continuous reflections in Subunit Ib to low-amplitude but still laterally continuous reflections in overlying Subunit Ia.

Physical properties and relationship with parametric echo sounder interpretation

Physical properties obtained from laboratory measurements on cores from Site U1538 are correlated with TOPAS Profile SCAN2013-L13 (Figure F44). The TOPAS profile allows the identification of acoustic reflections to a maximum depth of around 134 mbsf, or 4410 ms TWT. This depth includes the upper part of Subunit Ib and Subunit Ia.

In Subunit Ib, which is between Reflector a below and Reflector a' above, PWC, MAD, and GRA density show very slight uphole decreasing trends with low-amplitude oscillations that correlate with a package of very low amplitude reflections in the TOPAS profile. The few reflections identified in this area are interpreted to be related to minimum values in PWC, GRA density, MAD, and NGR. In the uppermost part of Subunit Ib in a 10 m section from 90 to 80 mbsf, all physical properties show maximum values in an area of transparent facies in the TOPAS profile. At the top, Reflector a is observed as a high-amplitude, irregular reflection in the TOPAS profile.

Above Reflector a', three major intervals are defined in Subunit Ia, which extends uphole to the seafloor. The lower part uphole to ~45 mbsf presents oscillations in NGR. MSL in this section shows

Figure F41. Physical property measurements and comparison with Seismic Profile SCAN2013-SCS13, Hole U1538A. MD = measured depth.

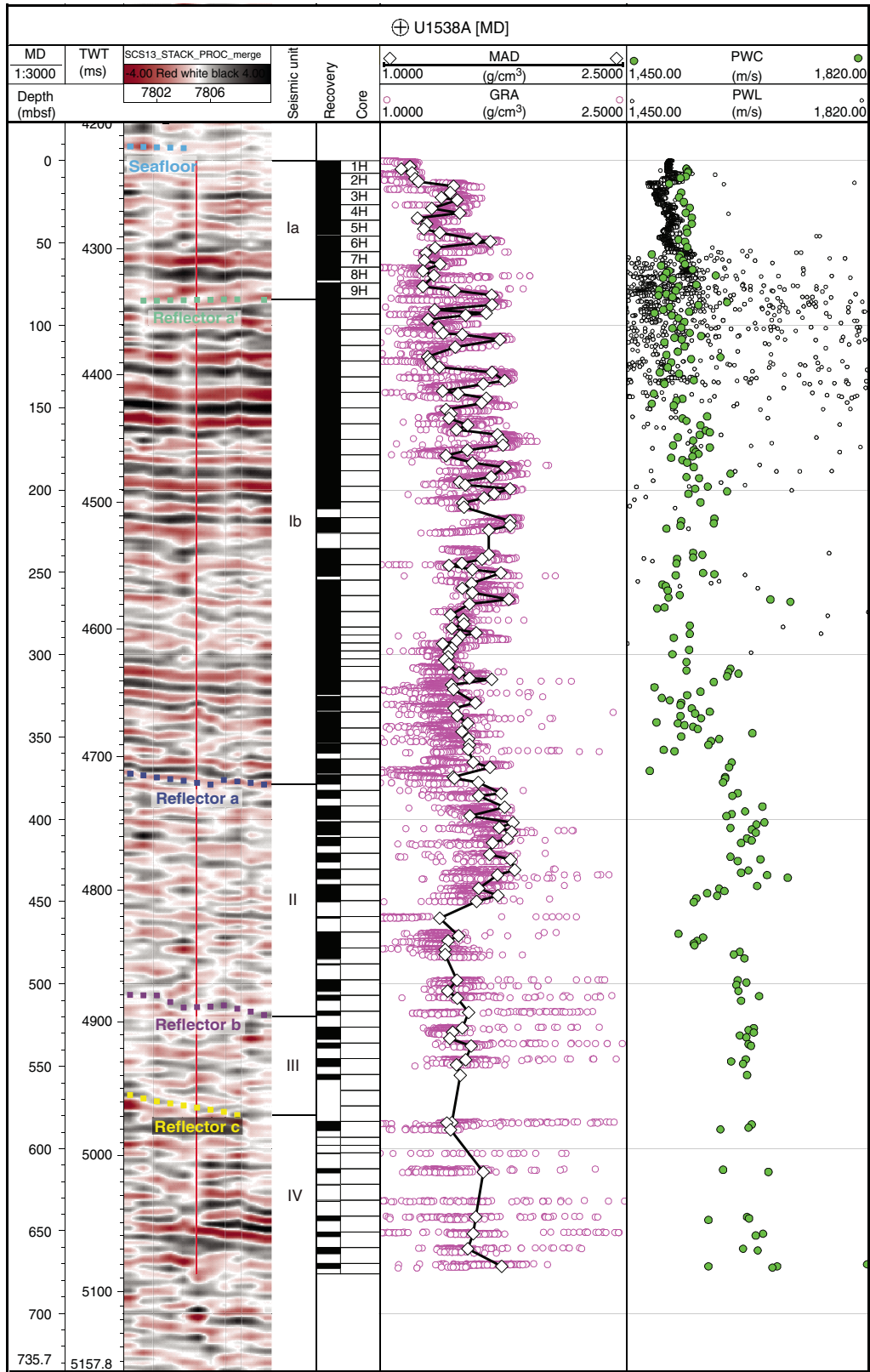
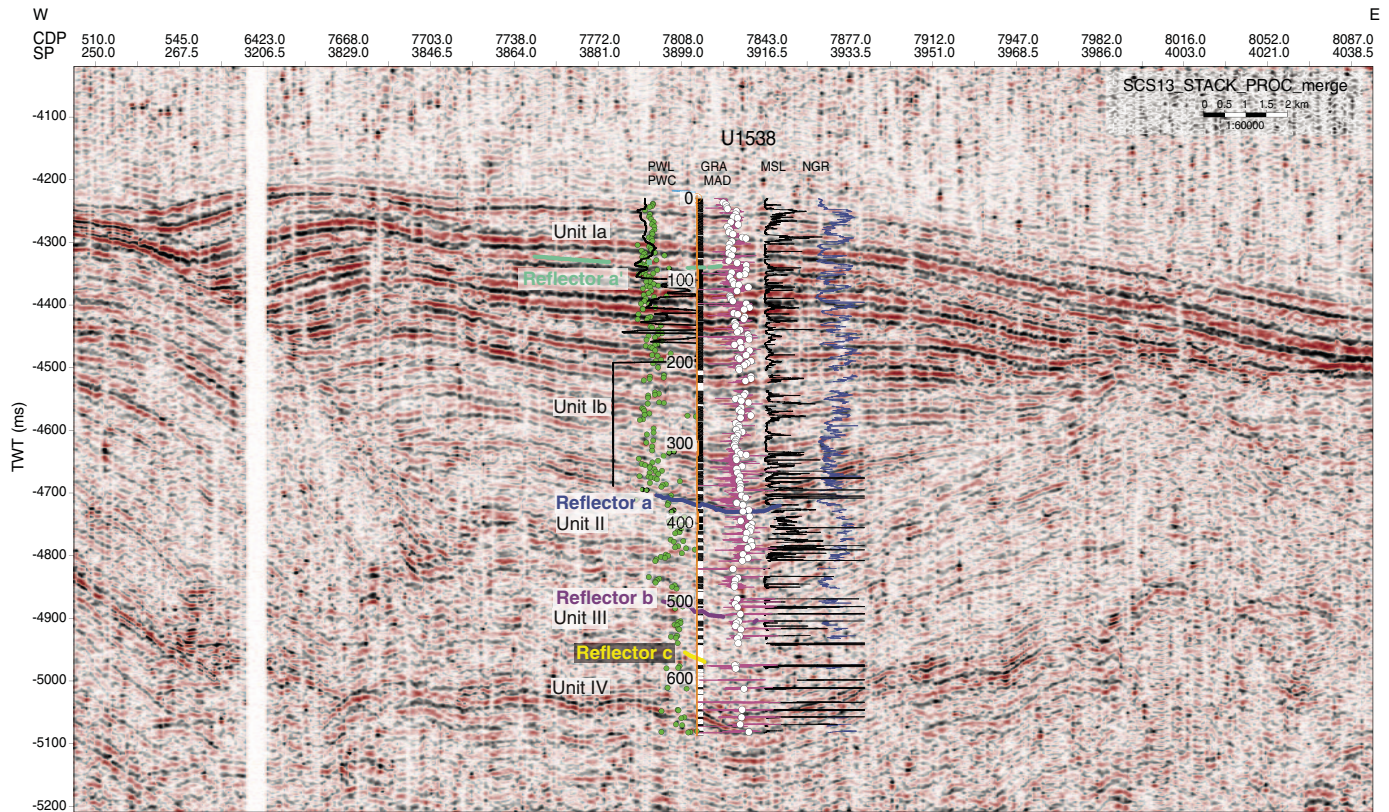


Figure F42. MCS Profile SCAN2013-SCS13 and physical properties, Hole U1538A. Green dots = PWC, black line = PWL, magenta line = GRA, open dots = discrete wet bulk density (MAD), black line = MSL, blue line = NGR. CDP = common depth point, SP = shotpoint.



little variability with the exception of a couple of transitory peaks, and GRA shows very little variability. A peak in all three values is noted near ~50 mbsf. These properties correspond to transparent facies in the TOPAS profile. A high-amplitude reflection of high lateral continuity is identified in this area at ~72 mbsf, corresponding to an interval that was not recovered between Cores 382-U1538A-8H and 9H. In the middle part of Subunit Ia (45–13.5 mbsf), GRA density and MAD present less variability than was observed in the interval below. *P*-wave velocity, MSL, and NGR values present an uphole increasing trend in this interval (Figure F44). In the TOPAS

profile, medium-amplitude reflections that are laterally continuous correlate with this interval. The uppermost part of Subunit Ia (~13.5 mbsf to the seafloor) presents relatively constant values in all the physical properties. GRA density, MAD, MSL, and NGR values are lower and *P*-wave velocity values are higher relative to the lower part of Subunit Ia. The acoustic signal observed in the TOPAS profile changes from high-amplitude to low-amplitude reflections at ~8 mbsf, in agreement with an observed minimum GRA density value and maximum MSL value.

Figure F43. Physical property measurements and comparison with TOPAS Line SCAN2013-L13, Hole U1538A.

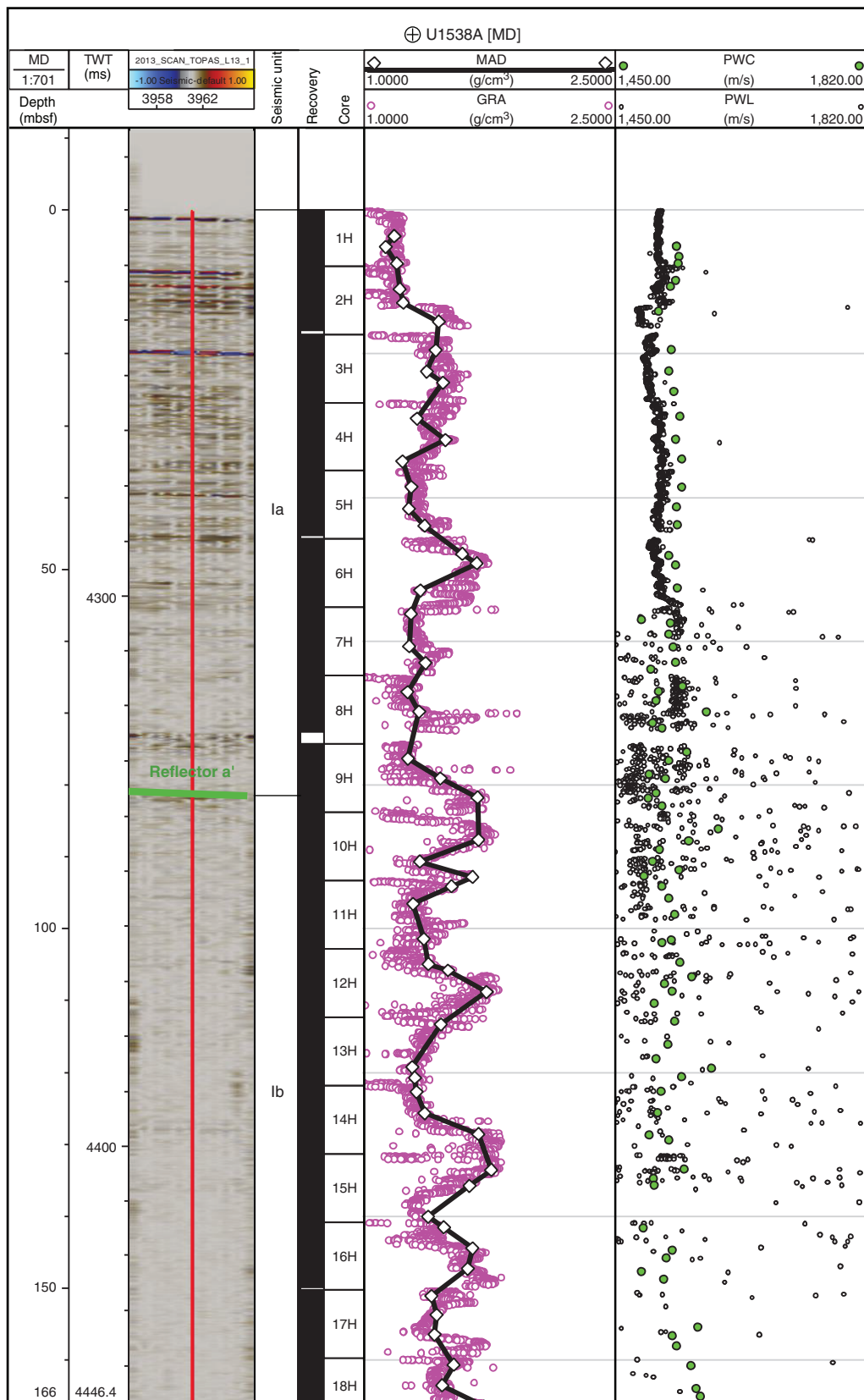


Figure F44. TOPAS Line SCAN2013-L13 and physical properties, Hole U1538A. Green dots = PWL, diamonds linked with black line = PWC, magenta line = GRA, black line = MSL, blue line = NGR.

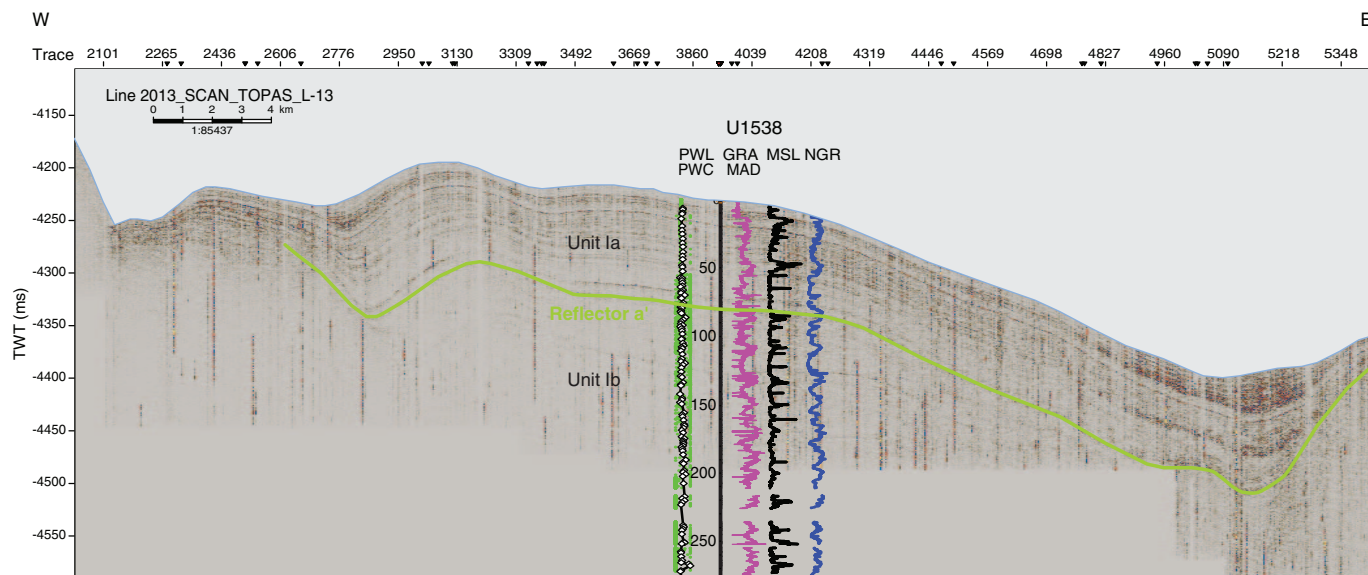


Table T28. Age model of main stratigraphic discontinuities, Site U1538.

* = determined by magnetostratigraphy, † = determined by biostratigraphy.

TWT = two-way traveltime. [Download table in CSV format.](#)

Discontinuity	Depth TWT (ms)	Depth (mbsf)	Core	Age (Ma)*	Age (Ma)†
			382-U1538A-		
Reflector a'	4348	90	10H	0.35	0.14
Reflector a	4711	370	43X	1.6	1.5
Reflector b	4893	513	57X	3.9	3.9
Reflector c	4964	575	64X	4.45	4.45

References

- Berg, R.D., and Solomon, E.A., 2016. Geochemical constraints on the distribution and rates of debromination in the deep seafloor biosphere. *Geochimica et Cosmochimica Acta*, 174:30–41. <https://doi.org/10.1016/j.gca.2015.11.003>
- Blum, P., 1997. *Technical Note 26: Physical Properties Handbook—A Guide to the Shipboard Measurement of Physical Properties of Deep-Sea Cores*. Ocean Drilling Program. <https://doi.org/10.2973/odp.tn.26.1997>
- Esper, O., and Zonneveld, K.A.F., 2007. The potential of organic-walled dinoflagellate cysts for the reconstruction of past sea-surface conditions in the Southern Ocean. *Marine Micropaleontology*, 65(3–4):185–212. <https://doi.org/10.1016/j.marmicro.2007.07.002>
- Hyndman, R.D., Erickson, A.J., and Von Herzen, R.P., 1974. Geothermal measurements on DSDP Leg 26. In Davies, T.A., Luyendyk, B.P., et al., *Initial Reports of the Deep Sea Drilling Project*, 26: Washington, DC (U.S. Govt. Printing Office), 451–463. <https://doi.org/10.2973/dsdp.proc.26.113.1974>
- Key, R.M., Olsen, A., van Heuven, S., Lauvset, S.K., Velo, A., Lin, X., Schirnick, C., et al., 2015. Global Ocean Data Analysis Project, Version 2 (GLODAPv2), ORNL/CDIAC-162, ND-P093. Oak Ridge, Tennessee (US Department of Energy). https://doi.org/10.3334/CDIAC/OTG.NDP093_GLODAPv2
- Maldonado, A., Bohoyo, F., Galindo-Zaldívar, J., Hernández-Molina, J., Jabloay, A., Lobo, F.J., Rodríguez-Fernández, J., Suriñach, E., and Vázquez, J.T., 2006. Ocean basins near the Scotia–Antarctic plate boundary: influence of tectonics and paleoceanography on the Cenozoic deposits. *Marine Geophysical Researches*, 27(2):83–107. <https://doi.org/10.1007/s11001-006-9003-4>
- Martos, Y.M., Maldonado, A., Lobo, F.J., Hernández-Molina, F.J., and Pérez, L.F., 2013. Tectonics and palaeoceanographic evolution recorded by contourite features in southern Drake Passage (Antarctica). *Marine Geology*, 343:76–91. <https://doi.org/10.1016/j.margeo.2013.06.015>
- Olsen, A., Key, R.M., van Heuven, S., Lauvset, S.K., Velo, A., Lin, X., Schirnick, C., et al., 2016. The Global Ocean Data Analysis Project version 2 (GLODAPv2) – an internally consistent data product for the world ocean. *Earth System Science Data*, 8:2907–323. <https://doi.org/10.5194/essd-8-297-2016>
- Pérez, L.F., Maldonado, A., Bohoyo, F., Hernández-Molina, F.J., Vázquez, J.T., Lobo, F.J., and Martos, Y.M., 2014. Depositional processes and growth patterns of isolated oceanic basins: the Protector and Pirie basins of the Southern Scotia Sea (Antarctica). *Marine Geology*, 357:163–181. <https://doi.org/10.1016/j.margeo.2014.08.001>
- Pérez, L.F., Maldonado, A., Hernández-Molina, F.J., Lodolo, E., Bohoyo, F., and Galindo-Zaldívar, J., 2017. Tectonic and oceanographic control of sedimentary patterns in a small oceanic basin: Dove Basin (Scotia Sea, Antarctica). *Basin Research*, 29(S1):255–276. <https://doi.org/10.1111/bre.12148>
- Pribnow, D., Kinoshita, M., and Stein, C., 2000. *Thermal Data Collection and Heat Flow Recalculations for Ocean Drilling Program Legs 101–180*: Hanover, Germany (Institute for Joint Geoscientific Research, Institut für Geowissenschaftliche Gemeinschaftsaufgaben [GGA]). <http://www-odp.tamu.edu/publications/heatflow/ODPReprt.pdf>
- Roberts, A.P., Chang, L., Rowan, C.J., Horng, C.-S., and Florindo, F., 2011. Magnetic properties of sedimentary greigite (Fe₃S₄): an update. *Reviews of Geophysics*, 49(1):RG1002. <https://doi.org/10.1029/2010RG000336>
- Sprenk, D., Weber, M.E., Kuhn, G., Rosén, P., Frank, M., Molina-Kescher, M., Liebetrau, V., and Röhlhng, H.-G., 2013. Southern Ocean bioproductivity during the last glacial cycle—new decadal-scale insight from the Scotia Sea. *Geological Society Special Publication*, 381(1):245–261. <https://doi.org/10.1144/SP381.17>
- Weaver, F.M., 1983. Cenozoic radiolarians from the southwest Atlantic, Falkland Plateau region, Deep Sea Drilling Project Leg 71. In Ludwig, W.J., Krashennnikov, V.A., et al., *Initial Reports of the Deep Sea Drilling Project*, 71 (Part 2): Washington (U.S. Govt. Printing Office), 667–686. <https://doi.org/10.2973/dsdp.proc.71.126.1983>
- Weber, M.E., 1998. Estimation of biogenic carbonate and opal by continuous non-destructive measurements in deep-sea sediments: application to the

- eastern equatorial Pacific. *Deep-Sea Research, Part I: Oceanographic Research Papers*, 45(11):1955–1975.
[https://doi.org/10.1016/S0967-0637\(98\)00028-4](https://doi.org/10.1016/S0967-0637(98)00028-4)
- Weber, M.E., Niessen, F., Kuhn, G., and Wiedicke, M., 1997. Calibration and application of marine sedimentary physical properties using a multi-sensor core logger. *Marine Geology*, 136(3–4):151–172.
[https://doi.org/10.1016/S0025-3227\(96\)00071-0](https://doi.org/10.1016/S0025-3227(96)00071-0)
- Weber, M.E., Raymo, M.E., Peck, V.L., and Williams, T., 2018. *Expedition 382 Scientific Prospectus: Iceberg Alley and South Falkland Slope Ice and Ocean Dynamics*. International Ocean Discovery Program.
<https://doi.org/10.14379/iodp.sp.382.2018>
- Weber, M.E., Raymo, M.E., Peck, V.L., Williams, T., Armbrrecht, L.H., Bailey, I., Brachfeld, S.A., Cardillo, F.G., Du, Z., Fauth, G., García, M., Glüder, A., Guitard, M.E., Gutjahr, M., Hemming, S.R., Hernández-Almeida, I., Hoem, F.S., Hwang, J.-H., Iizuka, M., Kato, Y., Kenlee, B., Martos, Y.M., O’Connell, S., Pérez, L.F., Reilly, B.T., Ronge, T.A., Seki, O., Tauxe, L., Tripathi, S., Warnock, J.P., and Zheng, X., 2021a. Expedition 382 methods. *In* Weber, M.E., Raymo, M.E., Peck, V.L., Williams, T., and the Expedition 382 Scientists, *Iceberg Alley and Subantarctic Ice and Ocean Dynamics*. Proceedings of the International Ocean Discovery Program, 382: College Station, TX (International Ocean Discovery Program).
<https://doi.org/10.14379/iodp.proc.382.102.2021>
- Weber, M.E., Raymo, M.E., Peck, V.L., Williams, T., Armbrrecht, L.H., Bailey, I., Brachfeld, S.A., Cardillo, F.G., Du, Z., Fauth, G., García, M., Glüder, A., Guitard, M.E., Gutjahr, M., Hemming, S.R., Hernández-Almeida, I., Hoem, F.S., Hwang, J.-H., Iizuka, M., Kato, Y., Kenlee, B., Martos, Y.M., O’Connell, S., Pérez, L.F., Reilly, B.T., Ronge, T.A., Seki, O., Tauxe, L., Tripathi, S., Warnock, J.P., and Zheng, X., 2021b. Site U1536. *In* Weber, M.E., Raymo, M.E., Peck, V.L., Williams, T., and the Expedition 382 Scientists, *Iceberg Alley and Subantarctic Ice and Ocean Dynamics*. Proceedings of the International Ocean Discovery Program, 382: College Station, TX (International Ocean Discovery Program).
<https://doi.org/10.14379/iodp.proc.382.105.2021>
- Weber, M.E., Raymo, M.E., Peck, V.L., Williams, T., Armbrrecht, L.H., Bailey, I., Brachfeld, S.A., Cardillo, F.G., Du, Z., Fauth, G., García, M., Glüder, A., Guitard, M.E., Gutjahr, M., Hemming, S.R., Hernández-Almeida, I., Hoem, F.S., Hwang, J.-H., Iizuka, M., Kato, Y., Kenlee, B., Martos, Y.M., O’Connell, S., Pérez, L.F., Reilly, B.T., Ronge, T.A., Seki, O., Tauxe, L., Tripathi, S., Warnock, J.P., and Zheng, X., 2021c. Site U1537. *In* Weber, M.E., Raymo, M.E., Peck, V.L., Williams, T., and the Expedition 382 Scientists, *Iceberg Alley and Subantarctic Ice and Ocean Dynamics*. Proceedings of the International Ocean Discovery Program, 382: College Station, TX (International Ocean Discovery Program).
<https://doi.org/10.14379/iodp.proc.382.106.2021>
- Weber, M.E., Raymo, M.E., Peck, V.L., Williams, T., and the Expedition 382 Scientists, 2021d. Supplementary material,
<https://doi.org/10.14379/iodp.proc.382supp.2021>. *Supplement to* Weber, M.E., Raymo, M.E., Peck, V.L., Williams, T., and the Expedition 382 Scientists, *Iceberg Alley and Subantarctic Ice and Ocean Dynamics*. Proceedings of the International Ocean Discovery Program, 382: College Station, TX (International Ocean Discovery Program).
<https://doi.org/10.14379/iodp.proc.382.2021>